OPEN ACCESS
IOP Publishing | International Atomic Energy Agency
Nuclear Fusion
Nucl. Fusion **63** (2023) 112010 (38pp)
https://doi.org/10.1088/1741-4326/acf560

Isotope physics of heat and particle transport with tritium in JET-ILW type-I ELMy H-mode plasmas

P.A. Schneider[1,*], C. Angioni[1], F. Auriemma[2,3], N. Bonanomi[1], T. Görler[1], R. Henriques[4,5], L. Horvath[5,6], D. King[5], R. Lorenzini[2,3], H. Nyström[7], M. Maslov[5], J. Ruiz[8], G. Szepesi[5], C.D. Challis[5], A. Chomiczewska[9], E. Delabie[10], J.M. Fontdecaba[11], L. Frassinetti[7], J. Garcia[12], C. Giroud[5], J. Hillesheim[5], J. Hobirk[1], A. Kappatou[1], D.L. Keeling[5], E. Kowalska-Strzeciwilk[9], M. Lennholm[5], B. Lomanowski[10], T. Luda di Cortemiglia[1], C.F. Maggi[5], S. Menmuir[5], G. Pucella[13], A. Thorman[5] and JET Contributors[a]

[1] Max-Planck-Institut für Plasmaphysik, Boltzmannstr. 2, 85748 Garching, Germany
[2] Consorzio RFX-CNR, ENEA, INFN, Università di Padova, Acciaierie Venete SpA, Padova, Italy
[3] CNR-ISTP, Corso Stati Uniti 4, 35127 Padova, Italy
[4] Instituto de Plasmas e Fusão Nuclear, Instituto Superior Técnico, Universidade de Lisboa, 1049-001 Lisboa, Portugal
[5] United Kingdom Atomic Energy Authority, Culham Science Centre, Abingdon, Oxon OX14 3DB, United Kingdom of Great Britain and Northern Ireland
[6] Princeton Plasma Physics Laboratory, Princeton, NJ 08540, United States of America
[7] KTH Royal Institute of Technology, Teknikringen 31, Stockholm, Sweden
[8] Rudolf Peierls Centre for Theoretical Physics, University of Oxford, Oxford OX1 3PU, United Kingdom of Great Britain and Northern Ireland
[9] Institute of Plasma Physics and Laser Microfusion, Warsaw, Poland
[10] Oak Ridge National Laboratory, Oak Ridge, TN, United States of America
[11] Laboratorio Nacional de Fusión Ciemat, E-28040 Madrid, Spain
[12] CEA, IRFM, F-13108 Saint-Paul-lez-Durance, France
[13] Dip.to Fusione e Tecnologie per la Sicurezza Nucleare, ENEA C. R. Frascati, via E. Fermi 45, 00044 Frascati (Roma), Italy

E-mail: philip.schneider@ipp.mpg.de

Received 28 February 2023, revised 29 August 2023
Accepted for publication 31 August 2023
Published 12 October 2023

Abstract

As part the DTE2 campaign in the JET tokamak, we conducted a parameter scan in T and D-T complementing existing pulses in H and D. For the different main ion masses, type-I ELMy H-modes at fixed plasma current and magnetic field can have the pedestal pressure varying by a factor of 4 and the total pressure changing from $\beta_N = 1.0$ to 3.0. We investigated the pedestal and core isotope mass dependencies using this extensive data set. The pedestal shows a strong

[a] See the author list of "Overview of T and D-T results in JET with ITER-like wall" by C.F. Maggi *et al* to be published in *Nuclear Fusion Special Issue: Overview and Summary Papers from the 29th Fusion Energy Conference (London, UK, 16–21 October 2023)*.
[*] Author to whom any correspondence should be addressed.

mass dependence on the density, which influences the core due to the strong coupling between both plasma regions. To better understand the causes for the observed isotope mass dependence in the pedestal, we analysed the interplay between heat and particle transport and the edge localised mode (ELM) stability. For this purpose, we developed a dynamic ELM cycle model with basic transport assumptions and a realistic neutral penetration. The temporal evolution and resulting ELM frequency introduce an additional experimental constraint that conventional quasi-stationary transport analysis cannot provide. Our model shows that a mass dependence in the ELM stability or in the transport alone cannot explain the observations. One requires a mass dependence in the ELM stability as well as one in the particle sources. The core confinement time increases with pedestal pressure for all isotope masses due to profile stiffness and electromagnetic turbulence stabilisation. Interestingly, T and D-T plasmas show an improved core confinement time compared to H and D plasmas even for matched pedestal pressures. For T, this improvement is largely due to the unique pedestal composition of higher densities and lower temperatures than H and D. With a reduced gyroBohm factor at lower temperatures, more turbulent drive in the form of steeper gradients is required to transport the same amount of heat. This picture is supported by quasilinear flux-driven modelling using TGLF-SAT2 within Astra. With the experimental boundary condition TGLF-SAT2 predicts the core profiles well for gyroBohm heat fluxes >15, however, overestimates the heat and particle transport closer to the turbulent threshold.

Keywords: H-mode, tritium, heat transport, particle transport, stability, isotopes

(Some figures may appear in colour only in the online journal)

1. Introduction

For densities and temperatures typical for magnetically confined plasmas the most favourable fusion cross sections are those of reactions between the hydrogen isotopes deuterium (D) and tritium (T). Therefore, since the beginning of research with magnetically confinement devices like tokamaks one question was always investigated: how does the mass number of the main ions A impact the physics of the plasma? Answering this question is fundamental to transferring knowledge gained in experiments and modelling with the lighter isotopes H and D towards D-T fusion plasmas. Early on it was quite clear that the multitude of different observations [1] cannot be explained with just a single physics concept, but they require the interplay of multiple mechanisms. One crucial challenge with investigating isotope mass related physics is that it is extremely difficult to vary just the isotope mass in experiment. If the temperature or density changes with the isotope these differences in experiments might be dominating the results, which makes it difficult to quantify the subdominant mass dependence. Additionally, the relevance of these changes can vary depending on the plasma regime.

In both electron heated L-mode and ohmic plasmas it was found that the electron-ion equipartition's mass dependence can cause a change in confinement time [2–4]. By adjusting the heating mix or reducing the density to diminish the importance of the equipartition, this mass dependence can be altered. When the equipartition does not play a role the core transport in L-mode can be found without mass dependence [5]. It is speculated that zonal flows, more precisely, geodesic acoustic modes (GAMs) might have an impact on the mass dependence of transport. In the edge of ohmic [6] and L-mode plasmas [7] the GAM amplitude was found to change with isotope mass. However, in the H-mode edge the drive of the GAMs is strongly reduced, due to reduced turbulence levels, up to a point where their amplitude cannot be measured anymore [8]. Up to now, there is no experimental evidence in H-mode plasmas, neither in the core nor in the edge, which indicates a mass dependence in the zonal flow activity.

In H-mode plasmas, the coupling between core and edge is essential to understand the observed plasma states [9]. We know that the H-mode pedestal shows a strong isotope mass dependence where plasmas with heavier hydrogen ions have higher pedestal top pressures [10–18]. To investigate the core transport experimentally, matched pedestal conditions are ideal, but we must offset the pedestal mass dependence to achieve this. Varying the heating power is one option [12, 13], but, then profile stiffness [19] and the associated power degradation will play an important role causing the relative relevance of A to decrease and the uncertainties in the measured mass dependence to increase. Adjusting the gas fuelling to offset the edge mass dependence will also influence the global confinement [9, 13, 16]. A third method is adjusting the plasma triangularity [16, 18], which appears to be the least invasive of the three methods, as its impact on the pedestal is more pronounced than its potential influence in the core. Although the plasma shape can affect core heat transport [20], its influence is less significant.

With matched edge conditions we can find experimental regimes with a very weak mass dependence in the core [10, 11, 18] and those with a strong mass dependence [16, 21, 22]. In the more recent studies with a strong mass dependence

in AUG and JET-ILW plasmas [16, 22] this could be attributed to a higher fast-ion content in plasmas with heavier main ions. These differences arise due to different heating methods and the mass dependence in the fast-ion slowing down. This fast-ion turbulence stabilisation is also a potential explanation why D-T supershots in TFTR exhibited a stronger mass dependence in the core than pulses with less heating power [21].

The story of the mass dependence in theory is not less diverse than the experimental observations. Depending on the dominant turbulence type the mass dependence is expected to be different. In general, theoretical mass dependencies are quantified relative to the microturbulence or gyroBohm scaling [23] with the gyroBohm diffusivity $\chi_{\mathrm{gB}} \propto T^{1.5}A^{0.5}/(RB^2)$ or the gyroBohm heat flux $q_{\mathrm{gB}} \propto T^{2.5}A^{0.5}n/(R^2B^2)$ where T is the plasma temperature, n the plasma density, R the major radius and B the magnetic field. Since, the hereby predicted increased transport with higher isotope mass is not observed experimentally, theory often tries to explain which physics mechanisms can cause such a gyroBohm breaking or anti-gyroBohm scaling—i.e. having a heat transport that reduces with increasing mass.

For the ion temperature gradient (ITG) driven turbulence, which is also dominant in the core of the plasmas discussed here, we expect a gyroBohm mass scaling only in the collisionless limit [16, 24]. Collisions, electromagnetic (EM) effects and $E \times B$ shearing $\gamma_{E\times B}$ can introduce mass dependencies [25] which can ultimately cause a gyroBohm breaking [24], where E is the radial electric field. Since the importance of these mechanisms can greatly vary for different experimental conditions—i.e. flat rotation profile vs. peaked rotation profile—so does the expected mass dependence. For trapped electron mode turbulence a weakening of the gyroBohm mass dependence can be caused by zonal flow regulation of the turbulence when $T_{\mathrm{e}} \sim T_{\mathrm{i}}$, for $T_{\mathrm{e}} \gg T_{\mathrm{i}}$ the mass scaling is again gyroBohm like [26].

The plasma collisionality is an important quantity for heat and particle transport. When changing the isotope mass, it becomes of particular interest to distinguish between the ion–ion and the electron–ion collisionality. This distinction plays a less critical role for mono-isotopic studies. The ion–ion collisionality $\nu_{\mathrm{i}\star} = \nu_{\mathrm{ii}}/(\epsilon\omega_{\mathrm{bi}})$ is mass independent, where ν_{ii} is the ion–ion collision frequency, ω_{bi} the ion bounce frequency and ε the aspect ratio. The electron–ion collisionality $\nu_{\mathrm{eff}} = \nu_{\mathrm{ei}}/(c_{\mathrm{s}}/R) \propto (m_{\mathrm{i}}/m_{\mathrm{e}})^{0.5}$ is mass dependent, where ν_{ei} is the electron–ion collision frequency and $c_{\mathrm{s}} = (T/m_{\mathrm{i}})^{0.5}$ the ion sound speed. Note, in some representations the thermal electron velocity is used for the normalisation which results in the mass independent electron collisionality $\nu_{\mathrm{e}\star}$. The electron–ion collisionality is particularly important for the density peaking in the plasma core which was first discovered on AUG [27] and repeatedly confirmed [28–32]. Theoretical results show that with increasing electron–ion collisionality the turbulent particle pinch produced by trapped electrons in low collisionality ITG turbulence is reduced [33]. The mass dependence in ν_{eff} then suggests a lower density peaking for heavier main ions [34].

In the plasma edge of L-modes, where the density gradients are steeper than in the core, collisional drift waves can become dominant and the finite electron-to-ion mass-ratio dependence of the nonadiabatic electron response introduces an anti-gyroBohm like mass dependence of the transport [35, 36]. In the H-mode pedestal also the temperature gradients increase and electron temperature gradient (ETG) driven turbulence can contribute significantly to the electron heat flux while showing no mass dependence [37]. However, for these H-mode pedestal parameters, the ITG turbulence drives strong anti-gyroBohm heat fluxes due to differences of $\gamma_{E\times B}$ when varying the mass. In the steep gradient region, the neoclassical transport also contributes to the heat and particle transport and has a more gyroBohm like mass dependence, such that in the total heat transport the opposite mass dependencies cancel out [37]. The total particle transport retains the mass dependence of the ITG turbulence since the neoclassical particle transport is mostly mass independent [37].

The unifying feature of all those theoretical studies is that no universal mass scaling of the transport is expected, but the mass dependence will change with the actual plasma regime that is considered. This is consistent with the variety of experimental observations and highlights the importance to perform experiments using pure T and D-T mixtures and not entirely relying on extrapolations from H and D plasmas.

This is also the reason why dimensionless identity and similarity studies [38] will only yield the mass dependence of heat and particle transport for the chosen values of dimensionless parameters. Based on our current theoretical understanding of plasmas, that deviate from an ideal collisionless case with adiabatic electrons, we do expect the mass dependency in the transport to be dependent on the dimensionless parameters itself—$T_{\mathrm{e}}/T_{\mathrm{i}}$ [2, 26], $\nu_{\mathrm{e}\star}$ [35], R/L_n [36], $W_{\mathrm{fast}}/W_{\mathrm{th}}$ [16] with the density gradient length L_n and stored energy of fast ions W_{fast} and thermal particles W_{th}. In L-mode this is observed in JET-ILW where two different dimensionless identity experiments yield different mass dependencies for the core transport [5, 39]. In H-mode there is the extra difficulty that no complete set of dimensionless parameters exists which can describe the core and edge plasma simultaneously. We will present examples of the reason behind this throughout this paper.

To quantify the impact of the isotope mass on heat and particle transport it is important to minimise secondary effects due to experimental differences and take the differences into account in the interpretation where they are unavoidable. The dynamic nature of the H-mode pedestal with edge localised modes (ELMs) and the coupling of the core and edge transport regions and the coupling of electron and ion transport channels are prime examples of interactions which need to be taken into account. This results in a complex system of often non-linear interactions which need to be modelled. The high-fidelity theoretical models discussed above are not suited for this purpose, where full radius flux-driven modelling is required. Instead, we rely on the quasilinear TGLF-SAT2 [40] model which does not simulate the full non-linear physics

but utilises linear growth rates and estimates heat and particle fluxes based on a saturation rule—here SAT2. SAT2 is optimised based on the solutions of non-linear CGYRO [41] simulations over a wide range of parameters. However, it was calibrated on deuterium plasmas. While this reduced model is not expected to capture the full physics it should reproduce the leading contributions to heat and particle transport. Recently, an extension to the saturation rule 2 has been proposed in the form of SAT3 [42] which captures the gyroBohm breaking CGYRO predicts for high density gradients $a/L_{ne} > 2.0$ [36] where a is the minor radius. $a/L_{ne} > 2.0$ corresponds to the steep gradient region in the pedestal which is in contrast to the core region with $a/L_{ne} < 1.0$. In the core also Sat2 captures the mass dependence suggested by CGYRO which is a bit stronger than gyroBohm like [42].

State of the art would be to use integrated models which couple scrape-off-layer, pedestal and core [43]. However, these lack flexibility in testing the individual mass dependencies and we know that parts of the models do not capture isotope physics well. In particular, the pedestal part of the model which relies on ideal peeling-ballooning (PB) stability does not reproduce the observed isotope mass dependencies [17]. Therefore, we investigate the pedestal and core separately while also quantifying the coupling between both.

In section 2 we will describe how the experiments are performed in the JET tokamak and discuss basic engineering constraints that arise when operating with different isotopes. The main part of the paper is divided into the edge and core parts. For each we present experimental observations and the associated modelling. The consequences of observations and modelling are discussed together in the edge and core discussion sections. The key results of this paper are then summarised in section 9. In the appendix we give more details on the analysis procedures used to obtain the presented data and describe the pedestal model used in section 4.1. Throughout the paper, we will apply the following color scheme for the different masses H: red/circle, D: blue/square, D-T: gold/star, T: purple/diamond. When we scan parameters other than the mass we will use brown, lime and grey with the symbols triangle-down, circle, triangle-up.

2. Experimental setup

The scenario used for this experimental study is a type-I ELMy H-mode with a plasma current of $I_p = 1.4$ MA, a magnetic field of $B_t = 1.7$ T, an edge safety factor of $q_{95} = 3.7$ and the corner–corner (CC) divertor configuration. This type of plasma has been extensively studied at JET [9, 14, 18, 44–47] and its properties in hydrogen and deuterium are well known. The main reason for choosing this type of plasma is the relatively low heating power 12–15 MW required to reach high plasma pressure, this allows for reasonable flexibility and it is possible to scan the normalised total plasma pressure β_N from 1.0 up to 3.0. In the CC divertor configuration, with the inner and outer strike points positioned in their respective divertor corners close to the pumping ducts, low densities are accessible which are required to reach high

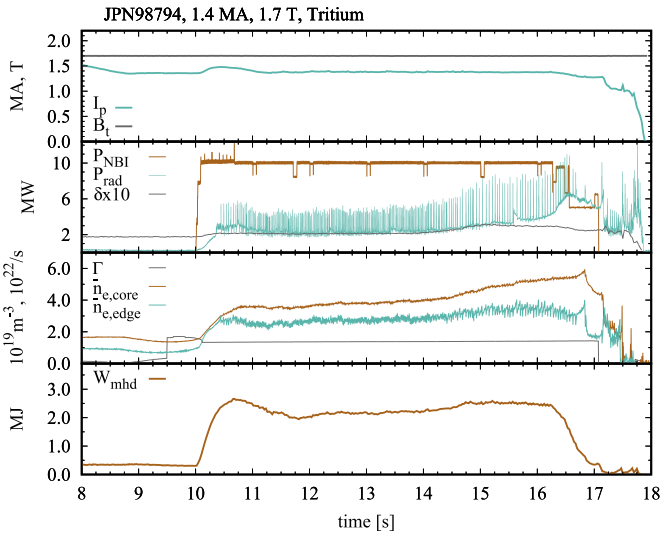

Figure 1. Time traces for a typical plasma pulse in T, from top to bottom plasma current I_p and magnetic field B_t, auxiliary heating power P_{NBI} and radiated power P_{rad} and average triangularity δ, core and edge line averaged densities $\bar{n}_e$ and the gas flow rate Γ, total plasma stored energy W_{MHD}.

β_N. Additionally, the CC configuration is commonly used for most experiments and consequently, those divertor tiles are relatively clean which is beneficial for the reproducibility of experiments. Experiments that utilise more uncommon divertor configurations often need to spend time on conditioning the divertor tiles first to ensure reproducible conditions.

Pulse setup: a typical setup for a plasma pulse is illustrated in figure 1. Each pulse is identified via a JET pulse number (JPN). In the current flattop phase, constant heating power is applied along with a constant gas fuelling. The flattop is divided into a low triangularity δ phase up to 14.0 s and a high δ phase starting at 15.0 s. Highly shaped plasmas or those with high β_N tend to not reach the planned termination due to impurity accumulation. The profile and transport analysis is then performed for the longest stationary phase before the onset of impurity accumulation. These phases typically have a length of $>10\tau_E$ where τ_E is the energy confinement time, however, at $\beta_N = 3.0$ the length goes down to $2\tau_E$.

Heating: the auxiliary heating power by neutral beam injection (NBI) P_{NBI} for our data set is varied from 3 up to 15 MW with the bulk of the experiments performed at 10 MW which results in a type-I ELMy H-mode for all main ion masses. The NBI species is D for most H and all D plasmas and T for the T plasmas. In DT both D- and T-NBI are utilised. The power calibration for D and T NBI is accurate within 10% [48]. Due to the low plasma density the NBI needs to be operated at reduced voltage $\leqslant$100 kV and reduced power per injector to avoid excessive NBI shine through. Along with the less than 100% availability of the neutral beams, this prevented a sophisticated optimisation of the heating profiles for the different NBI and main ion species. The power density to electrons and ions due to NBI as calculated with the NUBEAM [49] package within the TRANSP [50] code is illustrated for the different

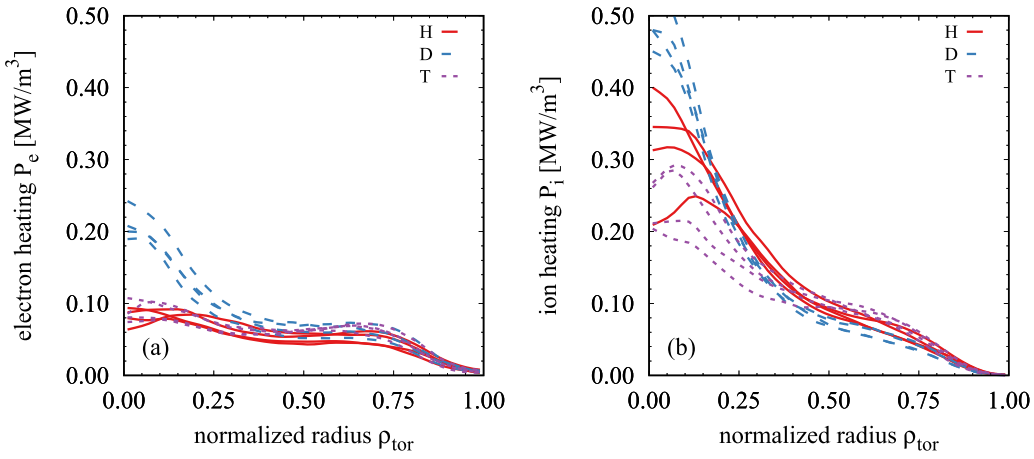

Figure 2. Electron and ion heating for $P_{\mathrm{NBI}} = 10\,\mathrm{MW}$ for different isotopes and densities.

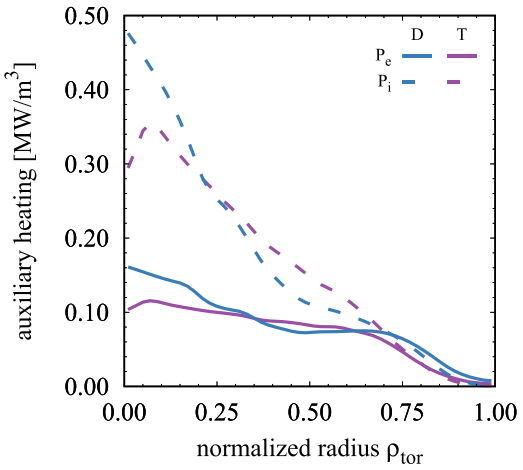

Figure 3. Electron and ion heating for $P_{\mathrm{NBI}} = 13\,\mathrm{MW}$ for T-NBI into T (JPN99224) and D-NBI into D (JPN97512) at similar densities.

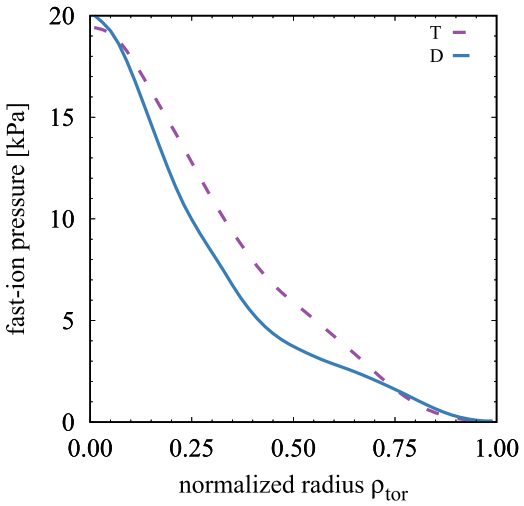

Figure 4. Fast-ion pressure for $P_{\mathrm{NBI}} = 13\,\mathrm{MW}$ for T-NBI into T (JPN99224) and D-NBI into D (JPN97512) at similar densities.

isotopes with varying density and $P_{\mathrm{NBI}} = 10\,\mathrm{MW}$ in figure 2. Despite the lack of dedicated optimisation the heat profiles are well matched for $\rho_{\mathrm{tor}} > 0.3$ for all three isotopes and for H and T over the whole radius (for the definition of the radial coordinate see appendix A). The D pulses tend to have more peaked heating profiles in the very centre. This is due to the different mean free paths of H, D and T neutrals in the plasma. While H neutrals are ionised on low and high field side, the birth distribution of fast NBI ions shifts towards the low field side with higher mass. However, due to the smaller volume for $\rho_{\mathrm{tor}} < 0.3$ the central heating amounts only to 30% of the total heating despite having more than five times the power density than at the outer radii. The differences in the heating profiles are taken into account in the modelling.

At the higher heating powers 13 MW, which are required to reach high β_{N}, the heat deposition is fairly similar due to overall higher plasma density which shifts the birth distribution of D ions away from the centre. This is illustrated for D and T plasmas in a matched density case in figure 3. Note the higher ion heating due to the NBI in all cases. In the DT plasmas also α heating due to D-T fusion reactions might play a role, however, for the parameters discussed here this is estimated to be only around 0.15 MW which is below 2% of the total heating power and will be neglected in the analysis. The fast-ion pressure calculated by TRANSP for the density matched plasmas in D and T is shown in figure 4, while the relative fast-ion energy is quite similar with $W_{\mathrm{fast}}/W_{\mathrm{th}}\,|_{\mathrm{D}} = 0.22$ and $W_{\mathrm{fast}}/W_{\mathrm{th}}\,|_{\mathrm{T}} = 0.24$, there are differences in the fast-ion pressure gradients at the outer radii.

Gas fuelling: the gas fuelling during the current flattop phase is done with divertor valves. For the gases hydrogen, deuterium and neon the standard gas introductory modules can be used, for tritium only the tritium introductory modules (TIMs) are available [51]. This introduces an operational difference regarding fuelling with T compared to other gases. The TIMs are farther away from the main plasma chamber, therefore, there is a considerable delay between the valve opening and the gas arriving at the plasma boundary. When using TIMs the timing of the valve openings is adjusted to minimise an impact

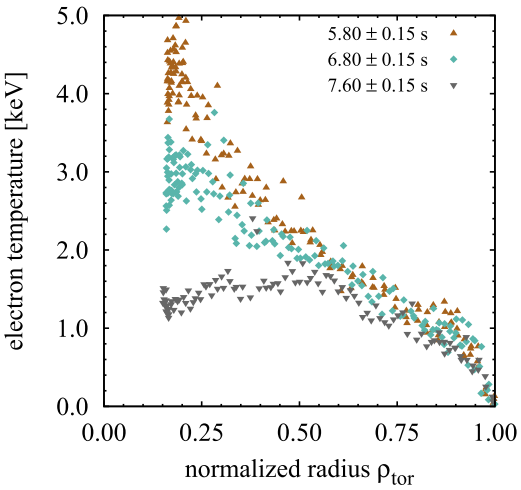

Figure 5. Sequence of impurity accumulation in JPN96830 at $\beta_N = 2.55$: stable electron temperature profile until 6.3 s, influenced by 3/2 mode at 6.8 s, hollow T_e profile at 7.6 s.

due to differences in the gas flow. Details on the impact of this time delay can be found in [52]. The auxiliary gas fuelling is adjusted depending on the plasma pressure, for moderate pressures of $\beta_N \leqslant 2.2$ the plasmas are quite resilient against impurity accumulation and we run the gas scans with three different gas fuelling levels $0.8 \cdot 10^{22}$, $1.3 \cdot 10^{22}$ and $1.8 \cdot 10^{22}$ particles s^{-1}. For higher pressures $\beta_N \geqslant 2.5$ all of the plasmas developmagnetohydrodynamic (MHD) modes which have a negative impact on the impurity balance in the plasma [53]. This can result in a negative feedback loop ending in a radiative collapse due to impurity accumulation. The impact of such a sequence on the electron temperature profile is illustrated in figure 5. From a mode analysis using Mirnov coils, we know that a sawtooth triggers a $n = 3$, $m = 2$ mode at 6.3 s. While the temperature profile is stable and peaked before the mode onset at 5.8 s, the impact of the magnetic island is visible at 6.8 s in the temperature profile between a normalised radius of 0.4–0.6. Already $3\tau_E$ later so many high-Z impurities have accumulated in the core to result in a hollow T_e profile. At the magnetic field of 1.7 T no favourable source of local heating is available at JET to stop this negative feedback loop. It does not help that at these densities the T pulses tend to have less central NBI heating than their D counterparts. Therefore, in the presented experiments the impurity control is done via the gas fuelling which impacts the ELM frequency f_{ELM}. With a sufficiently high f_{ELM} the impurity flux arriving in the core is moderated down to tolerable levels. Consequently, no fixed gas fuelling rates are applied for the high β_N plasmas.

Isotope purity: for the comparison of plasmas in H, D and T the goal is to have the highest possible isotope purity which is achievable with the JET Be/W wall. However, a perfectly pure plasma is experimentally not feasible. All plasmas will have a minimum of 1%–2% hydrogen which can be a legacy of H fuelling to facilitate ion cyclotron minority heating or from the H prefill gas used for the T plasmas. Some of the hydrogen plasmas presented here were performed during the D campaign, therefore, while the D was cleaned off the walls by H-D mixture experiments in advance, some residual D remained. A more relevant impact was the usage of D-NBI in these plasmas to achieve higher NBI power than possible with H-NBI, where technical issues limit the maximum NBI power to 10 MW [14]. This resulted in concentrations of $n_H/(n_H + n_D) \sim 0.9$ with the hydrogen and deuterium densities n_H and n_D. Still, for all metrics discussed in this paper, these plasmas exhibit no differences to plasmas with higher H concentrations. For the T campaign more time was allocated to clean the vacuum vessel of residual D in order to reduce the 14 MeV neutron production to below 1%, due to D-T neutron budget restrictions for the following DTE2 campaign. Concentrations of $n_T/(n_H + n_D + n_T) > 0.98$ where achieved. Additional to the main hydrogenic ions the plasma contains low-Z impurities which can dilute the main plasma and are mainly beryllium, carbon and neon. Due to the metallic wall, the impurity content is generally quite low. We find the effective charge number Z_{eff}, as measured by visible bremsstrahlung spectroscopy, with $Z_{eff} < 1.5$. There have been some issues with the calibration of this diagnostic, however, due to the overall low impurity content the impact on the ion density profiles due to uncertainties in Z_{eff} is expected to be well below 10%. High-Z impurities like tungsten do not dilute the main plasma due to their low concentrations, however, they contribute to the radiated power as discussed below.

Plasma shape: another parameter that is varied in the experiment is the plasma shape, in particular, the plasma triangularity δ which is known to have a significant impact on the pedestal for these 1.4 MA, 1.7 T plasmas [47]. While changing the triangularity extra care was employed to keep the divertor configuration constant and the strike points in the corner position. Effectively this means only the upper triangularity is varied, while the lower triangularity remains the same. This is relevant because changing the strike point position will have a considerable impact on the fuelling characteristics [54]. The flux surfaces of the two shapes which are used in this work are illustrated in figure 6. The corresponding triangularities are low $\delta = 0.20 \ldots 0.25$ and high $\delta = 0.29 \ldots 0.32$ where the variation within each set is due to the Shafranov shift of the plasma centre with different plasma pressures. Where we define the average triangularity as $\delta = (\delta_{up} + \delta_{low})/2$ with the upper triangularity δ_{up} and the lower triangularity δ_{low}. Since δ_{low} is kept constant most of the variation in the average δ originates in changes of δ_{up}. Note that this variation of δ, while it has an impact on the plasma, is not comparable to the impact of a high δ up to 0.6 in a machine like DIII-D [55]. It is also small compared to the variation of δ where an impact on the heat transport was observed in TCV [20], in TCV the transport was enhanced with more positive δ. A directly measurable impact due to the different δ is in the particle flow balance between inner and outer divertor. Langmuir probe data suggests that the ion fluxes towards the inner divertor decrease by 10%–100% with higher δ while the fluxes to the outer divertor stay the same within the uncertainties of ±30%.

Radiation: the core radiated power in these JET-ILW plasmas is dominated by the high-Z impurity tungsten which contributes about 95% of the total radiated power. Observations

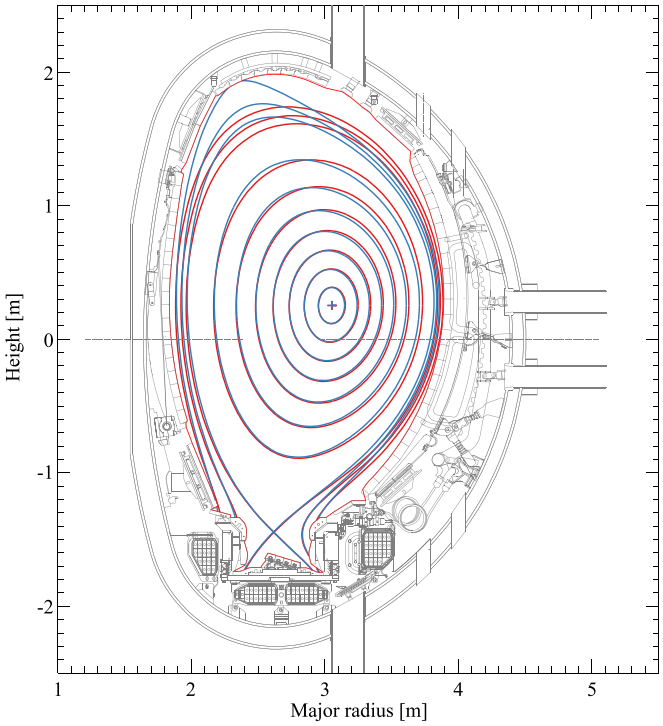

Figure 6. High and low triangularity shapes where only the upper triangularity is varied.

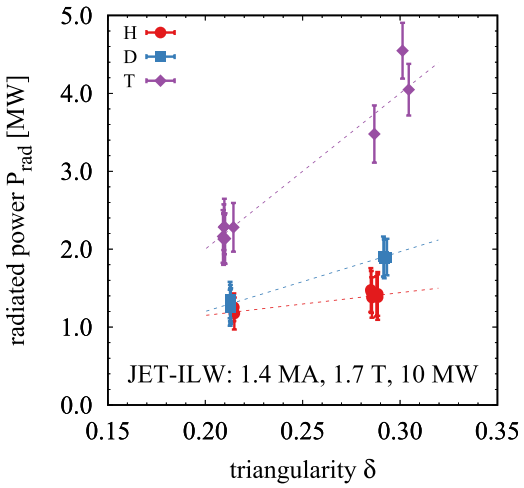

Figure 7. Bulk plasma radiated power at different triangularities for H, D and T.

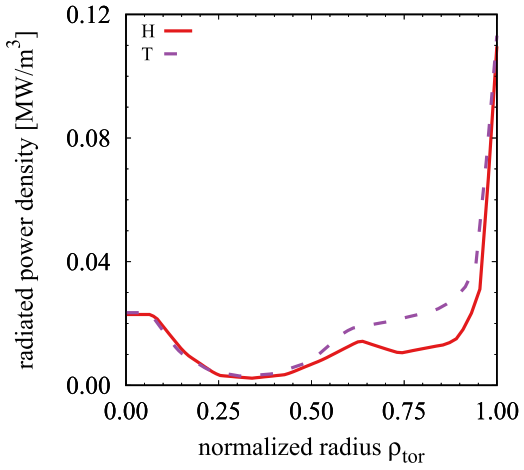

Figure 8. Radiated power density profile for an H and T with the same auxiliary heating power at matched densities (see figure 33).

in H and D show the impurity confinement to increase with larger main ion isotope mass. To mimic the impurity behaviour of a plasma with a heavier isotope experiments with a lighter isotope but higher triangularity were executed. This works quite well for H and D, a high δ H plasma has the same bulk radiated power $P_{\mathrm{rad,bulk}}$ as a low δ D plasma. However, despite D and T having a smaller relative mass difference, the high δ D plasmas designed to mimic low δ T conditions still exhibit lower bulk radiation than their T counterparts. In figure 7 an overview is given for all three isotopes, the high δ T plasmas partly suffer from impurity accumulation as discussed above, therefore, the scatter of $P_{\mathrm{rad,bulk}}$ is larger there. Despite similar auxiliary heating power, the T plasmas will have lower heat fluxes by 0.5–1.0 MW. Most of this difference is expected to originate from the edge plasma with $\rho_{\mathrm{tor}} > 0.7$ which accounts for 70% of the total radiated power. This is shown in figure 8 where we compare tomographic reconstructions of bolometer measurements for H and T plasmas with a pedestal density match. To take the different radiation into account we introduce the power over the separatrix $P_{\mathrm{sep}} = P_{\mathrm{heat}} - \partial W/\partial t - P_{\mathrm{rad,bulk}}$, where $P_{\mathrm{heat}} = P_{\mathrm{NBI}} + P_{\mathrm{ohm}}$, with P_{ohm} being the ohmic heating power, the changes in the stored energy $\partial W/\partial t$ are negligible during the stationary phases discussed here. The impact of impurity dilution of the plasma due to the tungsten is negligible. This follows from an estimate using tungsten cooling factors L_{W} [56]. The radiation density is $p^{\mathrm{W}}_{\mathrm{rad}} = n_{\mathrm{e}}^2 c_{\mathrm{W}} L_{\mathrm{W}}$ and assuming all radiation to be from tungsten we get at an upper limit for the tungsten concentration of $c_{\mathrm{W}} = 7 \cdot 10^{-5}$ when using an electron density $n_{\mathrm{e}} = 4 \cdot 10^{19}$ m^{-3} and $P_{\mathrm{rad}} = 4$ MW. With a charge of 40 this still translates to a dilution of <0.003 which is well below the uncertainty of the light impurity concentrations, additionally, the difference between H, D and T is even smaller.

3. Pedestal characteristics

Overview: we have two main sets of data in H, D and T, one at high $\beta_{\mathrm{N}} = 2.5 \ldots 3.0$ and one at medium $\beta_{\mathrm{N}} = 1.4 \ldots 2.5$. The aim of the first one is to obtain a comparison at high β_{N} with different isotopes and heating powers between 12 and 15 MW. At 10 MW of heating and medium β_{N} we have more operational flexibility and scan gas puff and triangularity. For the latter data set also a few DT pulses close to a ratio of $n_{\mathrm{D}}/n_{\mathrm{T}} \sim 50/50$ are available, although, only at a constant low gas puff.

The gas puff scan at 10 MW of heating and low δ is shown in figure 9(a) and significant differences between the three isotopes are observed. While for T the gas scan increases the density at constant pressure, the increase of density in D is

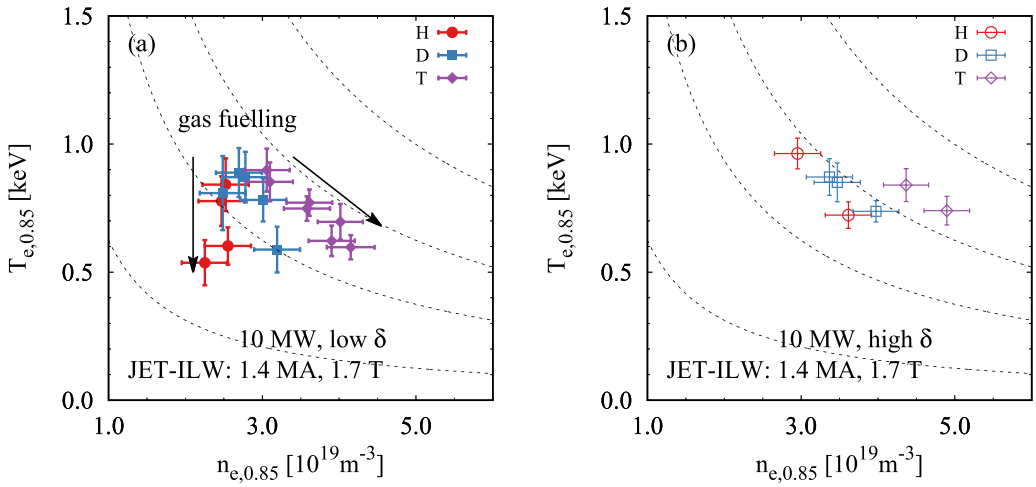

Figure 9. Edge electron temperature—determined at $\rho_{tor} = 0.85$—plotted against the electron density at the same position for different main ion isotope masses and gas fuelling, but otherwise identical engineering parameters. In (*a*) the low δ data is plotted and in (*b*) the one at high δ. The dashed lines are isobars at 1, 3, 5 and 8 kPa.

accompanied by a reduction in pedestal pressure. In hydrogen the impact of the gas puff does not result in a higher density at the pedestal top, but in the temperature and pressure dropping significantly. This is evidence of a strong isotope mass dependence in the pedestal. This isotope mass dependence does not follow a simple power law. If we were to express the mass dependence of the density at low gas fuelling as a power law it would yield $n_e \propto A^{0.13}$ while at high gas fuelling we find $n_e \propto A^{0.39}$. From figure 9(*a*) it is also evident that both scalings are significantly different. Such a deviation from a single power law description is also observed when varying the triangularity. At high δ the pressure remains constant with gas fuelling for all three isotope masses. This is quite different from the observation at low δ, where a clear mass dependence was observed between H and D as well as D and T. While at high δ the T pedestal is still found at higher pressures compared to H and D, the pressure differences between H and D are negligible, despite the larger mass ratio. Note that at high δ H and D pulses are found with a similar pedestal density and temperature compared to the low δ T pulses, which will become important for the comparisons in the core.

At high β_N the interpretation of the overview plot of edge temperature and density, shown in figure 10, is not as straightforward because we vary heating power, gas and shape at the same time. The main goal to match temperature and density at the pedestal top for all three isotopes was not achieved, however, we have a pair at constant pressure and one at constant density. High pressure H plasmas are only achieved at high triangularity and with D-NBI, the low pressure H points reached the heating powers above 10 MW with H-NBI and ion cyclotron range of frequencies (ICRF) heating and had low δ.

A very strong correlation is observed between the pedestal pressure and the ELM frequency. Figure 11(*a*) shows for a subset of the database at 10 MW that at lower pedestal pressure the highest f_{ELM} are found. For the whole database a similar correlation between f_{ELM} and the pedestal confinement time $\tau_{th,ped} = W_{th,ped}/P_{sep}$ is visible in figure 11(*b*). For the thermal stored energy W_{th} we define the core $W_{th,core}$ and pedestal

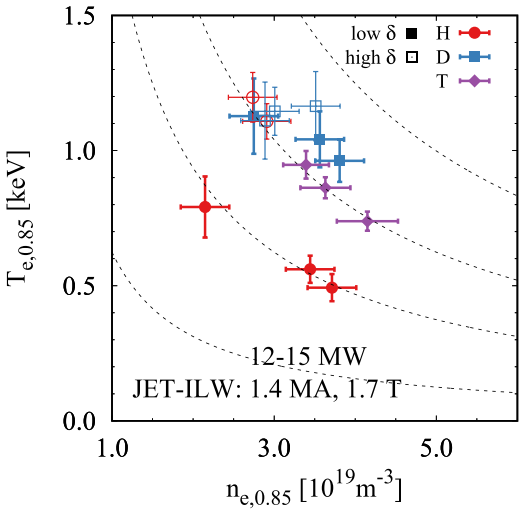

Figure 10. Edge electron temperature—determined at $\rho_{tor} = 0.85$—plotted against the electron density at the same position for the high pressure data set with different main ion masses. The dashed lines are isobars at 1, 3, 5 and 8 kPa. Note the different heating power.

$W_{th,ped}$ contributions as $W_{th,core} = W_{th} - W_{th,ped}$ with $W_{th,ped}$ as defined in [18]. No clear separation between the isotope masses is observed in this correlation, although, the lowest pedestal confinement and highest f_{ELM} are plasmas with H as main ions which also have the most irregular ELM frequency.

Density profiles: the pedestal electron density profiles for the gas scan at 10 MW and low δ are shown for H, D and T main ions in figure 12. Most striking is the density response in H, where an increase in the separatrix density $n_{e,sep}$ with higher gas fuelling is observed, while the pedestal top density is effectively unchanged. Here the separatrix position is at $\rho_{pol} = 1.0$ and defined as described in appendix A. In D and T gas fuelling increases the pedestal top density while the

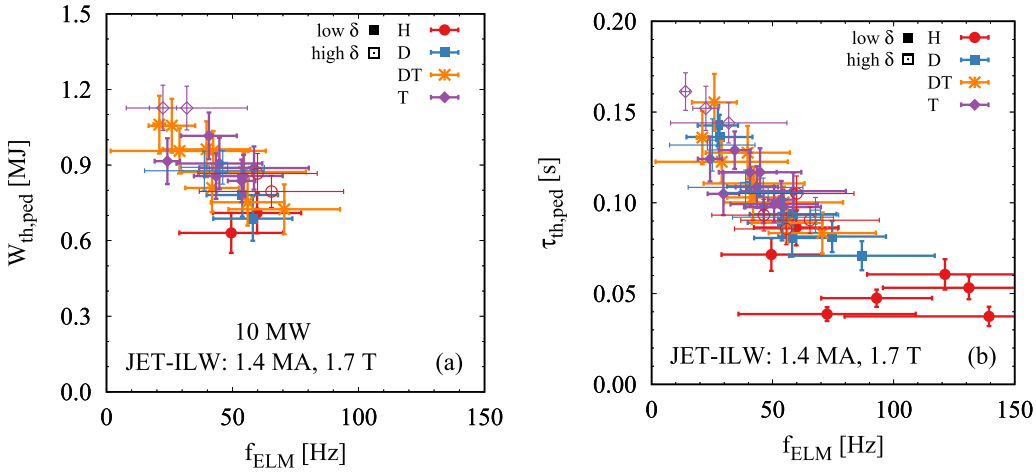

Figure 11. Pedestal stored energy (*a*) and pedestal confinement time (*b*) plotted against the ELM frequency for 10 MW plasmas in (*a*) and the whole database in (*b*).

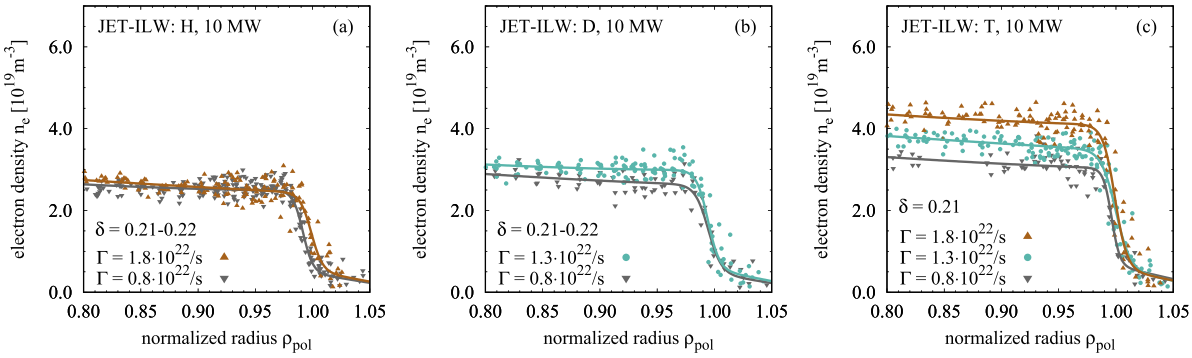

Figure 12. Edge electron density profiles at low δ for different gas puff levels and main ion mass: H (*a*), D (*b*) and T (*c*). H: JPN97094, JPN97095; D: JPN97035, JPN97036; T: JPN98794, JPN98795, JPN100177.

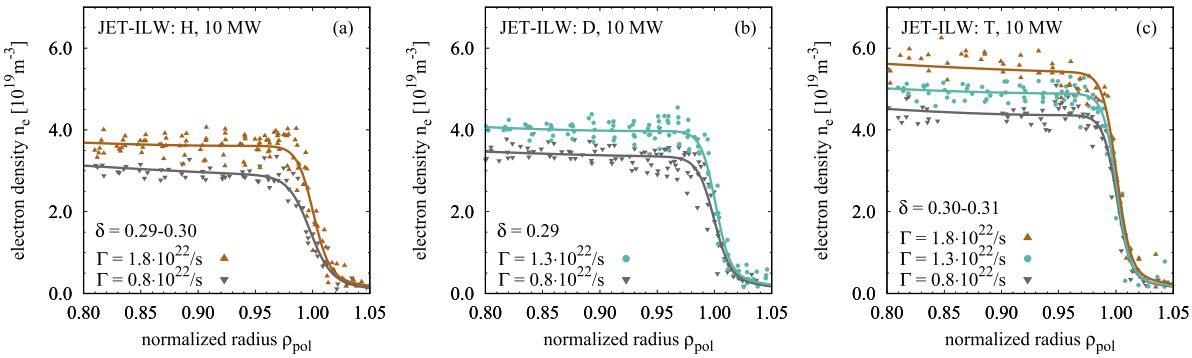

Figure 13. Edge electron density profiles at high δ for different gas puff levels and main ion mass: H (*a*), D (*b*) and T (*c*). H: JPN97094, JPN97095; D: JPN97035, JPN97036; T: JPN98794, JPN98795, JPN100177.

separatrix density appears to be less affected than in H, then the increase in pedestal top density is a result of steeper gradients. In D the data would support this, for T it is not directly evident. Overall, at low δ the changes in $n_{e,sep}$ and ∇n_e are not sufficient—given the available data quality—to pinpoint the cause for the pedestal top density values. This is different at high δ, as shown in figure 13 where the higher pedestal top density with larger gas fuelling is clearly a result of steeper density gradients, while the density at the foot of the pedestal remains relatively unchanged. In particular, it is surprising that the density is constant outside of the steep gradient region for all isotope masses despite a variation in gas puff of over a factor of 2. In the picture of the pedestal transport model discussed in section 4.1 this would correspond to an improved fuelling efficiency and higher particle capacity at high δ. Note that for our database only data from Thomson scattering is

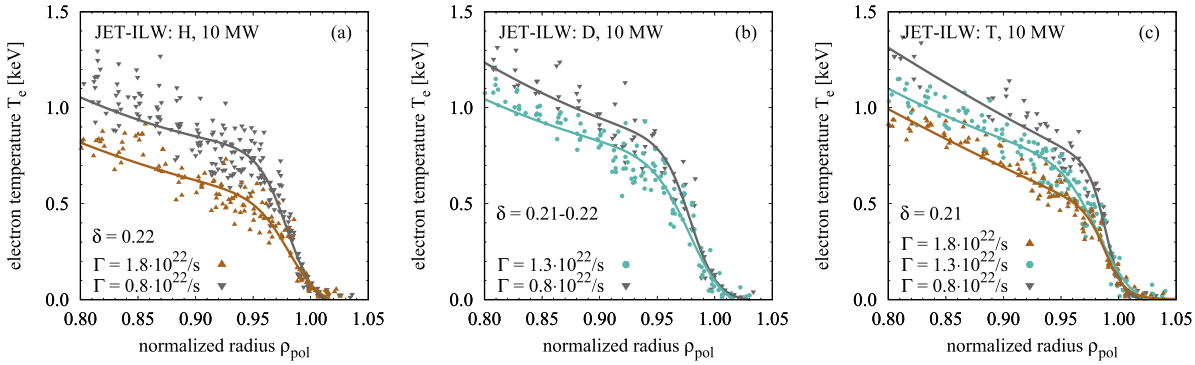

Figure 14. Edge electron temperature profiles at low δ for different gas puff levels and main ion mass: H (*a*), D (*b*) and T (*c*). H: JPN97094, JPN97095; D: JPN97035, JPN97036; T: JPN98794, JPN98795, JPN100177.

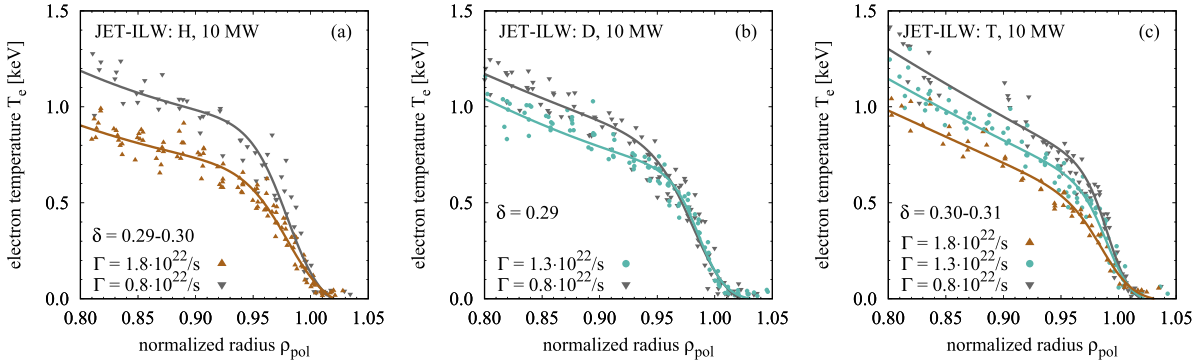

Figure 15. Edge electron temperature profiles at high δ for different gas puff levels and main ion mass: H (*a*), D (*b*) and T (*c*). H: JPN97094, JPN97095; D: JPN97035, JPN97036; T: JPN98794, JPN98795, JPN100177.

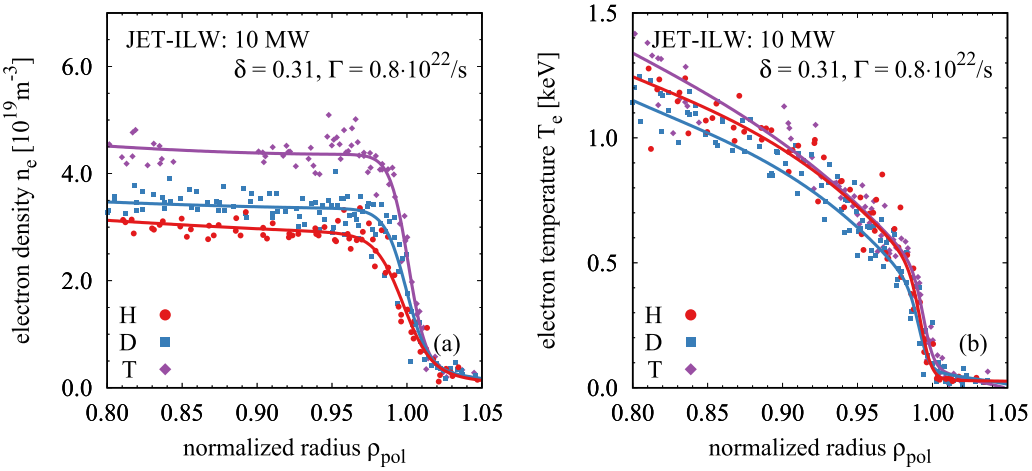

Figure 16. Edge electron density (*a*) and electron temperature (*b*) profiles of plasmas with different main ion mass H, D, T for 10 MW of heating, high δ and low gas puff. H: JPN97095; D: JPN97036; T: JPN98795.

available which has relatively large uncertainties at low densities. Measurements of the Li-beam diagnostic which would improve the accuracy of the SOL data were not available for the full data set.

Temperature profiles: the temperature response to the changes of gas fuelling is quite similar for different δ, as shown in figure 14 for the low δ plasmas and in figure 15 for high δ ones. In particular, for H, even at constant pedestal top density, the temperature drops with increasing gas puff as shown in figure 14(*a*). For all three isotopes, the temperature changes are comparable and scale with the gas fuelling level, although the changes in density were different for all isotopes. All the changes in the temperature pedestal top due to gas puffing are a result of different temperature gradients. There are no indications of a significant impact due to the pedestal width.

Impact of the isotope mass: when plotting engineering matched plasmas at high δ with all three isotopes as done in figure 16 for high δ it becomes evident that the density

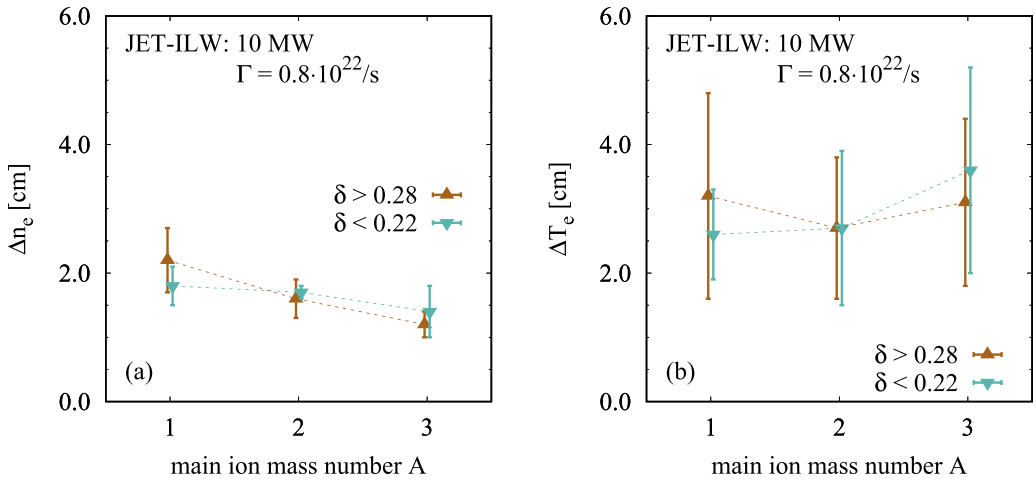

Figure 17. Pedestal electron density (*a*) and electron temperature (*b*) widths for different main ion mass at 10 MW of heating, different δ and low gas puff.

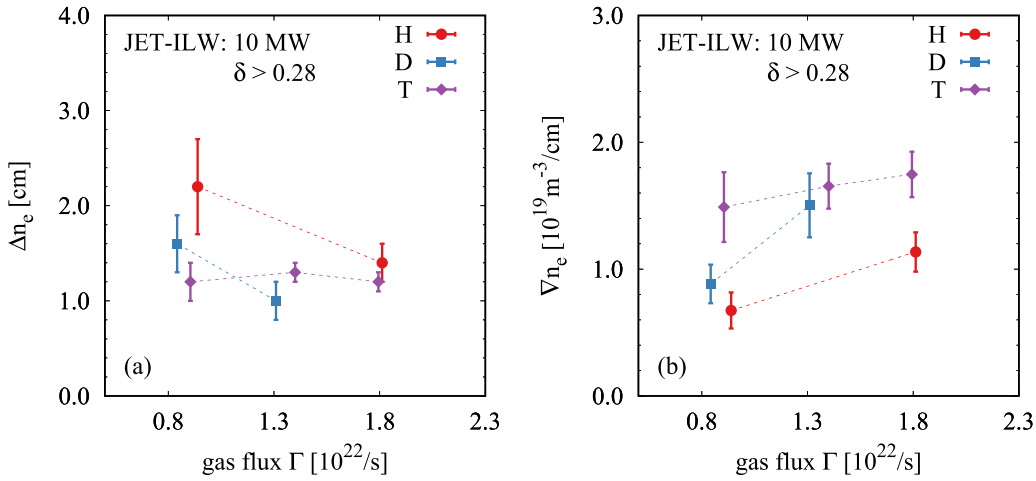

Figure 18. Pedestal electron density width (*a*) and gradient (*b*) for different main ion masses and gas puffing at 10 MW of heating and high δ.

pedestal width shrinks while its gradient increases when the mass number increases. At the same time, the temperature pedestal seems to be the same within the uncertainties for all three isotopes. However, the uncertainties are quite high since the temperature does not feature a similarly pronounced pedestal top as observed in the density. The transition between the steep gradient region and the core plasma is more gradual. In figure 17 the pedestal widths in real space coordinates are plotted against the isotope mass for low and high δ. The density pedestal width Δn_e reduces with higher mass at high δ while it remains relatively constant at low δ. The electron temperature pedestal width ΔT_e cannot be defined with the same accuracy as the density pedestal width. However, the values suggested by the bi-linear fit shown in figure 17(*b*) are similar for all isotope masses which is consistent with the profiles shown in figure 16(*b*). Nevertheless, they are higher than the pedestal widths determined with a modified hyperbolic tangent function, although both fitting methods are consistent within their uncertainties.

The impact of gas fuelling on the density pedestal widths and gradients is shown in figure 18. In T the pedestal width stays fairly constant while in H and D the pedestal becomes narrower with higher gas fuelling. The narrowing of the pedestal is accompanied by an increase of the density gradient which is larger than the reduction in the width. This leads to the higher pedestal top densities observed at high δ and increasing gas puffing—also shown in figure 13. Due to the relatively constant Δn_e in T, a smaller increase in ∇n_e is sufficient to reach higher pedestal top densities when compared to H and D. Similar trends are observed at low δ as shown in figure 19 albeit not as pronounced as at high δ.

ELM cycle: the ELM characteristics are different between the three isotopes, most prominently is the ELM frequency which changes for pulses with the same engineering. This is shown in figure 20 for the pulses at low gas and high δ already shown in figure 16, where the H plasma has an $f_{\mathrm{ELM}}^{\mathrm{H}} = 60 \pm 22$ Hz,

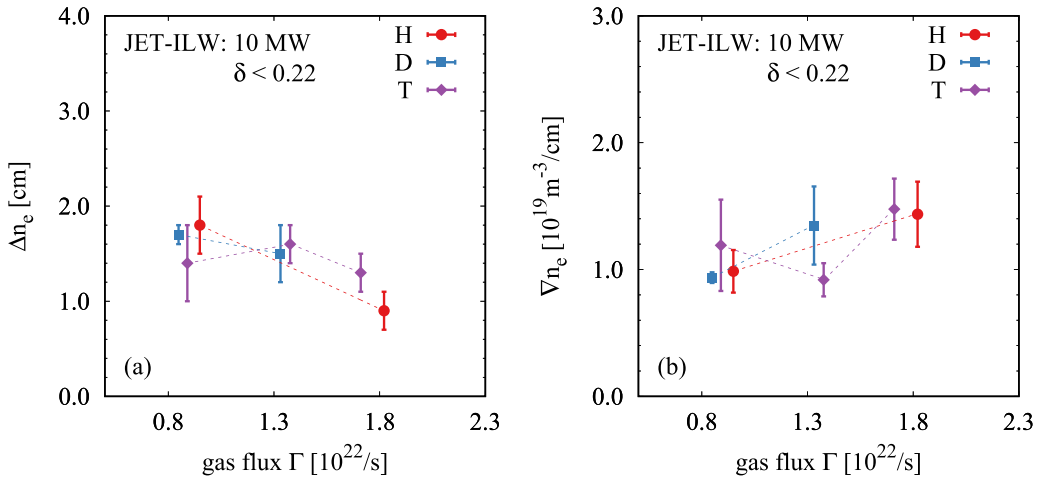

Figure 19. Pedestal electron density width (*a*) and gradient (*b*) for different main ion masses and gas puffing at 10 MW of heating and low δ.

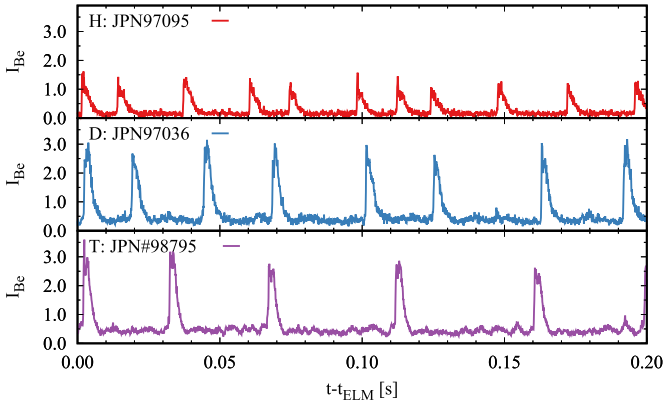

Figure 20. Time traces of the beryllium line intensity in the divertor as indicator of ELM crashes for the H, D and T. The pulses are the same as shown in figure 16.

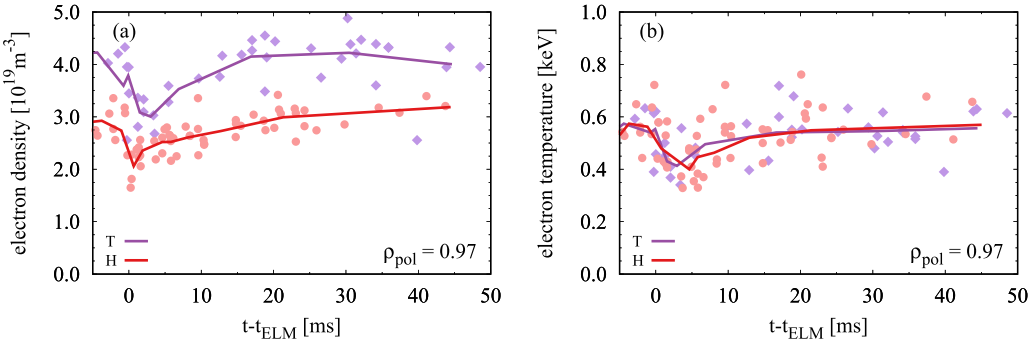

Figure 21. Electron density (*a*) and temperature (*b*) at $\rho_{\mathrm{pol}} = 0.97$ after an ELM crash for different main ion masses—H: JPN97095, T: JPN98795.

the D plasma $f_{\mathrm{ELM}}^{\mathrm{D}} = 38 \pm 24$ Hz and the T plasma $f_{\mathrm{ELM}}^{\mathrm{T}} = 32 \pm 24$ Hz. To analyse the pedestal recovery after an ELM crash we investigate the H and T plasma. In figure 21 the recovery of the density (*a*) and temperature (*b*) pedestal at $\rho_{\mathrm{pol}} = 0.97$ is shown. The data is a conditional average over multiple ELM cycles with the ELM onset time t_{ELM}. Both H and T show data up to 50 ms after an ELM crash which is the result of the irregularity of the ELM frequency, however, the T pulse exhibits more data for longer inter-ELM phases. This is due to the lower average ELM frequency. The limited temporal resolution of the Thomson scattering might obscure details of the crash, but the general trends should be recovered. The crash of the density pedestal appears to be larger in T compared to H, but the relative crash size is around 30% in both cases. The density recovers slightly faster than in T with the rate of recovery reducing after 20 ms. The temperature pedestal in H and T has fairly similar ELM crash size and recovery characteristics as shown in figure 21(*b*). The temperature at $\rho_{\mathrm{pol}} = 0.97$

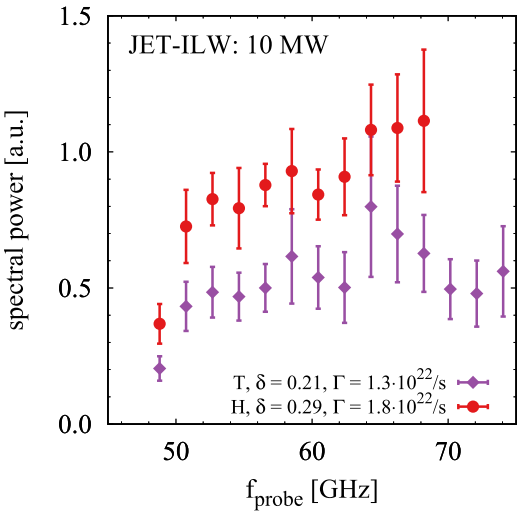

Figure 22. Spectral power for H and T pedestals plotted against the probing frequency for a density and temperature match (see figure 33).

has mostly recovered after 10 ms and only gradually increases afterwards.

Density fluctuations: as discussed in appendix A we use the spectral power measured by reflectometry at normal incidence as a proxy for density fluctuations with low wavenumbers $k_\perp$. While this will not yield absolute fluctuation levels without appropriate full wave modelling of the diagnostic [57] the relative changes are expected to be robust. We compare plasmas with matched pedestal gradients to minimise their impact on the measured signal. The resulting spectral powers are shown in figure 22, which are clearly higher for H compared to T for the whole steep gradient region. Even if the mapping from $f_{\rm probe}$ to a radial location would cause a shift between the H and T data, the observation of higher spectral power in H would hold. Some of the H points at higher $f_{\rm probe}$ are missing because there the Doppler shifted Doppler backscattering signal starts to dominate again. This indicates that a different part of the turbulent spectrum is observed which is not comparable anymore.

4. Pedestal modelling

4.1. Pedestal transport model

As discussed in the introduction the consistent treatment of the different transport channels and their interdependence is important. Therefore, we built a transport model using only very basic well-known physics constraints. The novelty in our approach is that we implement those constraints in a coupled self-consistent source-driven full radius model including heat and particle transport channels. The model is run within the Astra code which also captures the temporal evolution. This allows us to understand trivial dependencies, which otherwise might be obscured by the complexity of the non-linear interactions between the transport channels. The purpose of the model is not to predict plasma parameters but to illustrate the chain of consequences that changes will set off in a coupled environment such as a fusion plasma. A detailed description of the model can be found in appendix B, in the remainder of this section only the key results will be highlighted.

In the model the heat and particle transport is gradient driven, but will be reduced when the local $\gamma_{E\times B}$ exceeds a critical shearing rate. The isotope mass enters in the model only in the plasma edge via the neutral penetration and an empirical transport enhancement factor of the form $D \propto \chi \propto A^{\mu}$. μ will be varied in the simulations to mimic a potential mass dependence of the transport. The model can be run in two configurations a transport limited one and a stability limited one. Since we are only considering type-I ELMy H-modes, the transport limited case would correspond a to quasi-stationary phase before an ELM crash. The stability limited configuration corresponds to a dynamic simulation of ELM cycles, where the critical normalised pressure gradient $\alpha_{\rm crit}$—at which ELMs are triggered—is an input to the model.

The key difference between these two configurations is in the impact of μ on the results. In the quasi-stationary case varying μ will have a strong impact on the pedestal profiles. For a mass independent transport with $\mu = 0$, the plasma with lower main ion mass is found at higher density and higher pressure. This is shown in figures 23(a) and 24 and it is a consequence of the mass dependence in the particle sources due to neutral penetration. While the direct impact of the sources is small, it gets significantly enhanced by the $\gamma_{E\times B}$ part of the model. When modifying the transport to be reduced for higher ion mass—i.e. $\mu < 0$—the density and pressure dependence with ion mass can be inverted. With $\mu = -1$ the lower main ion mass is found with lower density and lower pressure. This is shown in figures 23(c) and 24. Note, we do not consider a gyroBohm like mass dependence with $\mu > 0$ as it would enhance the discrepancy with the experiment.

In the ELM cycle modelling varying μ will have only little impact on n and T instead it will change the ELM frequency as shown in figure 25. Reducing the transport will result in higher $f_{\rm ELM}$. However, the pedestal pressure will not change since this it is set by the ELM crash and $\alpha_{\rm crit}$ is kept constant. Additionally, n/T will remain fairly constant and $n^{\rm H} > n^{\rm T}$ despite the mass dependence in the transport. n/T is also not affected by a variation of $\alpha_{\rm crit}$ as described in appendix B.

The ELM frequency as an additional output of the model helps us to assess which of the two configurations is more realistic. As discussed in detail in appendix B the power dependence known for the frequency of type-I ELMs can only be reproduced when the pedestal is not quasi-stationary. This is a strong argument in favour of the stability limited model.

Assuming the stability limited model provides the more accurate description, we varied the model parameters to match the experimental pedestal characteristics presented in section 3. To achieve this match, i.e. $n^{\rm H} < n^{\rm T}$ while $T^{\rm H} \sim T^{\rm T}$, we need to vary $\alpha_{\rm crit}$ and neutral source n_0 with the main ion isotope mass. The result is illustrated in the form of time traces of ELM cycles in figure 26 and as edge profiles in figure 27. $\alpha_{\rm crit}$ and n_0 both increase with isotope mass. Heat and particle transport do not need to be mass dependent

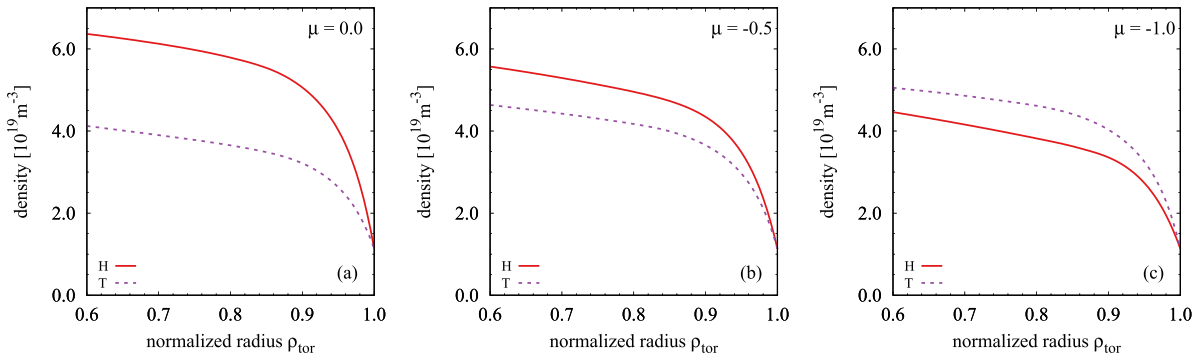

Figure 23. Expected influence of a mass dependence in edge heat and particle transport with $\chi \propto A^{\mu}$ on the pedestal density in the transport limited case.

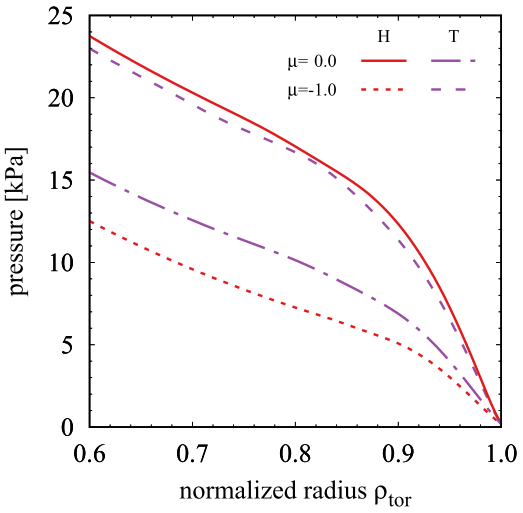

Figure 24. Expected influence of a mass dependence in edge heat and particle transport with $\chi \propto A^{\mu}$ on the pedestal pressure in the transport limited case.

to achieve this, i.e. $\mu = 0$. To deduce an exact value for μ from our experiments, we would require an accurate ELM stability model which includes proper treatment of the isotope mass. Unfortunately, such a model is not yet available. However, the model illustrates the general trend expected for f_{ELM}. For our example case with $\mu = 0$ we find $f^{H}_{\mathrm{ELM}}/f^{T}_{\mathrm{ELM}} = 2$ and with increasing mass dependence ($\mu < 0$) this ratio reduces. With $\mu = -0.5$ the ELM frequencies are the same for H and T. For $\mu < -0.5 \rightarrow f^{H}_{\mathrm{ELM}} < f^{T}_{\mathrm{ELM}}$. For $\mu \leqslant -0.75$ the transport in the H case increased so much that α falls below α_{crit} which corresponds to an L-mode like pedestal. A gyroBohm like mass dependence $\mu = 0.5$ has not been considered, because $f^{H}_{\mathrm{ELM}}/f^{T}_{\mathrm{ELM}}$ would increase considerably to values not observed in experiment. The parameter which is not varied here is the separatrix density which would have an additional impact if it is significantly different for H and T. However, a change of n_{sep} would not significantly affect n/T in the pedestal since heat and particle transport are coupled in our model.

To summarise: when an ELM stability limited pedestal is modelled with coupled heat and particle transport a mass dependence in the transport will not impact the profiles, only the ELM frequency. When varying the pedestal pressure via the ELM stability, n/T will remain constant. To change n/T one needs to introduce a mass dependence in the sources, or the heat and particle transport require different mass dependencies.

4.2. Pedestal stability

For the PB ELM stability analysis we use the ELITE [58] code. Due to the lack of highly resolved ion temperatures in the pedestal $T_{\mathrm{i}} = T_{\mathrm{e}}$ is assumed. While this is the best assumption possible and at the pedestal top $T_{\mathrm{i}} \sim T_{\mathrm{e}}$ is fulfilled, it could introduce systematic uncertainties if ∇T_{i} is significantly different from ∇T_{e}, which has been observed before in AUG [59] or DIII-D [55]. However, tests performed with $T_{\mathrm{i}} \neq T_{\mathrm{e}}$ showed a negligible impact on the results compared to the $T_{\mathrm{i}} = T_{\mathrm{e}}$ assumption [60]. The ideal PB growth rates scale with the main ion mass but are normalised to the Alfven frequency ω_{A}. Therefore, when using a criticality condition of $\omega_{\mathrm{A}} > 0.03$ to determine the stability, the mass dependence should cancel out. This was investigated in detail for H and D [17], with the result that only a very small mass dependence is expected from the ideal PB theory. However, this mass dependence was far from sufficient to explain the observations. A similar picture is found in our data set. In figure 28, for each isotope mass, both low and high δ cases are compared to the PB analysis based on the experimental profiles. The small variation of the stability boundary with triangularity is an indication that the pedestals discussed here are at the ballooning boundary, because, the impact on the PB boundary is expected to be stronger. The stability boundaries are consistently around $\alpha_{\mathrm{crit}} \sim 3$ regardless of the isotope mass. The D plasmas are found exceptionally close to the predicted boundary. The low δ H pedestal is found more in the stable region while both low and high δ T pedestals are found to be unstable. To illustrate the general quality of the PB predictions we quantify the quality with $\alpha_{\mathrm{exp}}/\alpha_{\mathrm{crit}}$ as described in [61]. The result is shown in figure 29 where a spread of $\alpha_{\mathrm{exp}}/\alpha_{\mathrm{crit}}$ by over a factor of 3 is observed. Additionally, there is no clear separation by isotope masses. This indicates that the isotope mass is unlikely to be the only reason for these differences. However, the weighting is still towards higher masses tending to be expected unstable, while the pedestal with lower masses should be more stable.

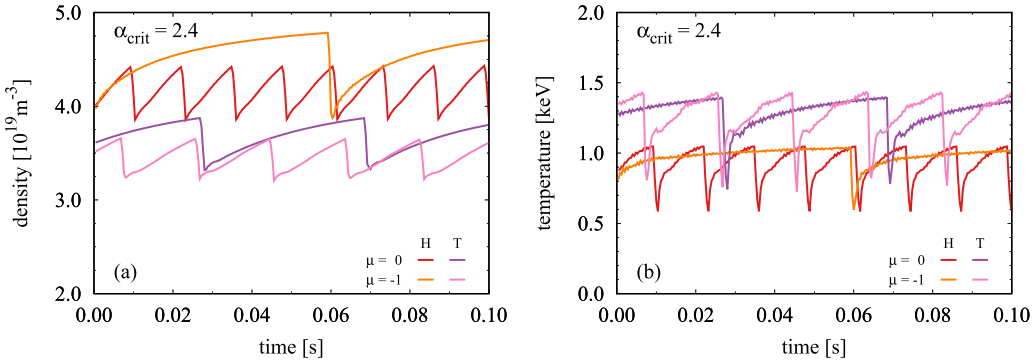

Figure 25. Evolution of density (*a*) and temperature (*b*) during an ELM cycle at $\rho_{tor} = 0.92$ for the same α_{crit} but different mass dependence in the edge transport model for H and T.

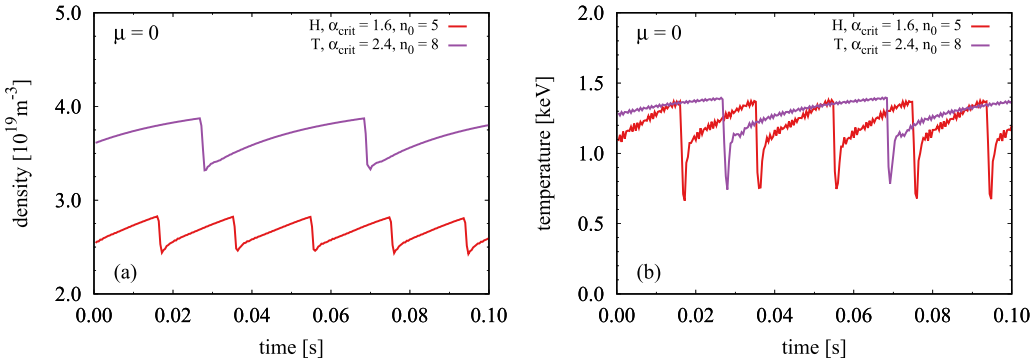

Figure 26. Evolution of density (*a*) and temperature (*b*) during an ELM cycle at $\rho_{tor} = 0.92$ for H and T with different α_{crit} and n_0, but without any mass dependence in the transport.

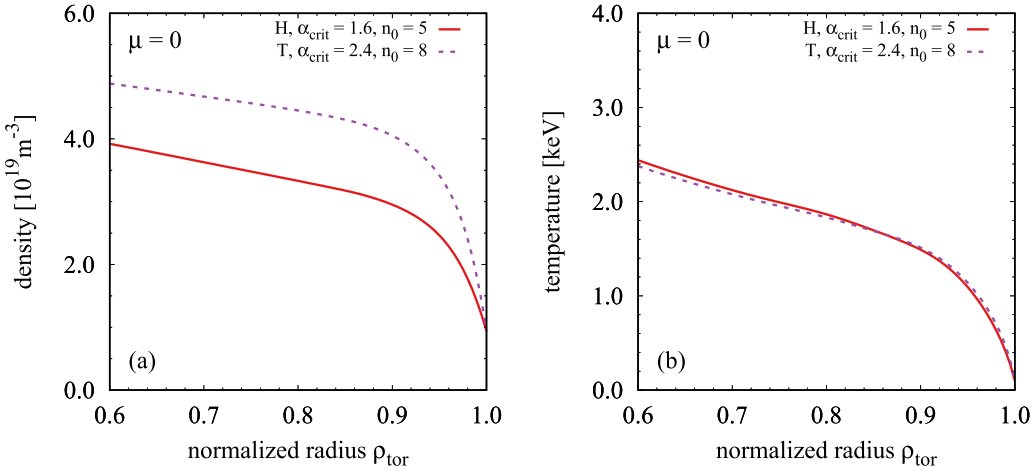

Figure 27. Edge profiles of density (*a*) and temperature (*b*) before an ELM crash for H and T with different α_{crit} and n_0, but without any mass dependence in the transport.

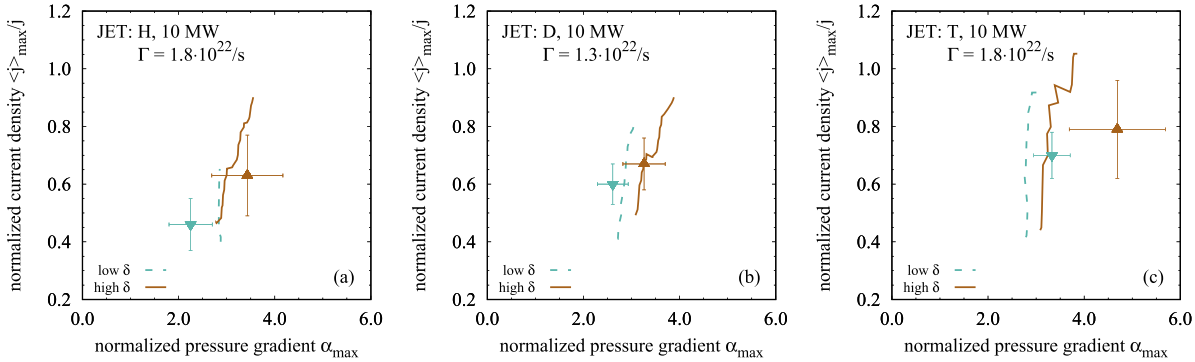

Figure 28. Ideal peeling-ballooning stability diagrams for H (*a*) (JPN97094), D (*b*) (JPN97035) and (*T*) (*c*) (JPN100177) plasmas at high and low triangularity.

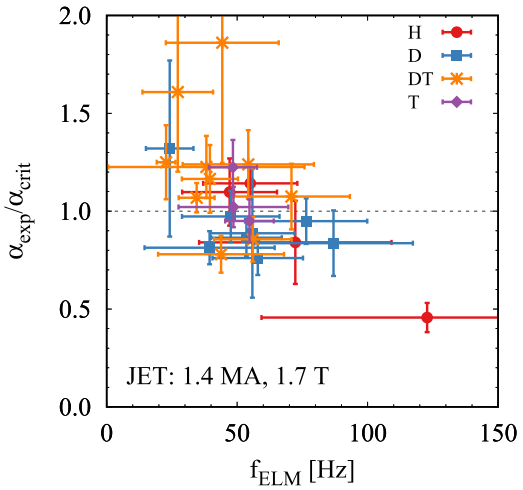

Figure 29. Deviation of experimental pressure gradients α_{exp} from peeling-ballooning stability boundary α_{crit} as a function of the ELM frequency.

5. Discussion of pedestal properties

The experimental observations for the type-I ELMy H-modes discussed in section 3 are summarised as follows:

- Engineering match between H, D and T; we find with increasing A: higher n_{ped}, higher p_{ped}, constant T_{ped}, higher n_{ped}/T_{ped}, smaller Δn, constant ΔT, higher ∇n, higher ∇p, constant ∇T, lower f_{ELM}.
- Gas fuelling Γ scan at low δ; we find with increasing A: stronger n_{ped} response to Γ, less p_{ped} degradation with Γ; smaller differences due to A at low Γ compared to high Γ.
- Gas fuelling Γ scan at high δ; we find with increasing A: similar n_{ped} response to Γ, similarly low p_{ped} degradation with Γ.
- Density match between H and T with different Γ and δ; we find with increasing A: reduced Doppler signal of normal incidence reflection in the steep gradient region.
- Whole database; we find a strong correlation of $\tau_{th,ped}$ with f_{ELM} independently of A.

From this list, we want to highlight that the pedestal dependencies on the main ion mass number change with the plasma shape and with gas fuelling. Additionally, the pedestal confinement time as a function of f_{ELM} does not show a mass dependence. These observations strongly suggest that a scaling derived from this data set will not yield any results suited for extrapolation. This is why a more sophisticated analysis is required to draw conclusions from these observations.

A major difficulty in describing the pedestal physics stems from the highly dynamical nature of this plasma region in the presence of ELMs. In such a situation the pedestal is not necessarily in transport equilibrium. However, for the lack of a complete model, it is often assumed that before an ELM crash, the plasma will be quasi-stationary which then allows us to determine transport coefficients that can be compared under different conditions. Unfortunately, in H-mode ELMs exist which impose limits to the pedestal profiles which are intrinsically independent of the transport properties.

To be able to assess the importance of these different aspects we introduced a new dynamic ELM cycle model in section 4.1 and appendix B. The model uses an externally imposed ELM stability limit and simulates the ELM recovery based on a critical gradient transport suppressed by $\gamma_{E\times B}$ shearing. It has an intrinsic isotope mass dependence due to neutral penetration. The model has no predictive capability but includes enough physics to help understand the interactions that might govern the pedestal. The key new feature of the model is its dynamic nature which has the ELM frequency as output. This is particularly important because for a transport analysis using static profiles, we need to measure T and n as well as heat and particle source profiles to infer transport coefficients. However, the particle source is difficult to measure and generally not available which is why it remains a free parameter in the modelling. So in general a static transport analysis will be an under-determined problem. The inclusion of the ELM dynamics in our model reduces the degrees of freedom in the model because f_{ELM} is a well defined quantity in the experiment. A self consistent model based on $\gamma_{E\times B}$ can enhance small profile effects due to a positive feedback loop. The n_i and T_i profile gradients directly influence $\gamma_{E\times B}$ via $E_r \propto T_i\,(L_n^{-1} + L_{T_i}^{-1})$ and $\gamma_{E\times B}$ acts back on n and T via the transport reduction. This behaviour is nicely observed in the nonlinear profile recovery after an ELM (e.g. figure 25), which is also observed experimentally for H and T (figure 21) and ELM studies in general [62–64].

In the model, we vary the critical pressure gradient α_{crit} which triggers an ELM crash, the fuelling efficiency n_0/n_{sep} and an additional mass dependent transport enhancement μ with $\chi \propto A^{\mu}$ ($D \propto \chi_i$). The main experimental quantities for comparison are α_{crit} or p_{ped}, n/T and f_{ELM}.

We have shown that the hypothetical maximum pressure gradient that can be achieved in transport equilibrium α_{eq}—if ELMs were switched off—is strongly linked to f_{ELM} with $\alpha_{eq}/\alpha_{crit} \propto f_{ELM}$ for $\alpha_{eq} > \alpha_{crit}$ (figure 58). So in this model, the pedestal is limited by the ELM instability and never quasi-stationary. This would mean a power balance analysis of an ELMy H-mode at pre-ELM pedestal conditions will never yield the real transport coefficients. Only for a reasonably low f_{ELM} the resulting transport coefficients would come close to the actual values. More importantly, a comparison of transport coefficients obtained at different f_{ELM} assuming quasi-stationarity is essentially meaningless. This would strongly affect the interpretation of observations with different isotopes as f_{ELM} changes significantly with mass.

The dynamic edge modelling highlighted the importance of the ELM stability parameter α_{crit} and the experiment shows a mass dependence of α_{crit}. The ideal PB modelling discussed in section 4.2 does not support such a mass dependence (figure 28) and fails to capture the experimental observations (figure 29), these observations are consistent with earlier studies for H and D plasmas [7, 17, 18]. However, stability modelling taking the resistivity into account does yield a mass dependence in α_{crit} [60, 65]. Such a resistivity-based model

could be the basis for explaining the enhanced impact of the main ion mass at high gas fuelling rates.

Another observation is that n/T changes with the main ion mass. ELM stability is not expected to impact n and T differently, therefore, we need at least one of the following: a mass dependence in D/χ or in n_0. Our transport model provides evidence to help answer this question. When changing the transport to achieve $n^{\mathrm{T}} > n^{\mathrm{H}}$ (figure 23(*c*)) we find $\Delta_{n\mathrm{T}} = 0.064$ and $\Delta_{n\mathrm{H}} = 0.056$ in ρ_{tor} as determined with same bi-linear fit used for the experimental pedestal widths. When changing the fuelling efficiency to increase the density the pedestal narrows (figure 54(*b*)) with $\Delta_{n0=5} = 0.068$ and $\Delta_{n0=8} = 0.058$. This narrowing of the pedestal with higher density is a typical feature for a neutral penetration based pedestal width model [66], however, most reported data sets do not follow this trend [67–71]. Different from these existing data sets, the mass scan at high δ shows a clear narrowing of the density width (figures 16 and 17) suggesting that the particle source might have changed with isotope mass. Note in our model we identified the fuelling efficiency n_0/n_{sep} as the important quantity for the particle source. The inclusion of n_{sep} is important because a higher n_{sep} tends to reduce $\gamma_{E\times B}$ and therefore, increases transport (figure 55). So the impact of increasing n_0 is not easily tested experimentally, because when puffing more gas n_{sep} is typically changed as well. The recycling particle flux could provide a potential explanation, if this increases with isotope mass it would alter the effective particle sources in the pedestal. While the reflectivity of hydrogen isotopes on tungsten surfaces indeed increases with mass [72], this effect is relatively small and detailed neutral modelling is required to assess its relevance. Nevertheless, the impact on the density profile is more pronounced at higher triangularity where the wall clearance is reduced in the upper divertor. Correlated with this change in wall clearance we observe a reduction of the particle flows towards the inner divertor. This could have an effect on the recycling fluxes back to the main plasma. Recent SOLPS-ITER simulations for D-T plasmas suggest that higher mass might be favourable in the distribution of neutrals in the divertor [73]. This is attributed to changing effective diffusion of neutrals with different masses when the diffusion is dominated by charge-exchange processes.

This leaves the big question: what value has the mass enhancement μ in the pedestal transport? The short answer is that it should not matter for the confinement of type-I ELMy H-modes. When μ does change it has only a minor impact on the achievable pedestal pressure (figure 25). The different transport properties result in a varying f_{ELM}. The correlation of $\tau_{\mathrm{th,ped}}$ and f_{ELM} which is observed experimentally (figure 11) is likely a consequence of this. The farther apart α_{crit} and α_{eq} are the larger f_{ELM} becomes. Since there is not a large variation in heating power and gas fuelling (<50%) one could assume α_{eq} to be relatively constant over the data set. Now a reduction of pedestal confinement is correlated with a reduction of α_{crit} [55] which in our model results in higher f_{ELM} as observed also experimentally.

There are still open questions on how the balance between electrons and ions and density and temperature might affect α_{crit}. This can only be answered in a dynamic model which is coupled to an ELM stability code that ideally takes resistive physics into account. Such a model would also allow us to derive the value for μ from a comparison with the experimental f_{ELM}.

Although, the value of μ is expected to be relatively unimportant for the pedestal pressure in type-I ELMy H-modes, this certainly does not mean that $\mu = 0$. The reflectometer measurements showed a significant increase of the spectral power for H compared to T (figure 22) which potentially corresponds to an increased density fluctuation level in the pedestal for lower main ion mass. Nonlinear GENE simulations find that in the heat transport channel, the mass dependencies of turbulent ITG and neoclassical transport cancel each other, while in the particle transport, the ITG mass dependence remains dominant [37] which yields a mass dependence in D/χ that could explain the mass dependence of n/T. Further observations in favour of an isotope mass dependence in the transport properties at the edge are related to L-mode [35] and L-H transitions [74–77] where the observed mass dependence cannot be explained with ELM stability.

6. Core characteristics

The impact of gas puffing and shaping on the pedestal was discussed in section 3 to better understand the physics mechanisms setting the pedestal. Now we will utilise those pedestal parameter scans to improve our understanding of the core plasma, in particular, the mass dependence of heat and particle transport.

Medium β_{N} overview ($\beta_{\mathrm{N}} < 2.5$): the majority of the data was collected at 10 MW of heating power and the gas scan at low δ shown in figure 30(*a*) highlights the strong correlation between the observed core and pedestal stored energies. A major drawback of this subset of data is that it is separated by isotope mass and due to the edge–core correlation is not sufficient for an experimental separation of mass and pedestal impact. With the additional data at high δ this correlation is broken and as shown in figure 30(*b*) we find matched pedestal pressures for different main ion masses. The DT plasmas are found with properties of the T rather than the D plasmas regarding the core and pedestal thermal energies.

Engineering match: the profiles for H, D and T plasmas from an engineering match are shown in figure 31. As expected from the overview plot the density increase for higher isotope mass propagates to the core, while the temperatures which are matched at the pedestal remain the same within their uncertainties and $T_{\mathrm{i}} = T_{\mathrm{e}}$ for most of the radius. The rotation of the D plasma with D-NBI is the same as the one of the T plasma with T-NBI. This is expected because the higher torque input from NBI injection with heavier neutrals is mostly compensated by the larger inertia of the plasma with the higher main ion mass. The rotation in H is higher because those plasmas were heated with D-NBI and therefore have a torque input that is higher relative to the plasma inertia compared to having the same

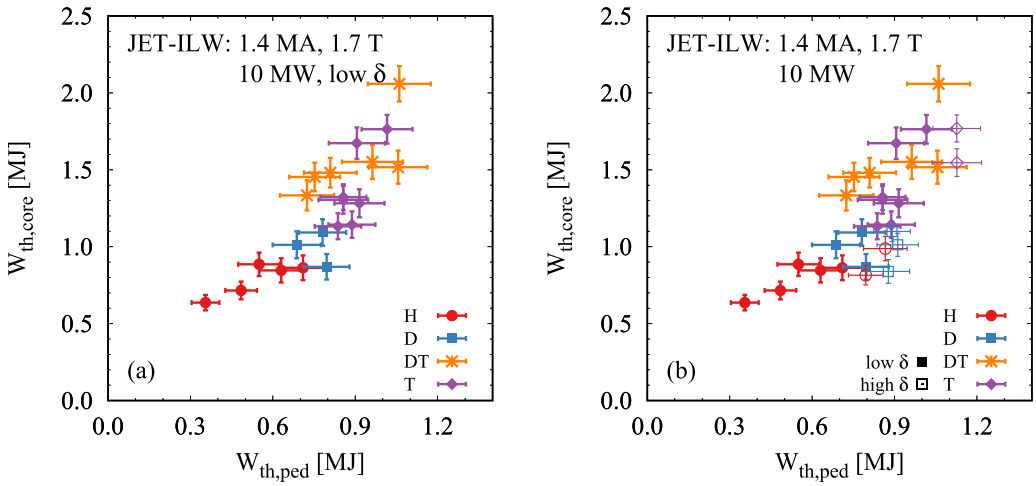

Figure 30. Core thermal stored energy as a function of the pedestal thermal stored energy for 10 MW plasmas of a gas puffing scan for different isotopes with low δ only in (*a*) and also high δ plasmas in (*b*).

species for NBI and main ions. Although, the density is higher in T while the temperature profiles are matched no systematic and significant isotope dependence is observed in the electron and ion heat diffusivities for most of the radius as shown in figure 32. Only the electron heat diffusivities show some differences with isotope mass close to the pedestal top, however, in this region the electron temperature profile becomes relatively flat and small variations in the gradients will translate in large uncertainties for χ_e. There is a significant difference between the electron and ion transport channels where $\chi_i \sim 2\chi_e$ for most of the radius. Note that close to the edge the χ_i values are as unreliable as the uncertainties suggest because no ion temperature gradients are available for the pedestal. Since $T_e \sim T_i$ more heat is transported via the ion channel in this comparison.

Pedestal match: a match of the boundary at the pedestal is achieved when comparing a low δ T plasma to high δ H plasmas with the same heating power but different gas fuelling. The higher gas puff in H does not cause a degradation of the pedestal due to the high δ shape as discussed in section 3. For The resulting profiles are shown in figure 33 which are extremely well matched for n_e, T_e and T_i for both isotopes with $T_i = T_e$, while the toroidal rotation is higher in H due to the D-NBI heating. Figure 34 shows again the electron and ion heat diffusivities this time for the pedestal match. We find $\chi_e^H \geqslant \chi_e^T$, but still similar within the uncertainties, while $\chi_i^H = \chi_i^T$ despite the uncertainties in ∇T_i. Again χ_i is about twice as high as χ_e.

High β_N ($\beta_N > 2.5$): extending the data set to higher pressure is not as straightforward as for 10 MW and medium β_N as discussed in appendix A, therefore, we have fewer comparison plasmas. This includes one T pulse (JPN99224) with $\beta_N = 3.0$ which is compared to a D pulse (JPN97512) with matched density and $\beta_N = 2.8$ and a D pulse (JPN96830) at lower density but matched total thermal pedestal pressure and $\beta_N = 2.5$. All pulses have the same NBI heating power of 13 MW with similar power density profiles but higher radiated power in T as discussed in section 2. The resulting profiles are shown in figure 35 for the pedestal density match and in figure 36 for the pedestal pressure match. The overview of the pedestal parameters was shown in figure 10. At high β_N we find $T_i > T_e$ for both isotope masses. The core temperature profiles for D and T have similar absolute values at mid-radius even for different densities, however, the T pulse has lower pedestal temperatures and features steeper gradients in particular for T_i and reaches higher core T_i than the D pulses. Comparing the D pulses with each other shows that the higher density also results in a higher pressure since the temperature does not drop equivalent to the density increase. Since the radiation is different for these pulses we also investigate the heat diffusivities. For the density match χ_e and χ_i are shown in figure 37 for D and T which are both the same over the whole radius within their uncertainties for the different isotope masses. Additionally $\chi_e \sim \chi_i$ in the core. For the pedestal pressure match shown in figure 38 the situation is similar for χ_e (*a*) which is matched between D and T, however, it is different for the ions (*b*) where the D pulse with lower n_e has a much higher χ_i than the T plasma. χ_i is most different at the outer radii of $\rho_{tor} = 0.4 \ldots 0.8$.

Entire database: for the entire database, the core stored energy is not a good metric because of the different heating powers which naturally give different $W_{th,core}$. Therefore, we are using the core energy confinement time $\tau_{th,core} = W_{th,core}/P_{sep}$. In figure 39 the dependence of $\tau_{th,core}$ on the boundary condition $W_{th,ped}$ is illustrated. For H and D plasmas there is a clear linear correlation of $\tau_{th,core}$ and $W_{th,ped}$ and a decent overlap for pedestal energies between 0.6 and 1.0 MJ. H plasmas extend to lower pedestal energies and D to higher energies. The DT and T plasmas show a steeper slope of their $\tau_{th,core}$, $W_{th,ped}$ correlation, resulting in higher core confinement times for the same pedestal energies. Still at intermediate $W_{th,ped} \sim 0.8$ MJ the data from all isotopes overlaps which corresponds to the profiles for the pedestal match shown above.

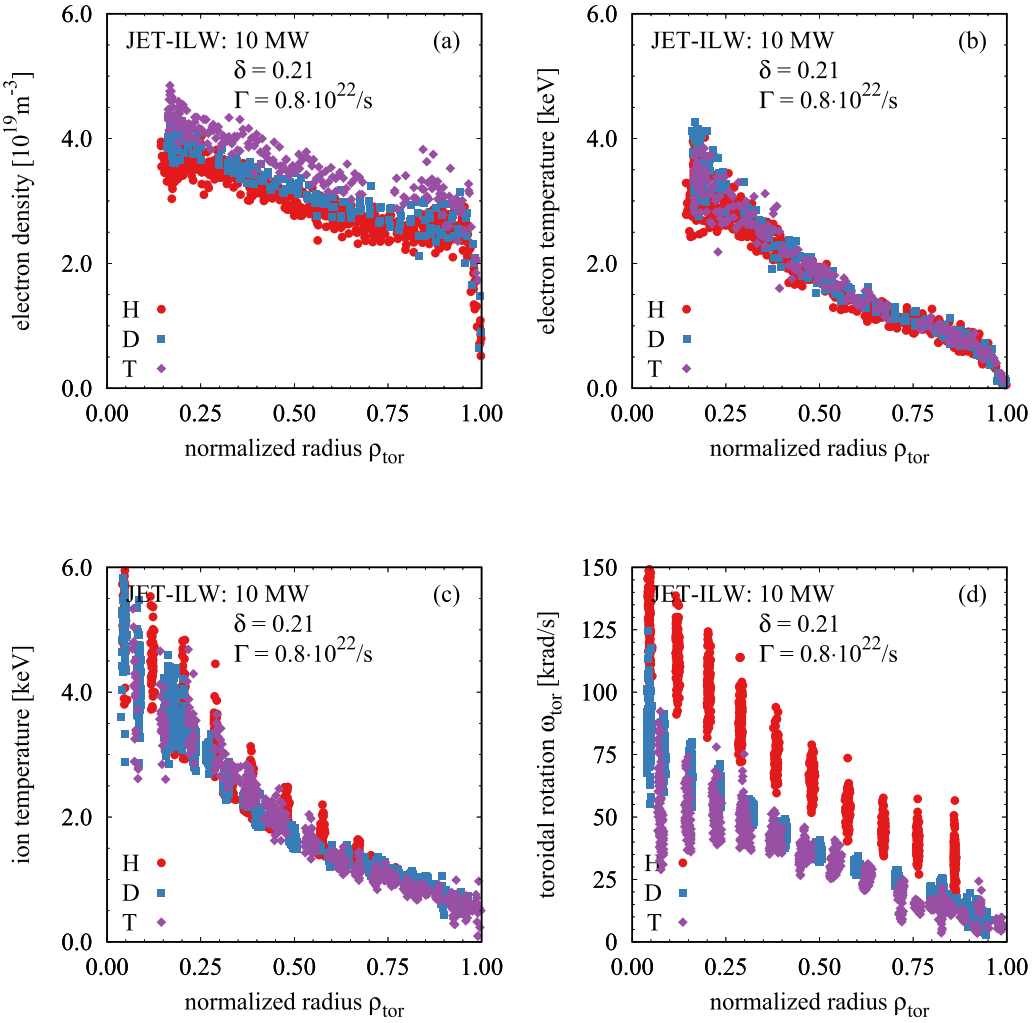

Figure 31. Profiles of electron density (*a*), electron temperature (*b*), ion temperature (*c*) and toroidal angular frequency (*d*) for an engineering match at 10 MW, low δ and low gas puffing but different main ion masses. H: JPN97095, D: JPN97036, T: JPN98795.

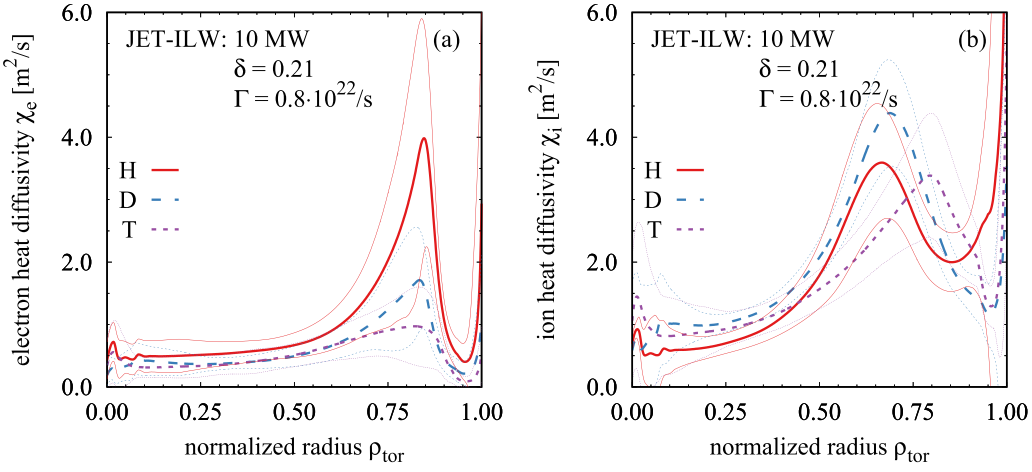

Figure 32. Profiles of electron heat diffusivity (*a*) and ion heat diffusivity (*b*) for an engineering match at 10 MW, low δ and low gas puffing but different main ion masses. The thin lines represent the uncertainties. H: JPN97095, D: JPN97036, T: JPN98795.

As discussed in section 1, for the density peaking the mass dependent electron–ion collisionality $\nu_{\rm eff}$ should be more important than the mass independent ion–ion collisionality ν_{i*}. Our data set allows for the first time to test this with a variation of 3 in A. The density peaking, as the ratio of the density at $\rho_{\rm tor} = 0.30$ and $\rho_{\rm tor} = 0.85$, is illustrated

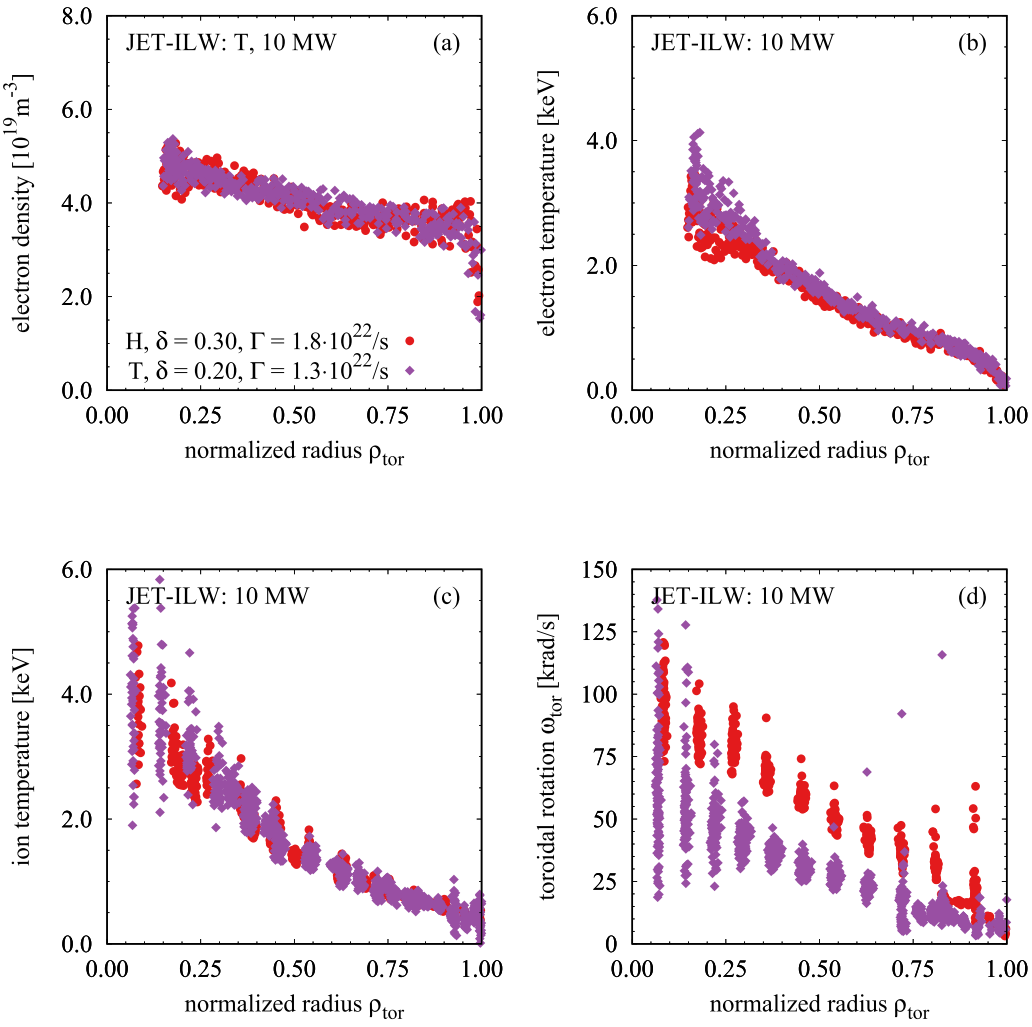

Figure 33. Profiles of electron density (*a*), electron temperature (*b*), ion temperature (*c*) and toroidal angular frequency (*d*) for an pedestal match at 10 MW achieved with different δ and gas puff for main ion masses H (JPN97094) and T (JPN98794).

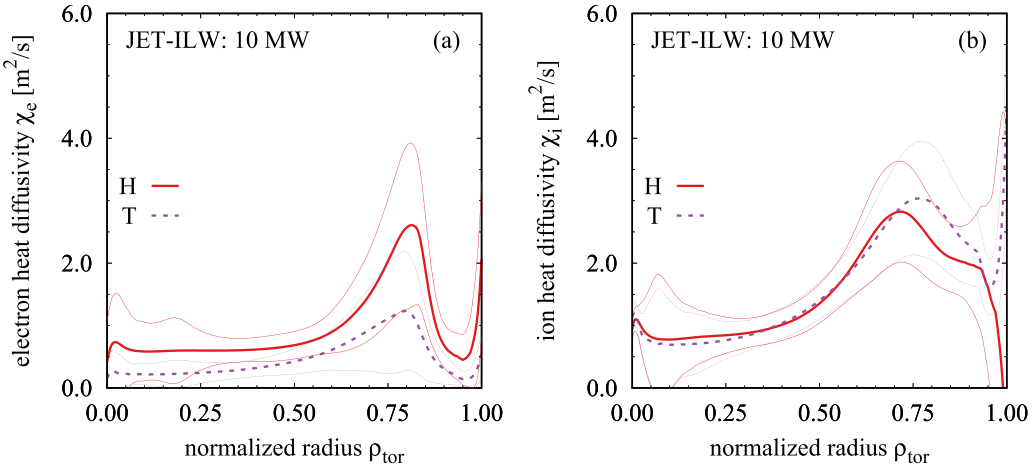

Figure 34. Profiles of electron heat diffusivity (*a*) and ion heat diffusivity (*b*) for an pedestal match at 10 MW achieved with different δ and gas puff for main ion masses H (JPN97094) and T (JPN98794). The thin lines represent the uncertainties.

in figure 40 as a function of $\nu_{i\star}$ (*a*) and $\nu_{\rm eff}$ (*b*), where the collision frequencies are calculated using $Z_{\rm eff} = 1$ and for DT mixed plasmas the effective ion mass is used for $m_{\rm i}$. There is a clear trend of the density peaking with the collisionality in both plots. However, the mass dependent $\nu_{\rm eff}$ orders the data better, highlighting the importance of the electron–ion collisions to the turbulent particle pinch.

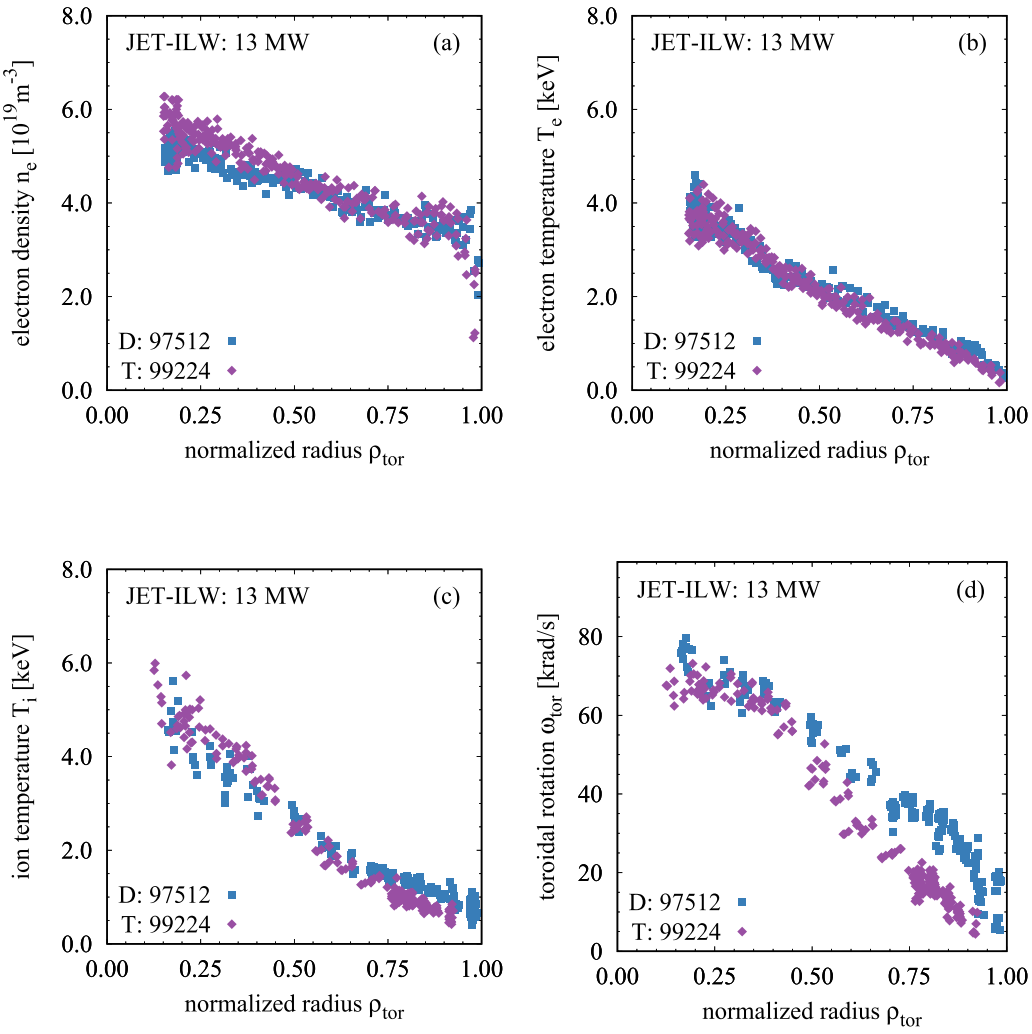

Figure 35. Profiles of electron density (*a*), electron temperature (*b*), ion temperature (*c*) and toroidal angular frequency (*d*) for high β_N pulses at matched density in D (JPN97512) and T (JPN99224).

The impact of collisionality is observed up to the edge, where the measured density gradient length R/L_n reduces with increasing collisionality as shown in figure 41. Due to the combination of higher ion mass and their higher pedestal densities the T plasmas are mostly found at higher collisionality and therefore, with lower R/L_n than the bulk of the H and D plasmas.

7. Core modelling

We will first discuss known physics principles that can lead to differences in core confinement properties based on changes in isotope mass and/or pedestal properties. This will be essential to understand the trends we find when applying quasilinear predictive modelling to the whole data set. The predictive modelling shows certain deviations from the experimental trends. To understand the physics cause for these deviation we require local linear and non-linear gyro-kinetic simulation. We started this effort with the GENE code [78]. Unfortunately, the investigation with non-linear GENE simulations in the local approximation where inconclusive. The simulations suggest a strong impact of the EM stabilisation on the turbulent heat fluxes. However, the predicted absolute heat fluxes are so far from the experimental values that their relevance remains questionable. This is why they are not included here. An extensive sensitivity study to scan the experimental inputs within their uncertainties is required to improve the significance of the results. Such a study will have to be presented in a future publication.

7.1. Core–edge coupling

In an H-mode plasma, it is often assumed that transport regions core and edge can be treated independently. This is not too bad of an assumption when both core and edge parameters are not varied a lot. However, for the data set discussed here, this is certainly not the case as the pedestal pressure is varied by a factor of 4 and the total pressure by a factor of 3. A known route how the global pressure can influence the edge is via β stabilisation of PB modes [79], this is taken into account in the stability analysis presented in section 4.2. The edge pedestal itself will again influence the core plasma and the

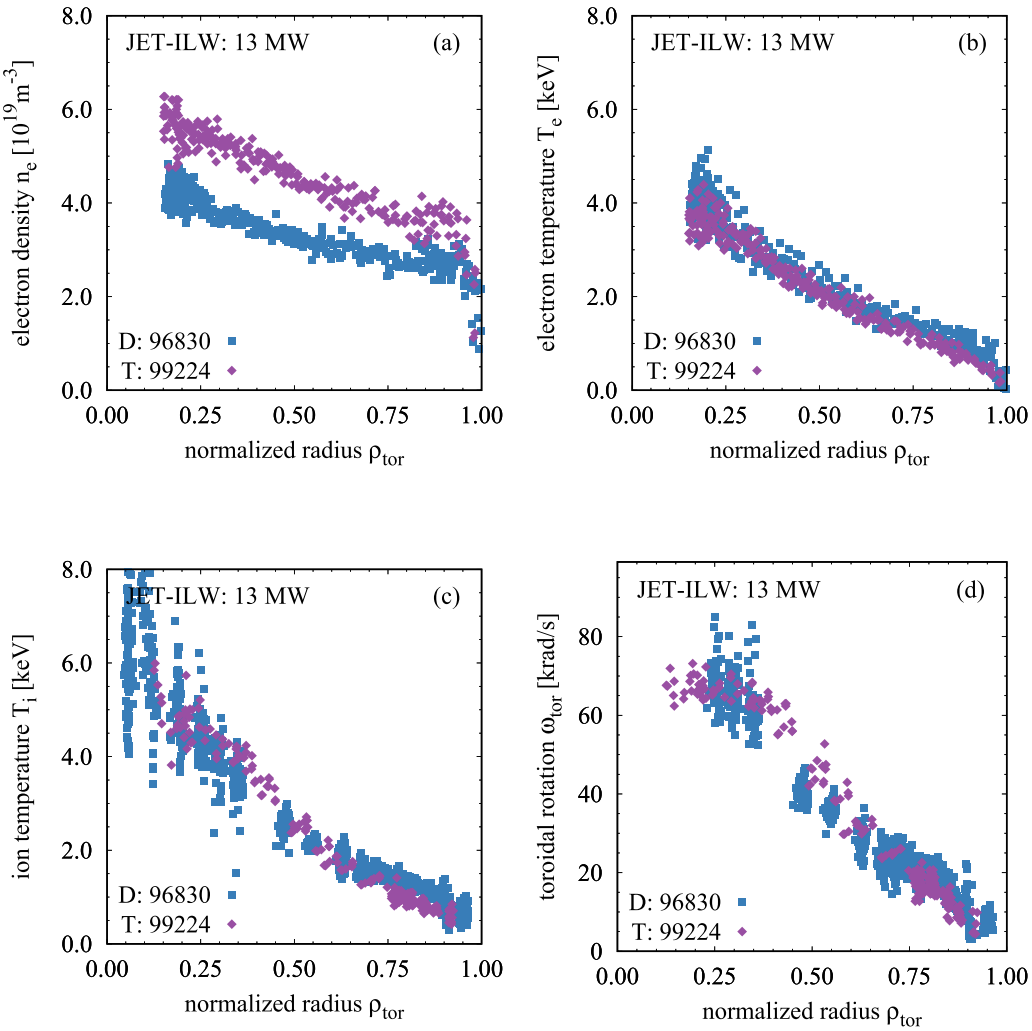

Figure 36. Profiles of electron density (*a*), electron temperature (*b*), ion temperature (*c*) and toroidal angular frequency (*d*) for high β_N pulses at matched thermal pedestal pressure in D (JPN96830) and T (JPN99224).

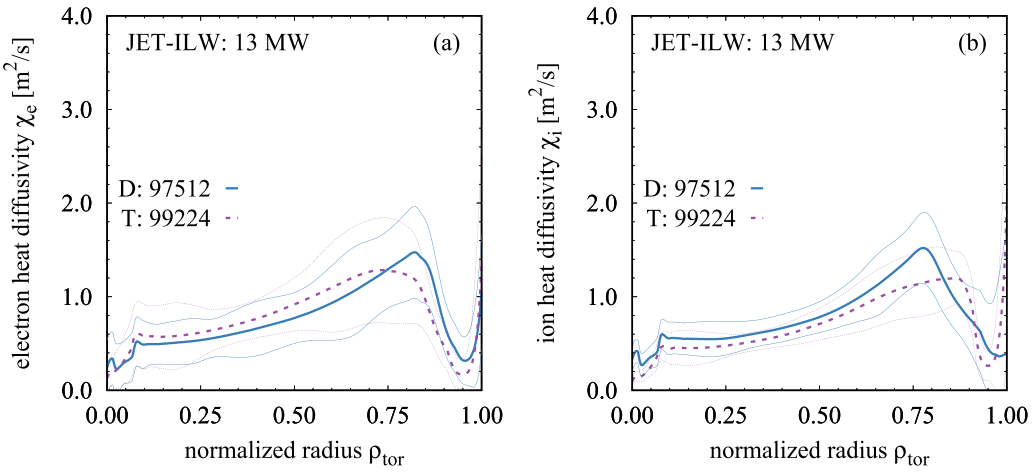

Figure 37. Profiles of electron heat diffusivity (*a*) and ion heat diffusivity (*b*) for high β_N pulses at matched density in D (JPN97512) and T (JPN99224). The thin lines represent the uncertainties.

resulting non-linear interaction can create complex feedback loops which were e.g. discussed in [9] and are one of the main motivations for integrated modelling codes like IMEP which also treat the scrape-off-layer [80]. For the interpretation of the parameter dependencies in our data set it will be essential to understand the leading contribution that a variation of the edge

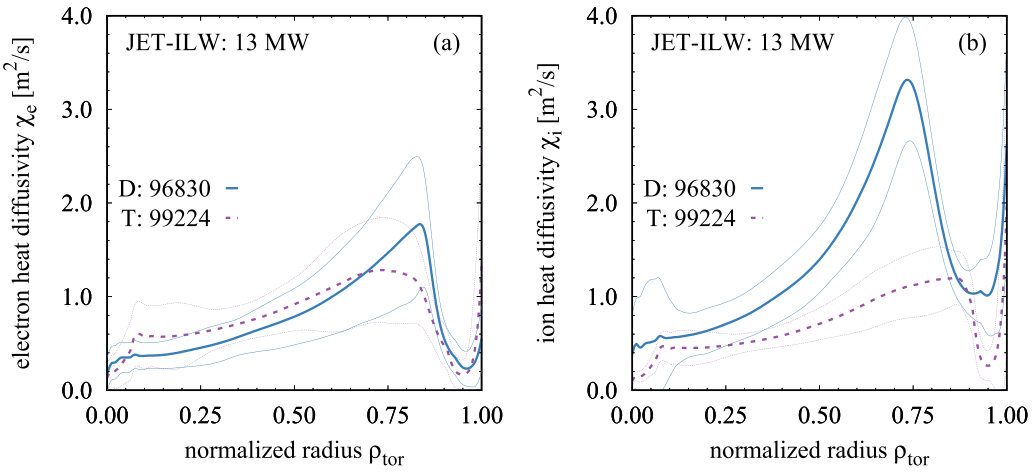

Figure 38. Profiles of electron heat diffusivity (*a*) and ion heat diffusivity (*b*) for high β_N pulses at matched thermal pedestal pressure in D (JPN96830) and T (JPN99224). The thin lines represent the uncertainties.

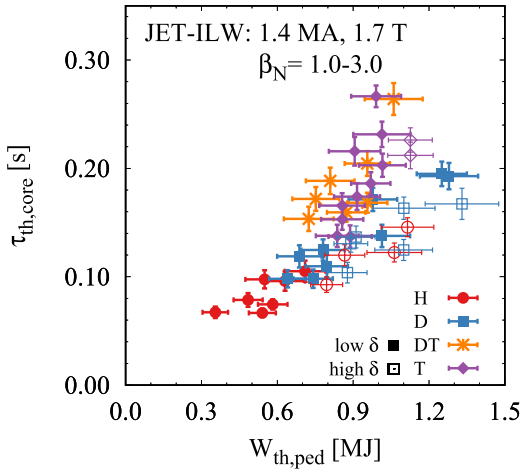

Figure 39. Core thermal confinement time as a function of the pedestal thermal stored energy for the entire 1.4 MA, 1.7 T database.

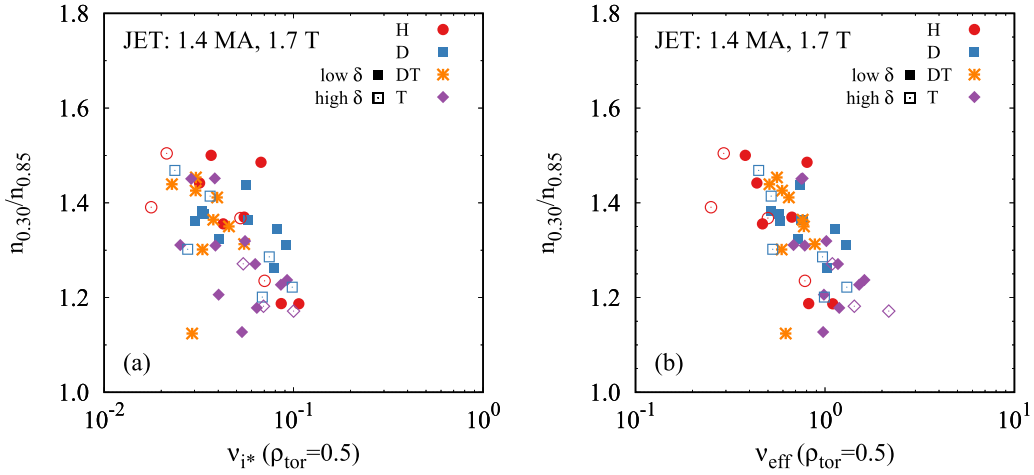

Figure 40. Density peaking as the ratio of the density at $\rho_{tor} = 0.30$ and $\rho_{tor} = 0.85$ plotted as a function of the mass independent ion–ion collisionality $\nu_{i\star}$ (*a*) and the mass dependent effective electron–ion collisionality ν_{eff}.

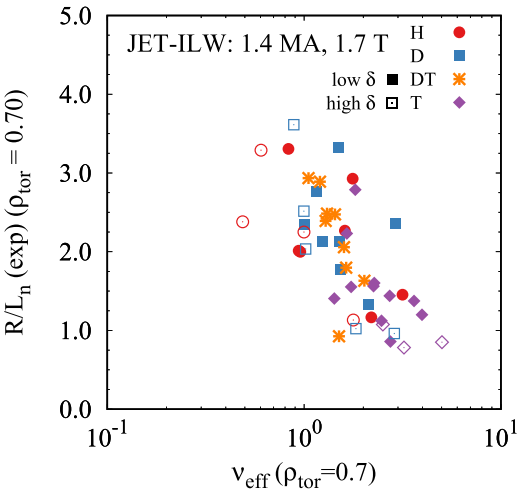

Figure 41. Normalised density gradient length at $\rho_{\mathrm{tor}} = 0.7$ plotted as a function of the mass dependent effective electron–ion collisionality ν_{eff}.

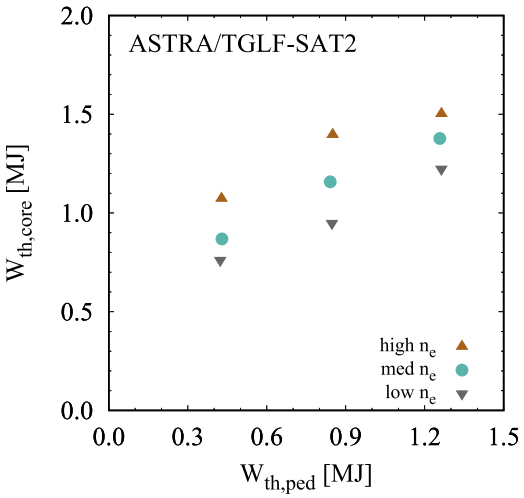

Figure 42. Impact of boundary condition on core stored energy $W_{\mathrm{th,core}}$ in ASTRA/TGLF-SAT2 simulations when varying n_{ped} and T_{ped}.

parameters will have on the core plasma. An important contribution stems from the temperature scale length invariance or profile stiffness [81]. In the limit of infinite stiffness we have $-\nabla T/T = L_{\mathrm{T}}^{-1} = \mathrm{const}$ which directly gives $T_{\mathrm{core}} \propto T_{\mathrm{ped}}$.

Another contribution is due to the temperature dependency in the efficiency of turbulent transport. This is generally associated with a gyroBohm or Bohm scaling of turbulent transport. Depending on plasma regime and species the turbulence scaling is often observed to be different [82]. However, all scalings exhibit a strong positive temperature dependence. This means for a higher temperature a larger absolute amount of heat can be transported with the same turbulent drive. Typically, the heat flux q is then normalised to the turbulence efficiency, in most cases, the gyroBohm heat flux q_{gB} or gyroBohm factor. For a purely gyroBohm like turbulent transport, the normalised heat flux q/q_{gB} should be constant for a given turbulent drive $\nabla T/T$. For hotter plasmas, the normalised heat flux goes down and less turbulent drive is required to transport the heat out of the plasma. In this case, a higher pedestal temperature will result in a lower core contribution to the total pressure.

In a realistic plasma, the transport is neither infinitely stiff nor does it purely scale like gyroBohm, therefore, we utilise the transport model TGLF-SAT2 to quantify the edge–core coupling expected for these two contributions. For this purpose, we run source driven simulations of n_{e}, T_{e} and T_{i} within the transport code ASTRA and the boundary fixed at $\rho_{\mathrm{tor}} = 0.85$. This boundary condition is motivated by one of the T plasmas that will be discussed in the next sections. We vary the boundary condition while keeping the heat and particle sources constant. At three distinct pressure levels, we vary the collisionality by scaling temperature and density, which results in nine different cases which are illustrated in figure 42. The impact of the stiffness and the gyroBohm factor partly cancel each other therefore a variation of factor of 3 in the pedestal pressure only results in a 40%–60% increase in the core stored energy. At constant pressure, the impact of a lower temperature is more obvious as a variation of a factor of 2 also yields an increase of $W_{\mathrm{th,core}}$ by about 50%. The correlation of the turbulent drive with the temperature is illustrated in figure 43(*a*) and shown for full profiles in figure 43(*b*). A lower temperature requires a higher gradient length to transport the same amount of heat. Therefore, $W_{\mathrm{th,core}}/W_{\mathrm{th,ped}}$ increases with lower T and higher n even for constant pedestal pressure. The density gradient length has a negligible impact on the TGLF-SAT2 predictions in the range $R/L_{ne} \in [0.5 - 1.5]$ relevant here [42].

To illustrate the significance of the impact the pedestal parameters have on the core transport we compare this to the impact of the main ion mass. ASTRA/TGLF-SAT2 is run with $A = 1$ and $A = 3$ using the average parameters of the boundary scan. The resulting profiles are shown in figure 44. We find a stronger density peaking with lower mass which has been theoretically explained by a stronger turbulent particle pinch for the lighter isotope [34]. The temperatures are fairly similar with the only differences being due to the mass dependence in the electron–ion equipartition. Since $T_{\mathrm{i}} > T_{\mathrm{e}}$ more heat will end up in the electron channel for lower mass, which is the reason for the reversal of ion and electron temperatures with ion mass. Overall increasing the mass by a factor of 3 results in a 19% reduction in the core stored energy which corresponds to a mass scaling suggested by TGLF-SAT2 of $W_{\mathrm{th,core}} \propto A^{-0.156}$. As will be discussed later, TGLF-SAT2 underestimates R/L_n close to the boundary in the T case. Therefore, the mass dependence suggested here is likely too large and should be considered as the upper limit.

7.2. ASTRA/TGLF-SAT2

The core transport is simulated in flux-driven simulations in the ASTRA transport code [83, 84] utilizing the transport model TGLF-SAT2 [40] with six basis functions. We simulate n_{e}, T_{e} and T_{i} while ω_{tor} is fixed with its experimental profile. The

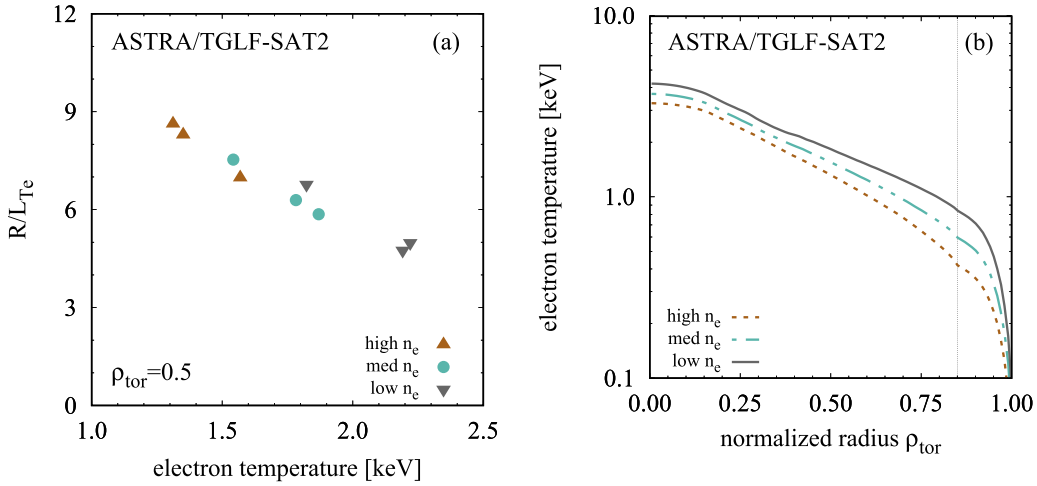

Figure 43. Impact of variations in T_{ped} on the normalised temperature gradient length R/L_{T} for the whole scan at mid radius (*a*) and radial profiles for the low pressure cases (*b*).

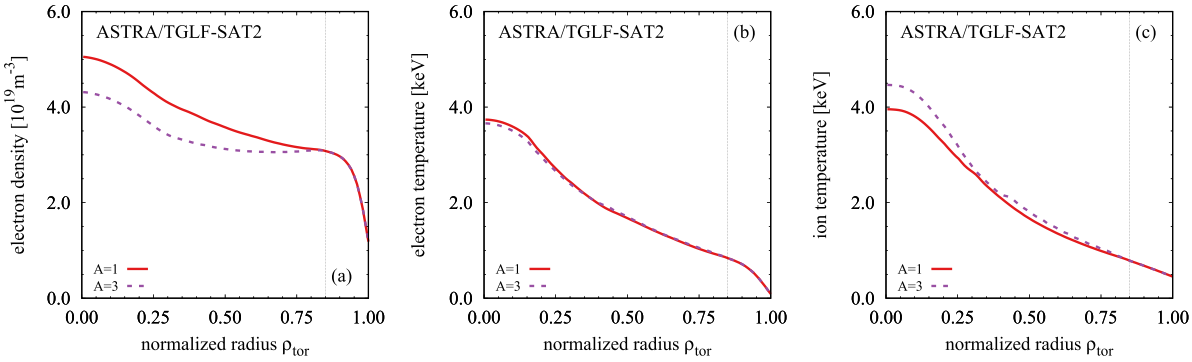

Figure 44. Electron density (*a*), electron temperature (*b*) and ion temperature (*c*) profiles calculated with ASTRA/TGLF-SAT2 for different main ion masses from a boundary at $\rho_{\mathrm{tor}} = 0.85$.

boundary condition for the simulated quantities is also taken from the experiment and fixed for $\rho_{\mathrm{tor}} > 0.85$. The auxiliary heat source profiles are taken from PENCIL [85] and PION [86] and cross checked against NUBEAM while the ohmic and equipartition powers are calculated by ASTRA. For the particle sources only the neutral beam fuelling is taken into account while gas puffing and recycling sources are assumed to be covered by the experimental boundary condition. The measured radiative power is distributed over the radius assuming a flat impurity density profile. This is not necessarily true, but we lack radially resolved impurity density measurements. Fast ions do not contribute to the drive of ITG turbulence [87] and are treated as non-resonant species which effectively reduces the thermal ion density. But no effects of turbulence mitigation due to fast ions are considered.

Pedestal match: for the pedestal match at medium β_{N} discussed in section 6 the TGLF-SAT2 predictions match the experimental core profiles extremely well. This is observed for H as shown in figure 45 as well as for T as shown in figure 46. The density peaking and $\chi_{\mathrm{i}} \sim 2\chi_{\mathrm{e}}$ as well as the difference in electron and ion temperature peaking observed for both isotope masses are reproduced by the model.

High β_{N}: for the plasmas at higher β_{N} the core profile prediction by TGLF-SAT2 is worse than at medium β_{N}, however, not completely off. Again the observations are fairly consistent for all main ion masses and also for all transport channels. TGLF-SAT2 predicts too high transport so the resulting density and temperatures are lower than experimentally observed. In the profile comparison shown in figure 47 for D and figure 48 for T it is evident that this difference already exists for $\rho_{\mathrm{tor}} > 0.5$. Interestingly, the TGLF-SAT2 heat diffusivities have $\chi_{\mathrm{i}} > \chi_{\mathrm{e}}$ as in the medium β_{N} cases while the high β_{N} experimental heat diffusivities were similar for the electron and ion channel with $\chi_{\mathrm{i}} \sim \chi_{\mathrm{e}}$.

Entire database: we ran predictive ASTRA/TGLF-SAT2 simulations for all time slices selected for analysis. To compare with the experiment we calculate $W_{\mathrm{th,core}}^{(\mathrm{TGLF})}$ and $\tau_{\mathrm{th,core}}^{(\mathrm{TGLF})}$ using the predicted pressure profiles and plot the latter against the experimental boundary condition. The result is shown in figure 49 and should be compared to its counterpart based on experimental core data shown in figure 39. From this comparison it becomes evident that TGLF-SAT2 can reproduce two key features observed experimentally, the correlation between the core confinement time and the pedestal pressure, as well as the separation of DT and T plasmas from their H and D

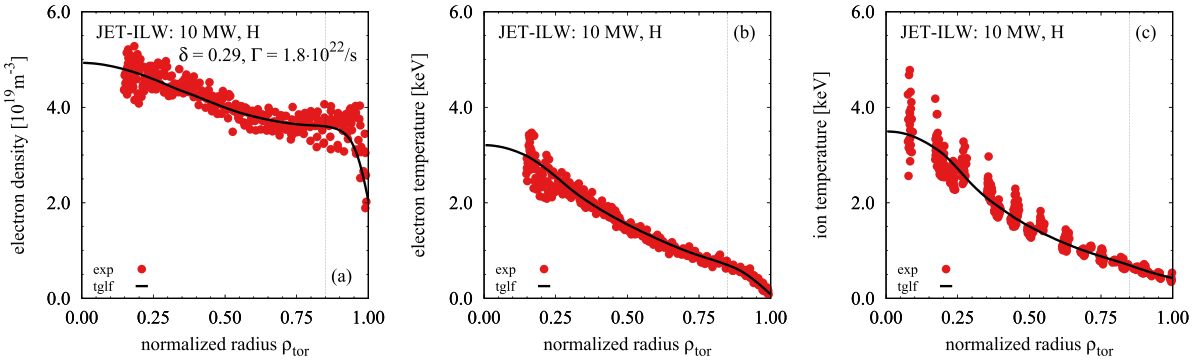

Figure 45. Profiles of electron density (*a*), electron temperature (*b*), ion temperature (*c*) for the H pulse (JPN97094) of the H, T pedestal match with the experimental data as points and the prediction by TGLF-SAT2 as solid line. The position of the boundary condition for the simulation is indicated by the vertical line.

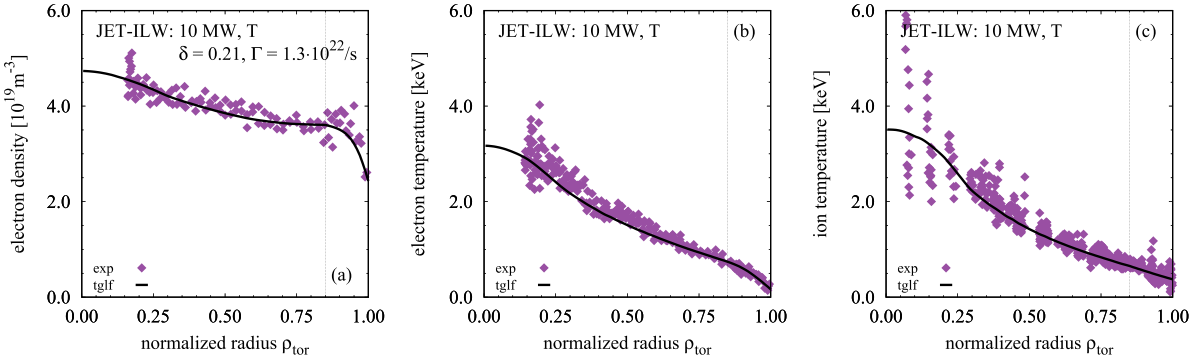

Figure 46. Profiles of electron density (*a*), electron temperature (*b*), ion temperature (*c*) for the T pulse (JPN98794) of the H, T pedestal match with the experimental data as points and the prediction by TGLF-SAT2 as solid line. The position of the boundary condition for the simulation is indicated by the vertical line.

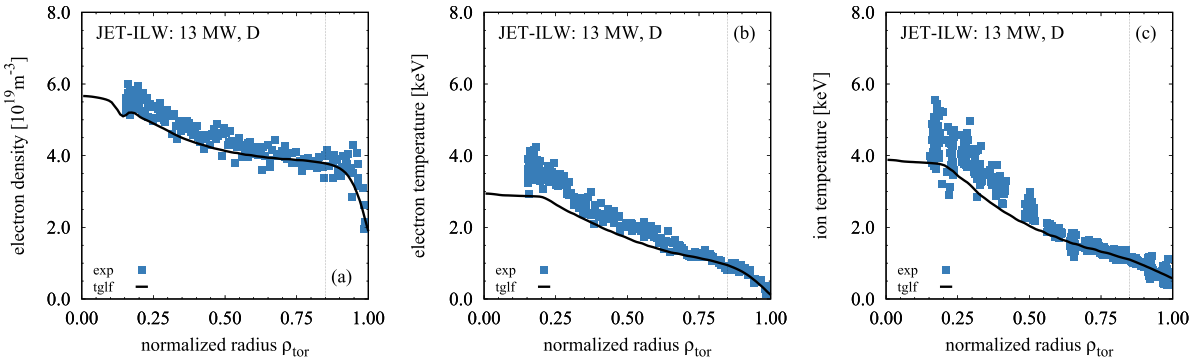

Figure 47. Profiles of electron density (*a*), electron temperature (*b*), ion temperature (*c*) for the D pulse (JPN97512) of the D, T high β_N pedestal density match with the experimental data as points and the prediction by TGLF-SAT2 as solid line. The position of the boundary condition for the simulation is indicated by the vertical line.

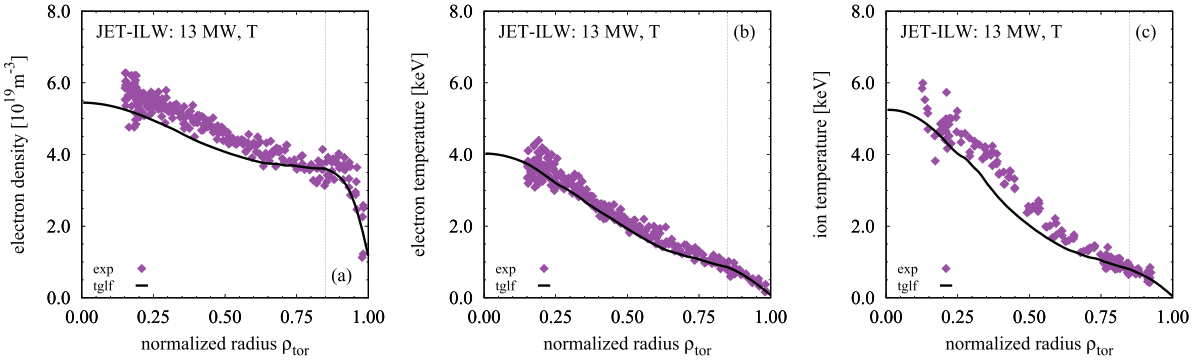

Figure 48. Profiles of electron density (*a*), electron temperature (*b*), ion temperature (*c*) for the high β_N T pulse (JPN99224) with the experimental data as points and the prediction by TGLF-SAT2 as solid line. The position of the boundary condition for the simulation is indicated by the vertical line.

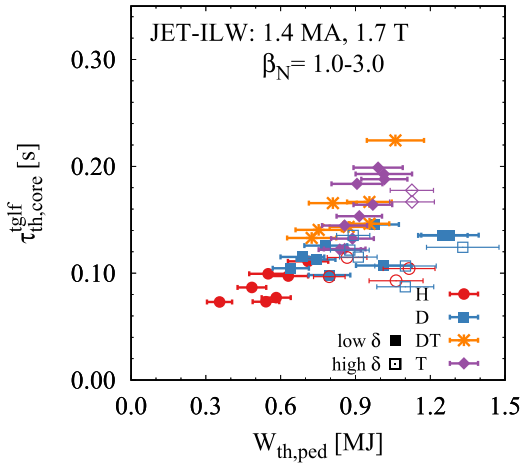

Figure 49. TGLF-SAT2 prediction for the core thermal confinement time as a function of the pedestal thermal stored energy for the entire 1.4 MA, 1.7 T database.

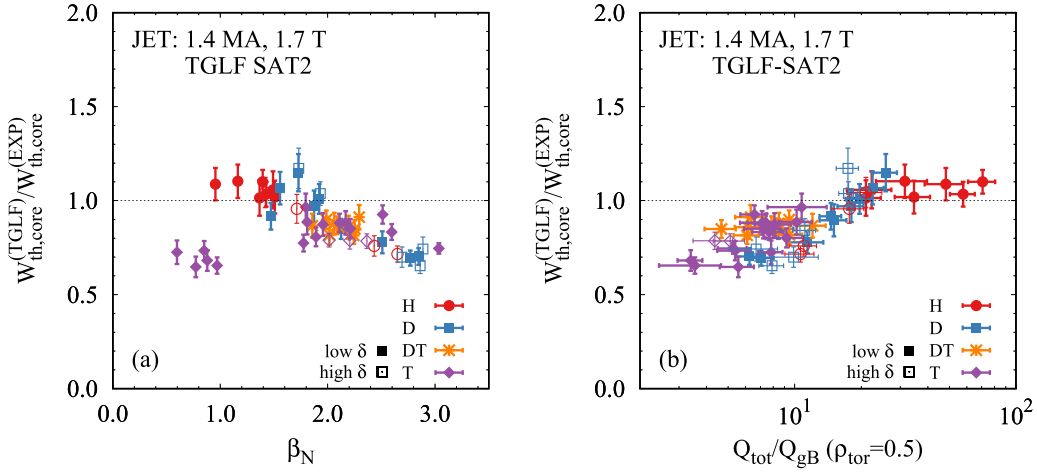

Figure 50. Quality of the TGLF-SAT2 predictions for the core thermal energy as a function of the normalised pressure β_N (*a*) and the heat flux in gyroBohm units at mid radius (*b*).

counterparts at high pedestal pressures. Despite these agreements also systematic deviations are showing, in particular, at higher $W_{th,ped}$ in the form of a discontinuity in the experimentally linear trend of H and D data. Note this is the same overestimation of transport already shown for the individual high β_N profiles.

For further investigation of this discrepancy, we utilise the deviation of predicted and observed core energies $W^{(TGLF)}_{th,core}/W^{(EXP)}_{th,core}$. We find a strong correlation between $W^{(TGLF)}_{th,core}/W^{(EXP)}_{th,core}$ and the normalised total pressure β_N as well as the heat flux in gyroBohm units Q_{tot}/Q_{gB} at $\rho_{tor} = 0.5$ as shown in figure 50. TGLF-SAT2 overestimates the transport at high β_N or low Q_{tot}/Q_{gB} leading to lower plasma energies. Lower Q_{tot}/Q_{gB} essentially means closer to the turbulent threshold. To gain additional insight regarding both correlations we added data with $\beta_N < 1.0$ and very low Q_{tot} just for this comparison. These plasmas are at $P_{heat} \sim 3 \ldots 5$ MW which is closer to the L-H power threshold than the bulk of the higher β_N pulses with $P_{heat} \geqslant 10$ MW. TGLF-SAT2 also overestimates transport for these plasmas, thereby, breaking the β_N correlation, while being consistent with the Q_{tot}/Q_{gB} one.

In section 6 figure 40 we have shown that the experimental density peaking exhibits a strong collisionality dependence. The profile comparisons in figures 45–48 show some deviations between the measured and predicted density profile. Figure 51(*a*) shows this for the whole database. TGLF-SAT2 reproduces the general trends but underestimates the R/L_n close to the boundary. The reason for this is not directly evident, we find some correlation with the density at the boundary, which is an input to the simulations, as shown in figure 51(*b*), but this is fairly weak. Note, while the deviation in the density prediction contributes to the miss match $W_{th,core}$ it is not dominating. The predicted profiles for n, T_e and T_i deviate similarly from their experimental counterparts and have an equal integrated contribution to the mismatch in $W_{th,core}$.

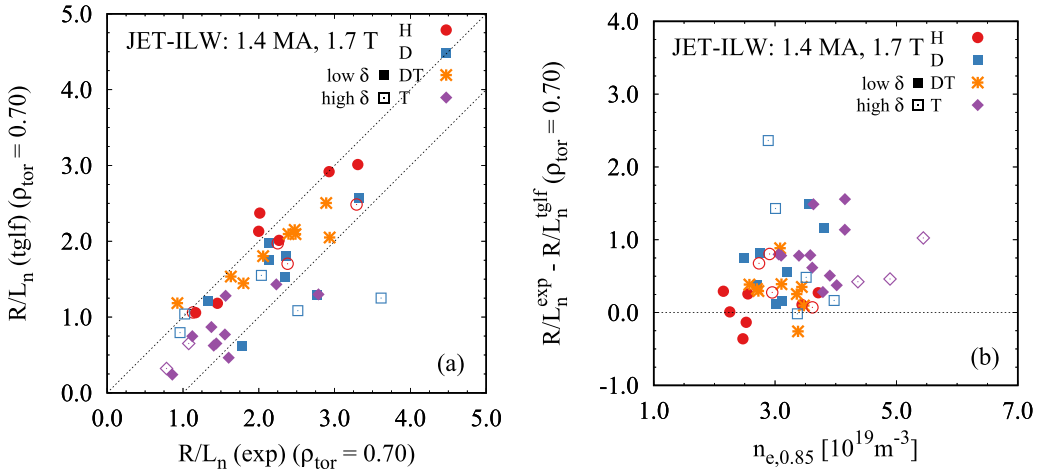

Figure 51. Comparison of the experimental density gradient length and the TGLF-SAT2 prediction at $\rho_{\rm tor} = 0.70$ (a) and the offset between predicted and experimental density gradient lengths as a function of the density at the simulation boundary of $\rho_{\rm tor} = 0.85$.

8. Discussion of core properties

Experimentally we can clearly distinguish the heat transport properties between the medium and high $\beta_{\rm N}$ type-I ELMy H-mode plasmas. At medium $\beta_{\rm N}$ we find $T_{\rm i} = T_{\rm e}$ despite higher ion heating, this is caused by $\chi_{\rm i} > \chi_{\rm e}$. These plasmas are achieved at high $\nu_{\rm eff}$ which results in a relatively low density peaking of 1.2. This is observed similarly in H and T plasmas with matched pedestal parameters and consistent with the H and D comparisons already reported in [18]. At higher $\beta_{\rm N}$ the ion and electron heat diffusivities are more similar $\chi_{\rm i} \sim \chi_{\rm e}$ over most of the radius, consequently, the higher ion heating by NBI results in $T_{\rm i} > T_{\rm e}$ at the same time the density peaking increases to 1.5 due to the lower $\nu_{\rm eff}$. This is mainly observed for high densities and then for D and T alike. At lower densities, which could not be accessed in T, D plasmas are found with $\chi_{\rm i} > \chi_{\rm e}$ even at higher $\beta_{\rm N}$ and similar pedestal pressures than T plasmas at higher density.

We find that DT and T plasmas can have higher core confinement time than their H and D counterparts at similar pedestal energies. Although, this could suggest an isotope mass dependence in the core transport, we can reproduce the difference quantitatively with the TGLF-SAT2 transport model—which does not include such an isotope mass dependence. We observe deviations between TGLF-SAT2 and the experiment, which will be discussed below, however, these deviations are the same for H, D, DT and T thus we cannot infer a mass dependence for them. TGLF-SAT2 is based on a gyroBohm mass dependence and yields $W_{\rm th,core} \propto A^{-0.156}$ when taking the equipartition into account. This mass dependence is already deviating from pure gyroBohm scaling which should yield $W_{\rm th,core} \propto A^{-0.5}$. It is exactly the mass dependence of core confinement as observed in type-I ELMy H-modes in the JET DTE1 campaign [11], where $\tau_{\rm core} \propto A^{-0.16}$ was reported. Still, we expect the mass dependence in the presented database to deviate somewhat, because TGLF-SAT2 predicts a too low R/L_n for high density and high $\nu_{\rm eff}$ plasmas, which is where most of the T data points lie. The impact of fast ions and $\gamma_{E\times B}$ in the TGLF predictions was tested for the H and D plasmas in [18] and it changes with the isotope mass less than 3%. The total impact of fast ions on the simulated stored energy was up to 20% and of $\gamma_{E\times B}$ up to 15%. However, since all plasmas have a finite fast-ion content and rotation the relative impact is well below these numbers. Still, TGLF-SAT2 does not consider the non-linear impact of fast ions and $\gamma_{E\times B}$ on turbulence. In particular, their mass dependence—found in non-linear gyrokinetic simulations [25, 88]—is not treated with the saturation rule SAT2.

One factor contributing to the apparent mass dependence observed in the core confinement is the strong impact of core–edge coupling. A higher pedestal pressure will in general result in an increased core energy due to profile stiffness. Additionally, a higher pedestal density at constant pressure and therefore a lower temperature will reduce the gyroBohm factor in the core and allow for a higher turbulent drive, i.e. temperature gradients, at constant heat fluxes in MW. This argumentation is not necessarily valid for plasmas with features that alter the core transport locally, like internal transport barriers or MHD modes. Note that the experimental edge mass dependence is an input to the core simulations with TGLF-SAT2. So it is no surprise that TGLF-SAT2 can reproduce the indirect mass dependence observed in the core so well.

So the fact that T pulses are generally found at higher pedestal densities than H and D plasmas as discussed in section 5 will directly impact the core performance as well. At high $\beta_{\rm N}$ this is confirmed by comparisons with matched and different densities. The D plasma with lower n and matched $p_{\rm ped}$ but similar $T_{\rm e}$ and $T_{\rm i}$ at mid radius has significantly higher $\chi_{\rm i}$ than its T and D counterpart at higher density.

The systematic deviations observed between TGLF-SAT2 and the experiment, cannot be resolved by introducing an additional mass dependence to the core transport model. A convenient explanation would be the missing EM stabilisation in TGLF-SAT2, which could be responsible for the overestimation of transport at high $\beta_{\rm N}$ which leads to reduced $W_{\rm th,core}$ (figure 50(a)). However, we also find overestimated transport

at very low β_N. While one could argue that these plasmas are quite different from the main database, as they have very low heating power just above the LH power threshold, there is another parameter where the deviation for low and high β_N aligns. This is the heat flux in gyroBohm units Q_{tot}/Q_{gB}. For low Q_{tot}/Q_{gB} the transport is overestimated by TGLF-SAT2 while its prediction is accurate for larger Q_{tot}/Q_{gB} (figure 50(*b*)). This does indicate that closer to the threshold of turbulent transport the model cannot capture the physics as well as well above the threshold. TGLF-SAT2 predicts $\chi_i > \chi_e$ for plasmas with $\chi_i \sim \chi_e$ which suggests a reason for the discrepancy could originate in the ion heat transport channel. Additionally, the largest deviation between experimental and predicted profiles is found for $\rho_{tor} > 0.5$. In this region TGLF-SAT2 also predicts too low R/L_n. Although, we cannot provide an explanation, we find a similar spread in the deviation for all isotope masses which probably means this deviation is not due to the different main ion mass.

We do need to add a disclaimer to the statement regarding the absence of an additional isotope mass dependence on the core transport—additional to what is included in the TGLF-SAT2 transport model. While it is true for the type-I ELMy H-modes and the relatively wide parameter scan we investigated here, it might change when other physics mechanisms become important. One such effect that is well known is the turbulence stabilisation by fast ions and the fast-ion content often varies with isotope mass [16]. In particular, in the presence of a significant α particle population, it is likely not negligible. However, for the data set discussed here, the fast-ion content is relatively low $\leqslant$20% and shows no systematic correlation with the main ion mass in the plasma. While we do expect higher fast-ion content due to T neutral beam injection, the T plasmas are found at higher densities and consequently lower temperatures which mitigates the difference due to the mass in the fast-ion slowing down.

9. Summary

We presented the results of a three isotope scan H, D, T in type-I ELMy H-mode with varying gas fuelling, triangularity and a power variation that resulted in normalised pressures $\beta_N = 1.0 \ldots 3.0$. This data is complemented by D-T mixture plasmas with the same heating and only minor variations in the total gas fuelling. For this data set, we investigated the pedestal characteristics and the core transport. In the analysis, we focus on ways to provide restrictions to theoretical models based on our experimental findings.

In the pedestal, the data shows a strong mass dependence which changes with gas fuelling. Low δ H plasmas lose pedestal pressure with gas fuelling while not gaining in pedestal top density. D plasmas also lose pedestal pressure with gas fuelling while the pedestal top density slightly increases. Higher gas fuelling in T plasmas increases the density at constant pressure. Consequently, we observe different isotope mass scalings for the pedestal density depending on the gas fuelling level. This strongly suggests that a mass scaling is likely only valid for the parameter range it was derived on. Extrapolations or applications to different plasma scenarios need to be discussed with this in mind.

To understand the interplay of the different physics processes in the pedestal we developed an empirical model based on $\gamma_{E\times B}$ turbulence mitigation and realistic neutral penetration with the option to simulate ELM cycles. This dynamic model has the ELM frequency as output and for the first time, a model can explain the mass dependence in the observed f_{ELM}. This makes f_{ELM} a new experimental constraint for the free parameters in the transport model. This is important because a transport analysis based on static or quasi-stationary profiles is typically under-determined when accurate measurements of the particle source are missing. Our model even suggests that for different f_{ELM} a quasi-stationary profile assumption potentially yields misleading results. This is of particular interest for studies with different isotopes where typically $f_{ELM}^{T} < f_{ELM}^{H}$. As observed before, higher ELM frequencies correlate with reduced confinement in our data set, however, this does not depend on the main ion mass. The dynamic ELM cycle modelling suggests that the higher ELM frequencies might not be the cause for the reduced confinement, but the natural consequence of a more unstable pedestal.

Ideal PB modelling is not able to describe the observed mass dependence of the pedestal pressure. But even with a stability model that describes the pedestal pressure correctly, one needs an additional ingredient to explain the observed n/T which changes in the experiment with isotope mass. This ingredient can be a mass dependence in D/χ or in the particle sources. The comparison of our dynamic ELM cycle model with the experimental pedestal characteristics suggests a mass dependence in the particle sources. Note, if the mass acts equally on heat and particle transport, neither the pedestal pressure nor n/T is expected to change, instead the mass dependence would manifest in a different f_{ELM}.

The core plasma scales with the pedestal. A higher pedestal pressure directly improves the core confinement of type-I ELMy H-modes. T plasmas are observed with a unique pedestal composition of high densities and only moderately reduced temperatures. A consequence is that plasmas with T can show improved core confinement even for similar pedestal pressures as H and D plasmas. This core–edge coupling is reproduced in flux-driven TGLF-SAT2 simulations when the measured pedestal is set as the boundary condition. This means that fairly basic physics mechanisms seem to be dominating this coupling. Although within our experimental uncertainties we cannot exclude that there might be an additional mass dependent mechanism in the heat and particle transport the modelling suggests it is not crucial to explain the observations. Note that in this context no additional mass dependence still means a deviation from the pure gyroBohm scaling. These observations suggest that a scaling, which does not separate core and pedestal parameters and includes pedestal parameters in the scaling for the core properties, cannot be expected to yield good results when used for extrapolations.

Consistent with other studies as quoted in section 1 and those for the high performance hybrid and baseline discharges [52, 89], we conclude that with varying main ion masses the differences in basic parameters such as pedestal pressure,

pedestal density or fast-ion content can explain the bulk of changes in the core confinement. When minimising these differences between plasmas with varying isotope mass also the differences in core confinement reduce. Such an explanation does not work for the pedestal. To explain the observations in the pedestal, we require an explicit mass dependence as discussed above.

The implications of this work for larger machines like ITER are the following. The buildup of the pedestal density and the particle transport and sources have a significant impact on the whole plasma and change rather strongly with isotope mass. However, it is not directly clear how this translates to ITER where the SOL is expected to be opaque meaning that the divertor and pedestal plasma become decoupled which is not the case in present day devices [90, 91]. In the core of the plasma, we expect fewer surprises, the transport is observed without strong mass dependence when other influences are minimised. One of the state-of-the-art transport models used for predicting future fusion devices TGLF-SAT2 does a good job to predict the isotope mass dependence of heat and particle transport. The model does this by capturing transport effects which are indirectly connected with a change of mass. In our data set these indirect effects are introduced by the boundary condition. TGLF-SAT2 over predicts the transport in the regime of low gyroBohm heat fluxes which is a regime most relevant for fusion plasmas due to their high temperatures. Lower transport in the real plasma is in general a positive observation, still, it leaves some uncertainties regarding the applicability of this model in such regimes. One important difference in fusion devices will be the high fast-ion population in the form of α particles, whose impact TGLF-SAT2 cannot describe at the moment. However, in our plasmas fast ions played a minor role, therefore, we cannot contribute to this question. JET H-mode plasmas with higher fusion rates and α particle population are reported in [52, 92]. In addition, ITER cannot have type-I ELMs, therefore, investigations of the isotope mass dependence for pedestals with no or small ELMs are required, which were not investigated here.

Studying plasmas with different main ion species raises many questions, but also yields crucial information which is inaccessible in mono isotopic studies. This information should not be interpreted as a free parameter and instead be a source to advance our understanding of fusion plasmas.

Acknowledgments

The authors thank E. Fable and G. Tardini for their support in running the ASTRA transport code. The authors thank G. Conway and C. Silva for fruitful discussions about the interpretation of the Doppler reflectometer data. This work has been carried out within the framework of the EUROfusion Consortium, funded by the European Union via the Euratom Research and Training Programme (Grant Agreement No. 101052200—EUROfusion) and from the EPSRC [Grant Number EP/W006839/1]. Views and opinions expressed are however those of the author(s) only and do not necessarily reflect those of the European Union or the European Commission. Neither the European Union nor the European Commission can be held responsible for them.

Appendix A. Analysis procedure

Profile diagnostics: the main profile diagnostics utilised for this work are the high resolution Thomson scattering (HRTS) [93] and charge exchange spectroscopy (CXRS) [94]. The HRTS yields reliable electron density n_e and temperature T_e profiles up to the separatrix with sufficient time resolution to resolve ELM cycles. The core CXRS diagnostic measures the ion temperature T_i and toroidal rotation frequency ω_{tor} of impurity ions and for selected cases also from the main ions. The main impurity used for CXRS is neon, which is puffed in small quantities during the flattop to enhance the measured CX signal. Due to the ITER like wall ILW with Be and W plasma facing components the intrinsic content of carbon is generally too low to be useful for CXRS measurements. Due to a dedicated edge CXRS system T_i and ω_{tor} are available reliably up to the pedestal top, information about pedestal gradients and separatrix values is only available under optimal conditions which was not the case for the entire database discussed here.

Coordinate mapping: the profile data is mapped from real space to flux coordinates using equilibrium reconstructions with the EFIT code. This procedure can introduce significant uncertainties and even discrepancies, therefore, we tested the mapping of equilibria with different levels of sophistication. The magnetics only reconstruction labelled EFIT typically underestimates the Shafranov shift of the plasma centre due to the missing pressure constraints, which becomes particularly important for high β_N plasmas with high β_p. Also, the reconstructed separatrix shape is found to be inconsistent mainly below the midplane. This becomes evident in the data of diagnostics which measure below the midplane up to the separatrix like the HRTS where the profiles need to be shifted up to several cm to be consistent with the expected separatrix temperatures of $T_{e,sep} = 100\,\text{eV}$. Taking the electron pressure from HRTS measurements into account in an EFIT reconstruction is called EFTP, this improves the consistency of the equilibrium reconstruction significantly and necessary profile shifts remain below 1 cm. The EFTP reconstruction is available for all pulses and is therefore used for the coordinate mapping of measurements throughout the paper. However, the EFTP reconstruction is only based on the electron pressure while $T_i = T_e$ is assumed and the fast-ion pressure is neglected. To test the impact of this assumption we did EFIT++ reconstructions, which utilise an iterative workflow. We map and fit the experimental profiles n_e, T_e, T_i using the magnetics only EFIT, then run TRANSP to determine the fast-ion pressure which then gives the best possible approximation of the total pressure profile. This is then used as input for the equilibrium reconstruction which gives the improved equilibrium EFIT++. This new equilibrium is then used to map the diagnostic data again. The results for a plasma with $T_i > T_e$ and $\sim$20% of fast-ion content is shown in figure 52(*a*) and illustrate that a significant discrepancy can arise in the core when the profiles are compared on normalised poloidal flux

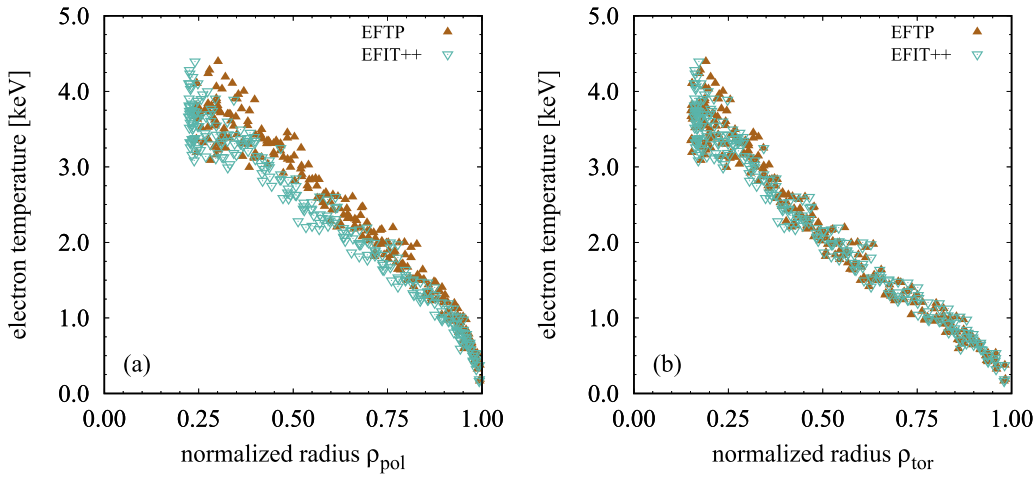

Figure 52. Mapping of the Thomson scattering data onto flux coordinates ρ_{pol} (*a*) and ρ_{tor} (*b*) done with different equilibria for JPN99224.

coordinates with $\rho_{\mathrm{pol}} = \sqrt{(\psi - \psi_{\mathrm{axis}})/(\psi_{\mathrm{sep}} - \psi_{\mathrm{axis}})}$ where ψ is the poloidal flux and ψ_{axis} and ψ_{sep} the respective values at the magnetic axis and the separatrix. In figure 52(*b*) it is shown that this discrepancy is avoided when the normalised toroidal flux label $\rho_{\mathrm{tor}} = \sqrt{(\phi - \phi_{\mathrm{axis}})/(\phi_{\mathrm{sep}} - \phi_{\mathrm{axis}})}$ is used instead, where ϕ is the toroidal flux. Therefore, we will use the normalised toroidal flux label ρ_{tor} for core profiles throughout the paper and only plot comparisons on ρ_{pol} for the pedestal where the potential discrepancy due to the missing fast-ion pressure in the EFTP equilibrium is minimal. Note that the discrepancy between EFTP and EFIT++ is expected to be most severe for high fast-ion pressures, in the shown example $W_{\mathrm{fast}}/W_{\mathrm{th}} \sim 0.2$.

We utilise an additional type of equilibrium reconstruction which relies on MHD markers like the sawtooth inversion radius or the position of a mode with known mode numbers. These MHD markers are then used in an EFTP equilibrium to constrain the q-profile and run with enhanced spatial resolution. An accurate q-profile is particularly important for the gyrokinetic simulations discussed in section 7, therefore, this type of equilibrium was used as input for the gyrokinetic simulations.

ELM synchronisation: if not stated otherwise all shown profiles are ELM synchronised and the pre-ELM data is shown. The ELM synchronisation is done relative to the rise of the Be II line intensity measured in the divertor which is used as ELM indicator. All profiles are sorted in time relative to the next ELM and profiles which are within a 2–3 ms time window up to the ELM crash are selected as pre-ELM. The time window will slightly vary depending on the ELM frequency f_{ELM}, the length of the available stationary phase and the availability of HRTS laser pulses relative to the ELMs. When ELM frequencies are shown those are also determined using the Be II radiation where the frequency is determined via the mean of the time between two adjacent ELMs $f_{\mathrm{ELM}} = 1/\langle \Delta t_{\mathrm{ELM}} \rangle$, uncertainties are then determined as one standard deviation of the Δt_{ELM} distribution. This means a small uncertainty of f_{ELM} corresponds to fairly regular ELMs, while a large uncertainty stems from more irregular ELMs, e.g. smaller ELMs in between more regularly occurring larger ELMs.

Profile fitting: the temperature and density profiles are fitted using a modified hyperbolic tangent function [95] which uses a hyperbolic tangent to fit the pedestal and is connected to a 3rd order polynomial in the core and 1st order polynomial in the scrape-off-layer. On the magnetic axis, $\partial f/\partial \rho_{\mathrm{tor}} = 0$ is used as boundary condition, where f is the fit function. The angular frequency ω is fitted using a spline with free knot locations and $\partial \omega/\partial \rho_{\mathrm{tor}} = 0$ on the magnetic axis, additionally, curvature changes are penalised in the very centre $\rho_{\mathrm{tor}} < 0.2$ where the data quality tends to degrade due to low impurity content. Uncertainties on profile data are determined statistically using the distribution of experimental data over the stationary time intervals selected for analysis. No systematic uncertainties, e.g. due to diagnostic calibration, are taken into account. When determining the pedestal width and gradients we will employ a bilinear fit [70] on only the edge data. For the density, this method yields similar values to an approach with modified hyperbolic tangent fit, for the temperature the values can vary. The reason for this is the relatively gradual change of the temperature inside of the steep gradient region which causes the pedestal width to vary by a factor of 2 depending on the regularisation imposed by the fit function and the radial range of experimental data included in the fit. We fit the data between $\rho_{\mathrm{pol}} = 0.70$ and the foot of the pedestal which is typically at $\rho_{\mathrm{pol}} \simeq 1.01$. The pedestal width Δ is then defined as the distance from the pedestal top to the separatrix.

Doppler reflectometry: the power measured with a reflectometer using a Doppler backscattering technique can be a proxy for the density fluctuation level $\tilde{n}/n$ at the scattering layer in the plasma [96]. We are using the correlation reflectometer [97] for this purpose by utilizing only the main probing frequencies f_{probe}. This is the Doppler V-band with frequencies of 48.8 . . . 74.0 GHz in X-mode. One full sweep takes 286 ms covering 14 distinct frequencies in this range. At the magnetic field of 1.7 T this corresponds to densities

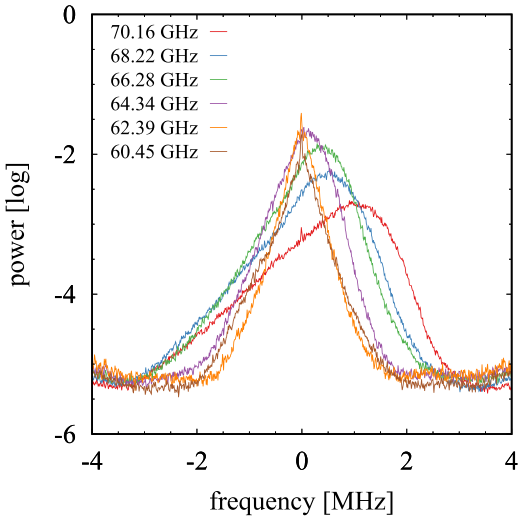

Figure 53. Measured power spectra by Doppler reflectometry for different probing frequencies.

of $\sim 1.2 \ldots 3.0 \cdot 10^{19}\,\mathrm{m}^{-3}$ as determined with ray tracing. This means at low densities we probe the plasma from inside the pedestal top, over the steep gradient region nearly up to the separatrix. Measured power spectra for different probing frequencies are shown in figure 53. While we see a clear Doppler shift when probing the plasma inside of the pedestal top, the Doppler peak vanishes for f_{probe} corresponding to the steep gradient region. Only a relatively symmetric spectrum remains around zero frequency. This can be explained by the very low turbulence levels in the steep gradient region which result in a very low backscattered signal and allows signals from other sources to dominate the spectrum. The source for the peak at zero frequency or zero rotation is most likely due to normal incidence reflection from the plasma. Despite operating the reflectometer with the main microwave beam tilted relatively to the flux surfaces to obtain backscattering there can be components with normal incidents. This is either due to a wide main lobe or due to side lobes and is commonly observed for Doppler reflectometry [98]. Although these components are typically attenuated by 10 dB or more below the main lobe, the turbulence level is higher at the normal incidence with $k_\perp \sim 0 \ldots 1\,\mathrm{cm}^{-1}$ compared to the expected Doppler $k_\perp \sim 10 \ldots 15\,\mathrm{cm}^{-1}$ by at least 10 dB. However, when a significant backscattering signal exists as is the case at higher frequencies the normal incidence signal can again vanish due to frequency locking to the main Doppler shifted signal [98]. To characterise the spectral power we fit the spectra using a Gaussian parametrisation for each time point and then average over the inter ELM phases for each frequency.

Appendix B. Pedestal transport model

The physics ingredients of the pedestal transport model used in section 4.1 are

- A critical gradient model [99] determines the heat diffusivity χ over the full radius up to the separatrix. However, the mass dependency due to the ion Larmor radius is removed from the model as in [2].
- A pedestal transport constraint reduces the heat diffusivity when the local $\gamma_{E\times B}$ exceeds a critical shearing rate. A mass dependence can be introduced in the diffusivity.
- The particle diffusivity is coupled to the ion heat diffusivity over the full radius. The particle convection is assumed to be neoclassical.
- A 1D neutral penetration model [100] calculates the particle source taking the ion mass into account.
- An ELM cycle model is used which triggers a short (1 ms) phase of enhanced transport when the maximum in the normalised pressure gradient $\max(\alpha)$ with $\alpha = -4.02 \cdot 10^{-3} R_0 (\mathrm{d}p/\mathrm{d}\rho_{\mathrm{tor}})(q/B_{\mathrm{t}})^2$ exceeds a predetermined critical value α_{crit}.

The necessary coefficients and critical values are chosen with existing studies in mind but ultimately arbitrarily to reproduce physically reasonable profiles and then scanned successively to document their impact. We distinguish between two general applications of the model, the full model including ELM cycles and a transport limited case where α_{crit} is chosen so high that no ELMs are triggered. Note that results from transport limited modelling often do not hold when ELMs are introduced, however, they help to understand the impact of changes in such a coupled system.

The most important ingredient in the model is the transport mitigation above a critical shearing rate $\gamma_{E\times B}$ which allows us to reproduce H-mode like profiles with steep gradients in the edge. Note this results in a positive feedback loop between $\gamma_{E\times B}$ which acts on the profiles by influencing the transport and the profiles which change $\gamma_{E\times B}$ via the radial electric field $E_{\mathrm{r}} \propto T_i\,(L_n^{-1} + L_{T\mathrm{i}}^{-1})$ where L_n and $L_{T\mathrm{i}}$ are the gradient lengths of ion density and temperature. Small changes in the profiles can be enhanced by this feedback loop. This is also relevant for the formation of the pedestal where the width is determined by neutral penetration. The local particle source results in a local steepening of the density profile which acts as seed for

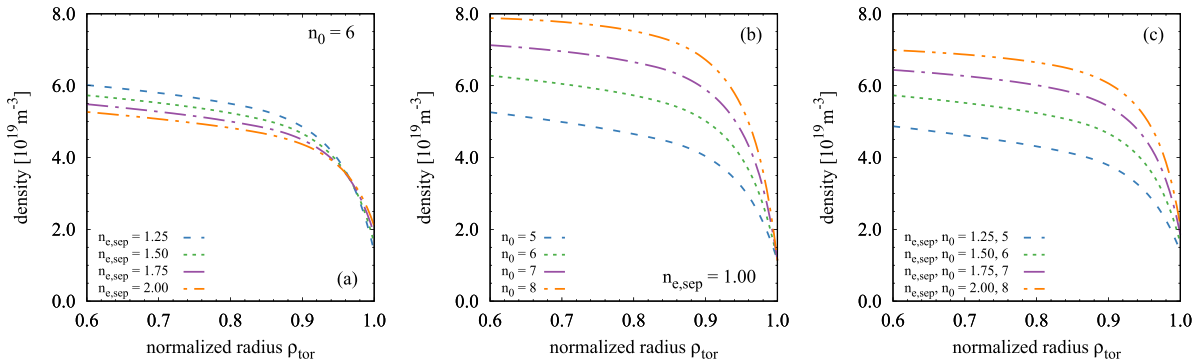

Figure 54. Expected influence of neutral penetration on the density profile in transport equilibrium, when varying separatrix density (*a*), neutral flux (*b*) or both (*c*).

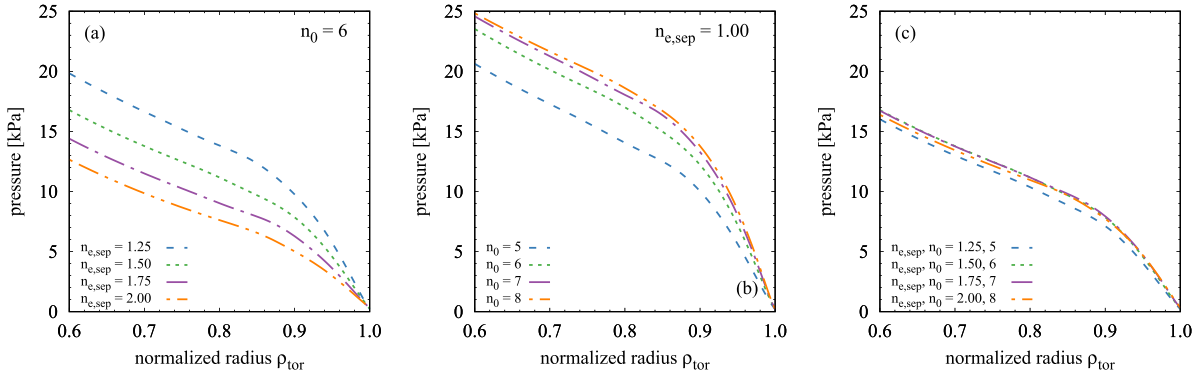

Figure 55. Expected influence of neutral penetration on the pressure profile in transport equilibrium, when varying separatrix density (*a*), neutral flux (*b*) or both (*c*).

the electric field well which is responsible for the shearing rate. The pedestal is then formed due to the feedback loop between $\gamma_{E\times B}$ and the kinetic profiles. $\max(\alpha)$ will reach an equilibrium $\alpha_{\rm eq}$ in the transport limited case because we impose a radial smoothing of the diffusivity to prevent local singularities. In the full ELM cycle case this would not be necessary as the gradients are limited by the imposed $\alpha_{\rm crit}$. Then also the pedestal width might be smaller because the pedestal will not evolve into a steady state solution. $\alpha_{\rm eq}$ will depend on the transport coefficients and the heat and particle sources.

Since we only simulate up to the separatrix we need to set the separatrix values $T_{\rm e,sep}$, $T_{\rm i,sep}$ and $n_{\rm sep}$ as boundary condition. Consequently, the question arises of how to treat gas fuelling in the model. Due to the direct influence of $n_{\rm sep}$ on $\gamma_{E\times B}$ it makes a huge difference whether $n_{\rm sep}$ and the neutral flux Γ are changed individually or together. In the model, the neutral flux is introduced via neutrals $n_0[10^{15}\,{\rm m}^{-3}]$ with a fixed energy of 5 eV at the separatrix. The results of scans in $n_{\rm sep}$ and n_0 are shown in figure 54 for the density and in figure 55 for the pressure. Increasing $n_{\rm sep}$ reduces $\gamma_{E\times B}$ and will result in higher transport and consequently lower density and pressure. Increasing n_0 increases $\nabla n_{\rm e}$ and therefore $\gamma_{E\times B}$, this reduces transport and lead to higher density and pressure. Modifying both at the same time can increase the density at constant pressure. This illustrates an important concept that we will call fuelling efficiency $n_0/n_{\rm sep}$. It describes the efficiency of depositing particles within the plasma while keeping $n_{\rm sep}$ constant. The fuelling efficiency is different from general fuelling where $n_{\rm sep}$ and n_0 change simultaneously. Improving the fuelling efficiency will be beneficial for confinement while normal fuelling can have a detrimental impact.

Due to the use of a neutral penetration model we introduce a mass dependence in the particle source. Lower ion masses will have deeper neutral penetration. To mimic a potential mass dependence in the heat and particle transport as well we add an explicit mass dependence in the transport equation in the form of $\chi \propto A^{\mu}$. The exponent μ is a variable input where $\mu = 0.5$ would correspond to a gyroBohm mass dependence, $\mu = -0.5$ to an anti-gyroBohm mass dependence and $\mu = 0$ would correspond to no mass dependence.

The transport limited simulations discussed above are of educational value as they illustrate basic nonlinear interactions between the particle and heat transport channels. However, those steady state solutions are likely not stable against peeling-ballooning modes and when ELMs are the limiting factor the results can change significantly.

First, we need to understand the interaction between $\alpha_{\rm crit}$ and $\alpha_{\rm eq}$. For most transport analysis in the H-mode pedestal one assumes a quasi-stationary situation, i.e. a transport equilibrium is reached before an ELM is triggered, because only then a power/particle balance analysis is viable. In our terminology this corresponds to $\alpha_{\rm crit} = \alpha_{\rm eq}$. In figure 56 the temporal evolution of the temperature after an ELM crash is plotted for different heating powers. In both cases, an ELM

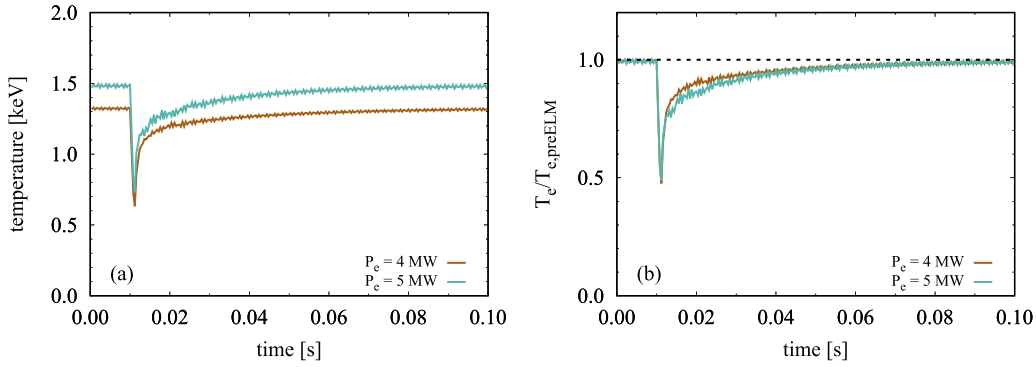

Figure 56. Evolution of temperature (*a*) and normalised temperature (*b*) after an ELM crash with $\alpha_{\text{crit}} = \alpha_{\text{eq}}$ at $\rho_{\text{tor}} = 0.92$ for different heating power.

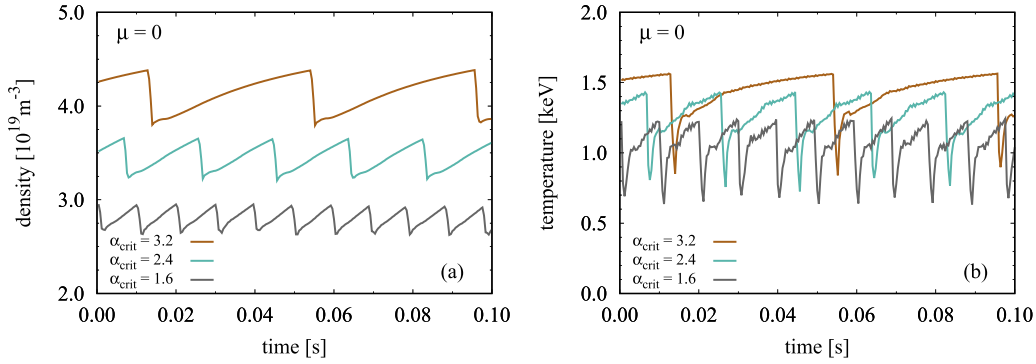

Figure 57. Evolution of density (*a*) and temperature (*b*) during an ELM cycle at $\rho_{\text{tor}} = 0.92$ for different α_{crit} and an $\alpha_{\text{eq}} = 3.8$.

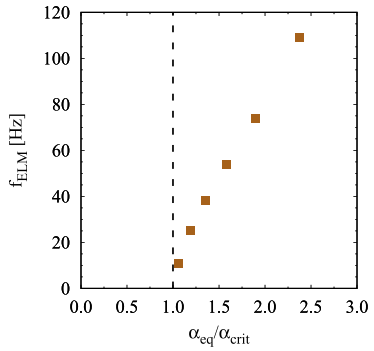

Figure 58. ELM frequency as a function of $\alpha_{\text{eq}}/\alpha_{\text{crit}}$.

is triggered for a quasi-stationary pedestal. In (*a*) the different α_{eq} due to the change in P_{heat} is visible. When T is normalised to its pre-ELM value shown in (*b*) no variation in the ELM recovery time is observed. This suggests ELMs triggered in quasi-stationary conditions will have a frequency independent of the heating power. For type-I ELMs f_{ELM} increases with power [17, 101]. So a quasi-stationary pedestal does not show the power dependence of f_{ELM} expected for type-I ELMs.

For the remainder of this section, we do not consider this quasi-stationary case anymore, but instead a dynamic system. This is done by imposing an α_{crit} with $\alpha_{\text{crit}} < \alpha_{\text{eq}}$ which will result in dynamic ELM cycles. To illustrate the basic features of these ELMy simulations we start with $\mu = 0$ and sources that yield $\alpha_{\text{eq}} = 3.8$ and vary α_{crit} below this upper bound. The result of this α_{crit} scan is shown in figure 57, for lower α_{crit} the pedestal density and temperature are naturally lower before the crash, where the density varies slightly more than the temperature, but n/T stays the same within 10%. Additionally, the ELMs become smaller and more frequent. The reason for the higher f_{ELM} stems from the non-linearity of the $\gamma_{E\times B}$ transport model which is best visible in the temperature recovery time traces. After the crash, the pedestal is near instantaneously refilled with energy from the core which helps to start the feedback loop which slows down as $\max(\alpha)$ approaches the transport equilibrium α_{eq}. The reason for the difference in ELM size is not directly obvious, as the coefficients for the enhanced transport during the 1 ms ELM crash are the same in all cases. This shows how the ELM frequency can change

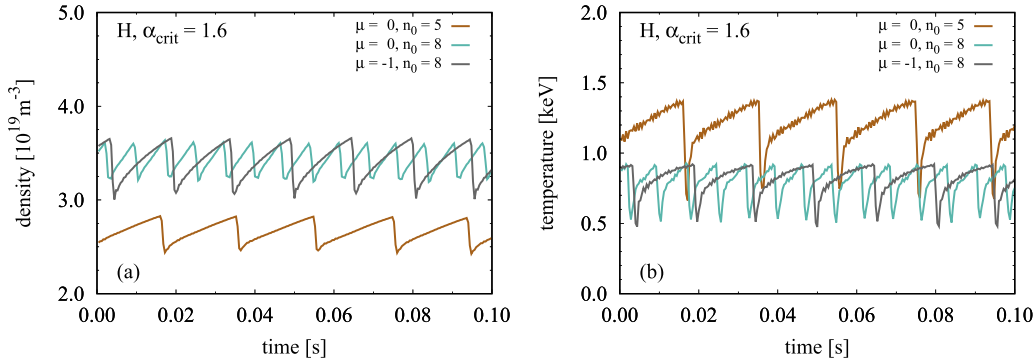

Figure 59. Evolution of density (*a*) and temperature (*b*) during an ELM cycle at $\rho_{\mathrm{tor}} = 0.92$ for the same mass but different mass dependence in the edge transport model and different fuelling efficiency.

despite constant heat and particle sources. In this picture, the change of the ELM frequency with different heat and particle sources is a result of α_{eq} and α_{crit} changing at different rates. In figure 58 the change of f_{ELM} with $\alpha_{\mathrm{eq}}/\alpha_{\mathrm{crit}}$ is shown for an α_{crit} scan where $\alpha_{\mathrm{eq}} = 3.8$. Similarly, for a dynamic pedestal with $\alpha_{\mathrm{eq}} > \alpha_{\mathrm{crit}}$ and a constant α_{crit}, f_{ELM} will increase with higher power, because α_{eq} increases with heating power. So the power dependence of type-I ELMs will be found as long as $\partial\alpha_{\mathrm{eq}}/\partial P > \partial\alpha_{\mathrm{crit}}/\partial P$. This is a strong indication that type-I ELMy plasmas are stability limited with $\alpha_{\mathrm{eq}} > \alpha_{\mathrm{crit}}$ rather than quasi-stationary with $\alpha_{\mathrm{eq}} = \alpha_{\mathrm{crit}}$.

Since the transport model discussed here is based on coupled heat and particle transport changing α_{crit} will not vary the ratio n/T significantly. A way to vary n/T at constant α_{crit} is via the particle sources or the fuelling efficiency n_0/n_{sep}. A n_0 variation with constant n_{sep} is illustrated in figure 59. While changing the diffusivities via the mass exponent μ again only results in different f_{ELM}, a reduction of the neutral source n_0 will significantly impact n/T at constant pressure. A similar effect can be achieved in a model that decouples heat and particle transport based on the main ion mass. We have not tested it here, but with $D \propto A^{\nu}$ and $\chi \propto A^{\mu}$ with $\nu \neq \mu$ the mass dependence of n_0 can be incorporated into ν. Still, source and transport driven changes should result in different pedestal width characteristics as discussed in section 5.

Appendix C. Pulse list

The pulses used in this publication are listed in table 1.

Table 1. Pulse numbers and time intervals used in this publication.

JPN	time (s)	I_p (MA)	B_t (T)	A	P_{NBI} (MW)	P_{ICRH} (MW)	Γ (10^{22} s^{-1})	δ	β_N
	H								
91358	5.0–8.5	1.4	1.7	1.0	10.4	0.0	0.9	0.22	1.4
91426	5.5–8.5	1.4	1.7	1.0	9.2	3.2	0.9	0.23	1.5
91552	5.5–8.5	1.4	1.7	1.0	9.3	5.5	3.6	0.22	1.4
91553	5.5–8.5	1.4	1.7	1.0	10.1	6.4	5.3	0.22	1.4
91557	5.5–8.5	1.4	1.7	1.0	10.1	0.0	1.7	0.21	1.0
97094	6.0–9.0	1.4	1.7	1.0	10.0	0.0	1.8	0.29	1.4
97094	11.0–13.5	1.4	1.7	1.0	10.0	0.0	1.8	0.22	1.2
97095	6.0–8.5	1.4	1.7	1.0	10.0	0.0	0.9	0.30	1.7
97095	11.0–13.5	1.4	1.7	1.0	9.8	0.0	0.9	0.22	1.5
97096	5.5–6.1	1.4	1.7	1.0	15.6	0.0	0.8	0.32	2.6
97096	8.5–11.5	1.4	1.7	1.0	16.3	0.0	0.8	0.32	2.4
	D								
87335	6.2–7.2	1.4	1.7	2.0	9.8	0.0	0.8	0.23	1.9
87338	5.0–8.5	1.4	1.7	2.0	6.3	0.0	0.9	0.22	1.5
87344	5.5–8.5	1.4	1.7	2.0	9.9	0.0	1.9	0.22	1.6
96830	4.8–6.2	1.4	1.7	2.0	13.3	0.0	0.9	0.27	2.5
96831	4.8–5.2	1.4	1.7	2.0	15.2	0.0	1.0	0.28	2.9
97035	12.0–14.0	1.4	1.7	2.0	10.1	0.0	1.3	0.21	1.7
97035	16.5–18.5	1.4	1.7	2.0	10.0	0.0	1.3	0.29	1.9
97036	12.0–13.5	1.4	1.7	2.0	10.0	0.0	0.8	0.22	1.9
97036	16.0–17.0	1.4	1.7	2.0	10.0	0.0	0.8	0.29	1.7
97510	5.5–6.7	1.4	1.7	2.0	13.6	0.0	1.0	0.31	2.7
97510	10.0–11.5	1.4	1.7	2.0	13.5	0.0	0.5	0.32	2.9
97512	5.0–5.4	1.4	1.7	2.0	13.4	0.0	1.8	0.27	2.8
97512	5.5–6.6	1.4	1.7	2.0	13.4	0.0	1.8	0.26	2.8
99484	5.0–6.7	1.4	1.7	2.0	10.4	0.0	1.0	0.25	2.1
	DT								
99485	11.5–13.5	1.4	1.7	2.3	10.0	0.0	1.1	0.21	1.9
99485	15.5–17.5	1.4	1.7	2.4	9.8	0.0	1.1	0.29	2.0
99486	10.5–11.5	1.4	1.7	2.4	10.0	0.0	0.9	0.22	2.2
99486	11.5–13.5	1.4	1.7	2.4	9.9	0.0	0.9	0.21	2.0
99486	15.5–17.5	1.4	1.7	2.5	9.9	0.0	0.9	0.29	2.1
99487	10.5–11.5	1.4	1.7	2.6	9.9	0.0	0.7	0.22	2.3
99487	11.5–13.5	1.4	1.7	2.6	9.9	0.0	0.7	0.22	2.1
99487	15.5–16.5	1.4	1.7	2.6	9.7	0.0	0.8	0.30	2.2
99808	10.8–11.5	1.5	1.7	2.5	10.1	0.0	0.7	0.23	2.3
	T								
98792	11.5–12.1	1.4	1.7	3.0	10.0	0.0	2.0	0.21	1.8
98794	11.5–12.2	1.4	1.7	3.0	9.8	0.0	1.4	0.21	1.8
98794	12.5–13.7	1.4	1.7	3.0	10.0	0.0	1.4	0.21	1.9
98794	14.9–16.0	1.4	1.7	3.0	9.9	0.0	1.4	0.30	2.2
98795	11.5–12.4	1.4	1.7	3.0	10.0	0.0	0.9	0.22	2.2
98795	12.7–13.5	1.4	1.7	3.0	10.0	0.0	0.9	0.21	2.0
98795	15.2–15.8	1.4	1.7	3.0	10.0	0.0	0.9	0.31	2.4
99224	4.5–5.0	1.4	1.7	3.0	9.6	0.0	1.4	0.24	2.2
99224	5.2–5.5	1.4	1.7	3.0	12.1	0.0	1.2	0.26	2.6
99224	5.5–5.9	1.4	1.7	3.0	12.1	0.0	1.2	0.27	3.0
99224	6.3–6.8	1.4	1.7	3.0	12.1	0.0	1.2	0.25	2.5
99973	4.7–7.3	1.4	1.7	3.0	10.6	0.0	1.1	0.25	2.1
100110	11.7–12.0	1.4	1.7	3.0	1.0	0.0	1.0	0.18	0.6
100110	12.5–14.0	1.4	1.7	3.0	2.0	0.0	1.0	0.19	0.8
100110	14.2–14.9	1.4	1.7	3.0	3.0	0.0	1.0	0.19	0.9
100177	11.7–13.5	1.4	1.7	3.0	9.9	0.0	1.7	0.21	1.8
100177	14.3–15.2	1.4	1.7	3.0	10.0	0.0	1.8	0.30	2.0
100186	10.5–11.5	1.4	1.7	3.0	3.0	0.0	0.9	0.19	0.9
100186	12.1–12.7	1.4	1.7	3.0	3.1	0.0	0.9	0.19	1.0

ORCID iDs

P.A. Schneider https://orcid.org/0000-0001-7257-3412
C. Angioni https://orcid.org/0000-0003-0270-9630
F. Auriemma https://orcid.org/0000-0002-1043-1563
N. Bonanomi https://orcid.org/0000-0003-4344-3330
T. Görler https://orcid.org/0000-0002-0851-6699
R. Henriques https://orcid.org/0000-0003-0585-0904
L. Horvath https://orcid.org/0000-0002-5692-6772
R. Lorenzini https://orcid.org/0000-0001-8353-4857
H. Nyström https://orcid.org/0000-0002-1310-4517
M. Maslov https://orcid.org/0000-0001-8392-4644
J. Ruiz https://orcid.org/0000-0003-4258-5273
A. Chomiczewska https://orcid.org/0000-0003-4931-728X
E. Delabie https://orcid.org/0000-0001-9834-874X
J.M. Fontdecaba https://orcid.org/0000-0001-7678-0240
L. Frassinetti https://orcid.org/0000-0002-9546-4494
J. Garcia https://orcid.org/0000-0003-0900-5564
J. Hobirk https://orcid.org/0000-0001-6605-0068
A. Kappatou https://orcid.org/0000-0003-3341-1909
D.L. Keeling https://orcid.org/0000-0002-3581-7788
B. Lomanowski https://orcid.org/0000-0003-2226-2004
T. Luda di Cortemiglia https://orcid.org/0000-0002-9941-0039
C.F. Maggi https://orcid.org/0000-0001-7208-2613
G. Pucella https://orcid.org/0000-0002-9923-2770
A. Thorman https://orcid.org/0000-0001-5912-9325

References

[1] Bessenrodt-Weberpals M. *et al* 1993 *Nucl. Fusion* **33** 1205
[2] Schneider P.A. *et al* 2017 *Nucl. Fusion* **57** 066003
[3] Delabie E. *et al* 2017 Preliminary interpretation of the isotope effect on energy confinement in Ohmic discharges in JET-ILW *44th EPS Conf. on Plasma Physics* (*Belfast, 26–30 June 2017*) (European Physical Society) p P4.159 (available at: http://ocs.ciemat.es/EPS2017PAP/pdf/P4.159.pdf)
[4] Kuprienko D.V., Altukhov A.B., Gurchenko A.D., Gusakov E.Z., Esipov L.A., Kaledina O.A., Tropin N.V., Lashkul S.I., Troshin G.A. and Shatalin S.V. 2019 *Plasma Phys. Rep.* **45** 1128
[5] Maggi C.F. *et al* 2019 *Nucl. Fusion* **59** 076028
[6] Xu Y., Hidalgo C., Shesterikov I., Krämer-Flecken A., Zoletnik S., Van Schoor M. and Vergote M. (The TEXTOR Team) 2013 *Phys. Rev. Lett.* **110** 265005
[7] Schneider P.A., Hennequin P., Bonanomi N., Dunne M., Conway G.D. and Plank U. 2021 *Plasma Phys. Control. Fusion* **63** 64006
[8] Conway G.D. *et al* 2022 *Nucl. Fusion* **62** 13001
[9] Challis C.D. *et al* 2015 *Nucl. Fusion* **55** 053031
[10] Saibene G. *et al* 1999 *Nucl. Fusion* **39** 1133
[11] Cordey J.G. *et al* 1999 *Nucl. Fusion* **39** 301
[12] Urano H., Takizuka T., Aiba N., Kikuchi M., Nakano T., Fujita T., Oyama N., Kamada Y. and Hayashi N. 2013 *Nucl. Fusion* **53** 083003
[13] Laggner F.M. *et al* 2017 *Phys. Plasmas* **24** 56105
[14] Maggi C.F. *et al* 2018 *Plasma Phys. Control. Fusion* **60** 14045
[15] Weisen H. *et al* 2020 *J. Plasma Phys.* **86** 905860501
[16] Schneider P.A. *et al* 2021 *Nucl. Fusion* **61** 036033
[17] Horvath L. *et al* 2021 *Nucl. Fusion* **61** 046015
[18] Schneider P.A. *et al* 2022 *Nucl. Fusion* **62** 26014
[19] Garbet X. *et al* 2004 *Plasma Phys. Control. Fusion* **46** 1351
[20] Camenen Y., Pochelon A., Behn R., Bottino A., Bortolon A., Coda S., Karpushov A., Sauter O., Zhuang G. and team T.T. 2007 *Nucl. Fusion* **47** 510
[21] Scott S.D. *et al* 1995 *Phys. Plasmas* **2** 2299
[22] Bonanomi N. *et al* 2019 *Nucl. Fusion* **59** 096030
[23] Waltz R.E., DeBoo J.C. and Rosenbluth M.N. 1990 *Phys. Rev. Lett.* **65** 2390
[24] Garcia J. *et al* 2022 *Plasma Phys. Control. Fusion* **64** 54001
[25] Garcia J., Görler T., Jenko F. and Giruzzi G. 2017 *Nucl. Fusion* **57** 014007
[26] Bustos A., Bañón Navarro A., Görler T., Jenko F. and Hidalgo C. 2015 *Phys. Plasmas* **22** 012305
[27] Angioni C., Peeters A.G., Pereverzev G.V., Ryter F. and Tardini G. 2003 *Phys. Rev. Lett.* **90** 205003
[28] Weisen H. *et al* 2005 *Nucl. Fusion* **45** L1
[29] Greenwald M., Angioni C., Hughes J.W., Terry J. and Weisen H. 2007 *Nucl. Fusion* **47** L26
[30] Fable E. *et al* 2019 *Nucl. Fusion* **59** 76042
[31] Tala T. *et al* 2019 *Nucl. Fusion* **59** 126030
[32] Mordijck S. *et al* 2020 *Nucl. Fusion* **60** 66019
[33] Angioni C., Candy J., Fable E., Maslov M., Peeters A.G., Waltz R.E. and Weisen H. 2009 *Phys. Plasmas* **16** 060702
[34] Angioni C., Fable E., Manas P., Mantica P. and Schneider P.A. 2018 *Phys. Plasmas* **25** 82517
[35] Bonanomi N., Angioni C., Crandall P.C., Di Siena A., Maggi C.F. and Schneider P.A. 2019 *Nucl. Fusion* **59** 126025
[36] Belli E.A., Candy J. and Waltz R.E. 2019 *Phys. Plasmas* **26** 82305
[37] Predebon I., Hatch D.R., Frassinetti L., Horvath L., Saarelma S., Chapman-Oplopoiou B., Görler T. and Maggi C.F. 2023 *Nucl. Fusion* **63** 36010
[38] Luce T.C., Petty C.C. and Cordey J.G. 2008 *Plasma Phys. Control. Fusion* **50** 43001
[39] Tala T. *et al* 2023 *Nucl. Fusion* **63** 112012
[40] Staebler G.M., Belli E.A., Candy J., Kinsey J.E., Dudding H. and Patel B. 2021 *Nucl. Fusion* **61** 116007
[41] Candy J., Belli E.A. and Bravenec R.V. 2016 *J. Comput. Phys.* **324** 73
[42] Dudding H.G., Casson F.J., Dickinson D., Patel B.S., Roach C.M., Belli E.A. and Staebler G.M. 2022 *Nucl. Fusion* **62** 96005
[43] Luda T. *et al* 2023 *Plasma Phys. Control. Fusion* **65** 34001
[44] Joffrin E. *et al* 2005 *Nucl. Fusion* **45** 626
[45] Maggi C.F. *et al* (The ASDEX Upgrade Team, The DIII-D Team, The JT-60U Team and EFDA-JET Contributors for the Pedestal and Edge Physics and the Steady State Operation Topical Groups of the ITPA) 2007 *Nucl. Fusion* **47** 535
[46] Garcia J., Challis C., Citrin J., Doerk H., Giruzzi G., Görler T., Jenko F. and Maget P. 2015 *Nucl. Fusion* **55** 053007
[47] Maggi C.F. *et al* 2015 *Nucl. Fusion* **55** 113031
[48] King D. *et al* 2023 *Nucl. Fusion* **63** 112005
[49] Pankin A., McCune D., Andre R., Bateman G. and Kritz A. 2004 *Comput. Phys. Commun.* **159** 157
[50] Breslau J. *et al* 2018 *TRANSP (Computer Software)* (https://doi.org/10.11578/dc.20180627.4)
[51] Carvalho I.S. *et al* 2017 *Fusion Eng. Des.* **124** 841
[52] Hobirk J. *et al* 2023 *Nucl. Fusion* **63** 112001
[53] Angioni C. 2021 *Plasma Phys. Control. Fusion* **63** 73001
[54] Lomanowski B. *et al* 2022 *Nucl. Fusion* **62** 66030

[55] Schneider P.A., Wolfrum E., Groebner R.J., Osborne T.H., Beurskens M.N.A., Dunne M.G., Kurzan B., Pütterich T. and Viezzer E. 2013 *Nucl. Fusion* **53** 073039
[56] Pütterich T., Neu R., Dux R., Whiteford A.D., O'Mullane M.G. and Summers H.P. 2010 *Nucl. Fusion* **50** 25012
[57] Pinzón J.R., Happel T., Blanco E., Conway G.D., Estrada T. and Stroth U. 2017 *Plasma Phys. Control. Fusion* **59** 35005
[58] Wilson H.R., Snyder P.B., Huysmans G.T.A. and Miller R.L. 2002 *Phys. Plasmas* **9** 1277
[59] Viezzer E. *et al* 2018 *Nucl. Fusion* **58** 026031
[60] Frassinetti L. *et al* 2023 *Nucl. Fusion* **63** 112009
[61] Frassinetti L. *et al* 2021 *Nucl. Fusion* **61** 126054
[62] Kojima A., Oyama N., Sakamoto Y., Kamada Y., Urano H., Kamiya K., Fujita T., Kubo H. and Aiba N. 2009 *Nucl. Fusion* **49** 115008
[63] Burckhart A., Wolfrum E., Fischer R., Lackner K. and Zohm H. 2010 *Plasma Phys. Control. Fusion* **52** 105010
[64] Groebner R.J. *et al* 2010 *Nucl. Fusion* **50** 064002
[65] Nyström H., Frassinetti L., Saarelma S., Huijsmans G.T.A., Perez von Thun C., Maggi C.F. and Hillesheim J.C. (JET Contributors) 2022 *Nucl. Fusion* **62** 126045
[66] Mahdavi M.A., Maingi R., Groebner R.J., Leonard A.W., Osborne T.H. and Porter G. 2003 *Phys. Plasmas* **10** 3984
[67] Hubbard A.E. 2000 *Plasma Phys. Control. Fusion* **42** A15
[68] Urano H., Takizuka T., Kamada Y., Oyama N. and Takenaga H. 2008 *Nucl. Fusion* **48** 045008
[69] Groebner R.J., Leonard A.W., Snyder P.B., Osborne T.H., Maggi C.F., Fenstermacher M.E., Petty C.C. and Owen L.W. 2009 *Nucl. Fusion* **49** 085037
[70] Schneider P.A. *et al* 2012 *Plasma Phys. Control. Fusion* **54** 105009
[71] Leyland M.J. *et al* 2013 *Nucl. Fusion* **53** 083028
[72] Eckstein W. 2002 Calculated Sputtering, Reflection and Range Values IPP-Report 9/132 (Max-Planck-Institut für Plasmaphysik) (available at: https://hdl.handle.net/11858/00-001M-0000-0027-4522-5)
[73] Makarov S.O., Coster D.P., Kaveeva E.G., Rozhansky V.A., Senichenkov I.Y., Veselova I.Y., Voskoboynikov S.P., Stepanenko A.A., Bonnin X. and Pitts R.A. 2023 *Nucl. Fusion* **63** 26014
[74] Bonanomi N., Angioni C., Plank U., Schneider P.A. and Maggi C.F. 2021 *Phys. Plasmas* **28** 52504
[75] Birkenmeier G. *et al* 2022 *Nucl. Fusion* **62** 86005
[76] Plank U. *et al* 2023 *Plasma Phys. Control. Fusion* **65** 14001
[77] Solano E. *et al* 2023 *Nucl. Fusion* **63** 112011
[78] Görler T., Lapillonne X., Brunner S., Dannert T., Jenko F., Merz F. and Told D. 2011 *J. Comput. Phys.* **230** 7053
[79] Dunne M.G. *et al* 2017 *Plasma Phys. Control. Fusion* **59** 25010
[80] Luda T., Angioni C., Dunne M.G., Fable E., Kallenbach A., Bonanomi N., Schneider P.A., Siccinio M. and Tardini G. 2020 *Nucl. Fusion* **60** 036023
[81] Suttrop W. *et al* 1997 *Plasma Phys. Control. Fusion* **39** 2051
[82] Petty C.C., Luce T.C., Pinsker R.I., Burrell K.H., Chiu S.C., Gohil P., James R.A. and Wròblewski D. 1995 *Phys. Rev. Lett.* **74** 1763
[83] Fable E. *et al* 2013 *Plasma Phys. Control. Fusion* **55** 124028
[84] Tardini G., Weiland M., Angioni C., Cavedon M., Ryter F. and Schneider P.A. (The ASDEX Upgrade Team) 2021 *Nucl. Fusion* **61** 036030
[85] Challis C.D., Cordey J.G., Hamnén H., Stubberfield P.M., Christiansen J.P., Lazzaro E., Muir D.G., Stork D. and Thompson E. 1989 *Nucl. Fusion* **29** 563
[86] Eriksson L.-G., Hellsten T. and Willen U. 1993 *Nucl. Fusion* **33** 1037
[87] Tardini G., Hobirk J., Igochine V.G., Maggi C.F., Martin P., McCune D., Peeters A.G., Sips A.C.C., Stäbler A. and Stober J. (The ASDEX Upgrade Team) 2007 *Nucl. Fusion* **47** 280
[88] Garcia J., Görler T. and Jenko F. 2018 *Phys. Plasmas* **25** 55902
[89] Kim H.-T. *et al* 2023 *Nucl. Fusion* **63** 112004
[90] Romanelli M. *et al* 2015 *Nucl. Fusion* **55** 93008
[91] Mordijck S. 2020 *Nucl. Fusion* **60** 82006
[92] Maslov M. *et al* 2023 *Nucl. Fusion* **63** 112002
[93] Frassinetti L., Beurskens M.N.A., Scannell R., Osborne T.H., Flanagan J., Kempenaars M., Maslov M., Pasqualotto R. and Walsh M. 2012 *Rev. Sci. Instrum.* **83** 13506
[94] Hawkes N.C., Delabie E., Menmuir S., Giroud C., Meigs A.G., Conway N.J., Biewer T.M. and Hillis D.L. 2018 *Rev. Sci. Instrum.* **89** 10D113
[95] Groebner R.J. and Osborne T.H. 1998 *Phys. Plasmas* **5** 1800
[96] Lechte C., Conway G.D., Görler T. and Tröster-Schmid C. (The ASDEX Upgrade Team) 2017 *Plasma Phys. Control. Fusion* **59** 075006
[97] Meneses L., Cupido L. and Manso M.E. 2011 *Fusion Eng. Des.* **86** 552
[98] Conway G.D., Tröster C., Schirmer J., Angioni C., Holzhauer E., Jenko F., Merz F., Poli E., Scott B. and Suttrop W. (The ASDEX Upgrade Team) 2007 Doppler reflectometry on ASDEX Upgrade: foundations and latest results *8th Int. Reflectometry Workshop—IRW8 (St. Petersburg, 2–4 May 2007)* vol 8 pp 2–4 (available at: www.aug.ipp.mpg.de/IRW/IRW8/papers/0805-IRW08-ConwayG-paper.pdf)
[99] Ryter F., Camenen Y., DeBoo J.C., Imbeaux F., Mantica P., Regnoli G., Sozzi C. and Stroth U. (ASDEX Upgrade, DIII-D, FTU, JET-EFDA contributors, TCV, Tore Supra and W7-AS Teams) 2006 *Plasma Phys. Control. Fusion* **48** B453
[100] Pereverzev G.V. and Yushmanov P.N. 2002 ASTRA automated system for transport analysis in a tokamak *IPP Report* 5/98 (Max-Planck-Institut für Plasmaphysik) (available at: https://hdl.handle.net/11858/00-001M-0000-0027-4512-9)
[101] Kallenbach A. *et al* 2009 *Nucl. Fusion* **49** 045007